Drift-Field Distortions and Specific Energy Loss Calibration of the ALICE TPC in LHC Run 3

Dissertation
zur Erlangung des Doktorgrades
der Naturwissenschaften

vorgelegt beim Fachbereich Physik
der Johann Wolfgang Goethe-Universität
in Frankfurt am Main
von

Matthias Kleiner
aus Frankfurt am Main, Deutschland

Frankfurt am Main 2024
(D 30)

Vom Fachbereich Physik
der Johann Wolfgang Goethe-Universität
als Dissertation angenommen.

Dekan:	Prof. Dr. Roger Erb
Gutachter:	Prof. Dr. Henner Büsching
	Prof. Dr. Harald Appelshäuser

Datum der Disputation: 17.12.2024

Zusammenfassung

Die Fragen nach dem Ursprung, der Entstehung und dem Aufbau unseres Universums beschäftigen die Wissenschaft seit Jahrtausenden. Am Ende des 19. Jahrhunderts lieferten aus heutiger Sicht einfache Experimente grundlegende Erkenntnisse über den Aufbau der Materie unseres Universums, wie zum Beispiel den Nachweis des Elektrons, des ersten entdeckten Elementarteilchens. Im Laufe der Zeit wurden die Anforderungen an die Detektorsysteme der Experimente jedoch immer höher, um Elementarteilchen und aus ihnen zusammengesetzte Teilchen und deren Eigenschaften nachweisen zu können. Dies führte zu immer komplexeren Experimenten und zur Entwicklung neuartiger Teilchendetektoren wie der Nebelkammer, mit der erstmals Teilchenspuren fotografiert werden konnten. Die technischen Grenzen von Nebelkammern führten zu Weiterentwicklungen wie der Blasenkammer und schließlich zur revolutionären Entwicklung der Spurendriftkammer (TPC), die eine vollständig digitale Datenaufnahme ermöglicht. Fortschritte in der Leistungsfähigkeit von Rechenzentren und Rekonstruktionsprogrammen ermöglichen zudem eine automatische Rekonstruktion dreidimensionaler Teilchenspuren sowie eine präzise Bestimmung der Teilcheneigenschaften mit TPCs.

Im Rahmen dieser Arbeit werden grundlegende Korrekturen für die weltweit größte in Betrieb befindliche TPC im ALICE-Experiment am Teilchenbeschleuniger CERN-LHC entwickelt, um eine präzise Rekonstruktion von Teilchenspur und Teilchenart zu ermöglichen. Daher wird im Folgenden zunächst das ALICE-Experiment und die TPC beschrieben. Anschließend werden die entwickelten Korrekturen vorgestellt.

Das ALICE-Experiment wurde hauptsächlich zur Untersuchung von Schwerionenkollisionen entwickelt. Bei diesen Schwerionenkollisionen entsteht ein extrem heißer und dichter Materiezustand, der als Quark-Gluon-Plasma (QGP) bezeichnet wird. Es wird angenommen, dass sich die Materie unseres Universums Sekundenbruchteile nach dem Urknall in einem solchen Zustand befand. Nach der Bildung dieses extrem heißen und dichten Materiezustandes findet eine Abkühlung statt, wobei viele Teilchen entstehen, die Aufschluss über die Eigenschaften und die Evolution dieses Materiezustandes geben. Zur Untersuchung des QGPs und um Antworten auf die Fragen nach der Entwicklung des frühen Universums zu finden, werden die bei den Schwerionenkollisionen nach dem Abkühlen des QGPs entstehenden Teilchen mit der im ALICE-Experiment verwendeten TPC und weiteren Detektoren präzise rekonstruiert und anschließend analysiert.

Während der ersten beiden Datenaufnahmeperioden des ALICE-Experiments von 2010 bis 2018 wurde die TPC aufgrund der Totzeit der verwendeten Ausleseelektronik in einem getriggerten Auslesemodus betrieben, wodurch nur ausgewählte Schwerionenkollisionen aufgezeichnet werden konnten. Für die dritte Datenaufnahmeperiode, die 2022 begonnen hat, wurden umfangreiche Verbesserungen an den Detektoren vorgenommen, insbesondere an der TPC, um eine kontinuierliche Datenaufnahme zu ermöglichen. Die kontinuierliche Datenaufnahme erhöht erheblich die Anzahl der registrierten Teilchenkollisionen, sodass auch seltene Prozesse und Teilchen präzise nachgewiesen werden können. Zudem wurde die Software zur Spurrekonstruktion und Datenverarbeitung grundlegend neu entwickelt, um die erhöhten Datenströme zu verarbeiten. Diese neue Softwareumgebung, O^2, ersetzt die Softwareumgebung AliRoot, die in den beiden vorherigen Datenaufnahmeperioden verwendet wurde, und basiert auf modernen C++ und GPU-gestützten Algorithmen zur Rekonstruktion der Teilchenspuren während der Datenaufnahme. In O^2 werden die im Rahmen dieser Arbeit entwickelten Korrekturen für die TPC implementiert.

Die zylindrische TPC ist mit einer Länge und einem Durchmesser von ca. fünf Metern um den Kollisionspunkt angeordnet. Ihr Volumen ist mit einem speziellen Gasgemisch aus $Ne-CO_2-N_2$ im Verhältnis von 90-10-5 gefüllt, um einen stabilen Betrieb zu ermöglichen. Eine zentrale Hochspannungselektrode teilt das Volumen in zwei unabhängige Bereiche, die als A-Seite und C-Seite bezeichnet werden. Zusammen mit einem inneren Feldkäfig und einem äußeren Feldkäfig sorgt die zentrale Hochspannungselektrode für ein homogenes elektrisches Feld entlang der Zylinderachse. Der sogenannte L3-Magnet, in dem sich die TPC befindet, erzeugt zusätzlich ein magnetisches Feld entlang der Zylinderachse innerhalb der TPC. Ein elektrisch geladenes Teilchen, das die TPC durchquert, erfährt aufgrund der Lorentzkraft des Magnetfeldes eine Krümmung. Die Gasatome werden durch Stöße entlang der Teilchenspur ionisiert, wodurch das Teilchen einen Bruchteil seiner kinetischen Energie verliert. Der Energieverlust pro Wegstrecke hängt für eine gegebene Gasmischung im Wesentlichen nur von der Geschwindigkeit und der Ladung des Teilchens ab und wird durch die sogenannte Bethe-Bloch Formel beschrieben. Die bei den Ionisationsprozessen frei werdenden Elektronen driften aufgrund des elektrischen Feldes in Richtung von Auslesekammern, die sich an beiden Endkappen der TPC befinden. In den Auslesekammern findet zunächst eine Vervielfachung der Elektronen durch vier sogenannte Gas Electron Multiplier (GEM) statt. Diese GEMs bestehen aus 50 µm dünnen Polyimidfolien mit gleichmäßig angeordneten Löchern, umgeben von

zwei Kupferschichten. Durch Anlegen einer elektrischen Spannung zwischen den beiden Kupferschichten entsteht in den Löchern ein sehr starkes elektrisches Feld, das ausreicht, um Elektronen aus den Ionisationsprozessen um den Faktor 2000 zu vervielfachen. Die dabei entstehenden Elektronen werden auf einer segmentierten Ausleseebene detektiert, womit eine zweidimensionale Messung der Position der ursprünglichen Ionisation auf der Ausleseebene ermöglicht wird. Die z-Position wird mithilfe einer Driftzeitmessung und der mittleren Elektronendriftgeschwindigkeit berechnet. Mit diesen Positionsmessungen werden dreidimensionale Spurpunkte bestimmt, aus denen die Teilchenspuren rekonstruiert werden.
Bei den Vervielfachungsprozessen entstehen neben den Elektronen positiv geladene Ionen, die in entgegengesetzte Richtung driften und größtenteils auf einer der GEM-Schichten enden. Ein signifikanter Anteil an Ionen, der bei ca. einem Prozent der vervielfachten Elektronen liegt, tritt jedoch in das Volumen der TPC ein, was als Ionenrückfluss (IBF) bezeichnet wird. Diese Ionen driften aufgrund ihrer im Vergleich zu den Elektronen sehr hohen Masse ca. zweitausendmal langsamer als die Elektronen durch das gesamte Driftvolumen der TPC, bis sie auf die zentrale Hochspannungselektrode treffen. Während des kontinuierlichen Betriebs der TPC bilden diese Ionen eine zeitabhängige Raumladungsdichte, die zu Verzerrungen des Driftfeldes führt. Bei Schwerionenkollisionen mit Kollisionsraten von 50 kHz führen diese Driftfeldverzerrungen zu Verzerrungen der Elektronendriftstrecken um bis zu zehn Zentimetern. Die dadurch verzerrten rekonstruierten Spurpunkte werden im Folgenden vereinfachend als Verzerrungen bezeichnet. Um die intrinsische Auflösung der TPC zu gewährleisten, müssen diese Verzerrungen bei der Rekonstruktion der Teilchenspuren korrigiert werden, wofür in dieser Arbeit geeignete Korrekturmethoden vorgestellt werden.
Schon während der ersten beiden Datenaufnahmeperioden wurde eine datenbasierte Methode entwickelt, um diese Verzerrungen messen und somit korrigieren zu können. Hierzu wird zusätzlich zur TPC das innere Spurrekonstruktionssystem (ITS) verwendet, das sich bei kleinen Radien zwischen Kollisionspunkt und TPC befindet. Das ITS liefert Referenzteilchenspuren, die nicht von den Driftfeldverzerrungen der TPC betroffen sind. Durch Extrapolation dieser Referenzteilchenspuren zu den rekonstruierten Spurpunkten in der TPC werden die Abstände zwischen der extrapolierten Referenzteilchenspur und dem jeweiligen Spurpunkt berechnet. Die Messung dieser Abstände ermöglicht eine datenbasierte Methode zur Erstellung von dreidimensionalen Korrekturkarten. Im Rahmen dieser Arbeit werden auf Basis dieser Korrekturkarten dedizierte Methoden zur Korrektur der Verzerrungen entwickelt und in O^2 bereitgestellt.

Im Folgenden werden die im Rahmen dieser Arbeit durchgeführten Simulationen von Driftfeldverzerrungen, die Analyse der beobachteten Verzerrungen und die implementierten Korrekturmethoden vorgestellt.

Die bisher in AliRoot verwendeten Algorithmen zur analytischen Berechnung der Verzerrungen werden im Rahmen dieser Arbeit sowohl optimiert als auch in die neue Softwareumgebung O^2 implementiert. Mithilfe dieser Algorithmen und mit Simulationen von Schwerionenkollisionen werden analytische Modelle der erwarteten Verzerrungen aufgrund der Raumladungsdichte entwickelt. Zudem wird eine Parametrisierung des magnetischen Feldes bereitgestellt, um Verzerrungen zu berechnen, die aufgrund von Inhomogenitäten des magnetischen Feldes auftreten. Mithilfe dieser analytischen Modelle werden Aufladungseffekte am inneren Feldkäfig untersucht, die zu Verzerrungen von bis zu einem Zentimeter führen. Die Analyse dieser Verzerrungen mit einem analytischen Modell zeigt einen Anstieg der Verzerrungen mit der Interaktionsrate der Teilchenkollisionen, was mit dem Modell von Aufladungseffekten übereinstimmt.
Neben Simulationen von Driftfeldverzerrungen werden im Rahmen dieser Arbeit Methoden entwickelt, um insbesondere Änderungen der Raumladungsdichte als Funktion der Zeit präzise zu beschreiben. Diese Änderungen der Raumladungsdichte treten vorwiegend durch das Abklingen des LHC-Strahls und aufgrund von Fluktuationen in der Anzahl der Teilchenkollisionen auf. Bei Schwerionenkollisionen tragen zusätzlich die relativ großen Variationen in der Anzahl der produzierten Teilchen pro Teilchenkollision zu Änderungen der Raumladungsdichte bei. Um die Raumladungsdichte während der Datenaufnahme als Funktion der Zeit präzise zu beschreiben, werden die gemessenen Rohsignale auf der Ausleseebene über eine Millisekunde integriert. Diese integrierten Ströme (IDCs) sind direkt proportional zu den erzeugten Ionen des jeweiligen Integrationszeitfensters. Zur Speicherung der IDCs in der Online-Datenbank des Experiments und zur Verwendung für die entwickelten Korrekturmethoden werden die IDCs während der Datennahme weiterverarbeitet. Im ersten Schritt werden die IDCs über eine Zeit von ca. zehn Sekunden gemittelt. Im zweiten Schritt wird für jedes Integrationszeitfenster der mittlere IDC-Wert über alle Auslesekanäle relativ zum jeweiligen Mittelwert über zehn Sekunden berechnet. Diese eindimensionalen IDCs und die gemittelten IDCs über zehn Sekunden werden in der Online-Datenbank abgespeichert. Die eindimensionalen IDCs geben die Größe der Fluktuationen der Raumladungsdichte um den Mittelwert an und werden als Maß für Raumladungsscheiben interpretiert, die durch den IBF erzeugt werden und von der Auslese zur zentralen Hochspannungselektrode driften. Diese

Raumladungsscheiben tragen abhängig von ihrer Position im Volumen der TPC unterschiedlich stark zu den Verzerrungen bei. Die Größe des Beitrags zu den Verzerrungen in Abhängigkeit der Position der Raumladungsscheiben wird mit Daten bestimmt. Dazu werden die rekonstruierten, verzerrten Teilchenspuren zum Ort mit der geringsten Entfernung zum Kollisionspunkt extrapoliert. Der Abstand zwischen diesem Ort und dem Kollisionspunkt (DCA) wird unmittelbar durch die Größe der Verzerrungen bestimmt. Die DCAs werden in Zeitabschnitten von ca. drei Millisekunden gemittelt, um eine möglichst robuste Abschätzung für die Größe der Verzerrungen als Funktion der Zeit zu erhalten. Durch eine multidimensionale lineare Parametrisierung der DCAs mit den eindimensionalen IDCs wird der Beitrag der einzelnen Raumladungsscheiben zu den Verzerrungen in Abhängigkeit von ihrer Position in Zeitrichtung extrahiert. Es wird gezeigt, dass Raumladungsscheiben in der Nähe der zentralen Hochspannungselektrode und der Auslese einen signifikant geringeren Beitrag zu den Verzerrungen liefern als Raumladungsscheiben in der Nähe des Zentrums des Driftvolumens. Mit den extrahierten Beiträgen wird durch Kombination zweier Korrekturkarten eine dreidimensionale Korrekturkarte der Verzerrungen während der Teilchenspurrekonstruktion erstellt: Die erste Korrekturkarte beschreibt für eine gegebene Interaktionsrate die mittleren Verzerrungen. Eine zweite Korrekturkarte, die die Änderungen der Verzerrungen in Bezug auf Änderungen in der Raumladungsdichte beschreibt, wird mit den eindimensionalen IDCs, gewichtet mit ihrem jeweiligen Beitrag zu den Verzerrungen, skaliert.
Zusätzlich zu den implementierten Korrekturmethoden für Verzerrungen aufgrund der Raumladungsdichte werden in dieser Arbeit Korrekturmethoden für Verzerrungen vorgestellt, die aufgrund einer Fehlfunktion auf der A-Seite des wasserbasierten Kühlsystems entstehen und zu regelmäßig auftretenden etwa zehn Sekunden langen M-Formen in den DCAs führen. Im Folgenden werden zunächst die Ursachen dieser Verzerrungen beschrieben. Anschließend werden die dazu entwickelten Korrekturmethoden vorgestellt. Das wasserbasierte Kühlsystem verläuft entlang des inneren Feldkäfigs und wird in einem Unterdruckzustand gehalten, um ein Austreten von Wasser im Falle eines Lecks zu verhindern. Es wird angenommen, dass sich in einer Zuleitung des Kühlsystems ein Leck befindet, wodurch Luftblasen in das Kühlsystem eintreten und durch das Kühlsystem gepumpt werden. Die hohe Strahlungsbelastung während der Teilchenkollisionen könnte zu Aufladungseffekten dieser Luftblasen führen, wodurch die Luftblasen Ströme im inneren Feldkäfig induzieren würden. Die Luftblasen, die in das Kühlsystem eintreten, erhöhen zudem den Druck im Kühlsystem. Erreicht dieser Druck einen Schwellenwert, wird eine Vakuumpumpe aktiviert, die den ursprünglichen

Unterdruck wiederherstellt. Es wird eine eindeutige Korrelation zwischen der Häufigkeit dieser Verzerrungen mit dem Zeitpunkt festgestellt, an dem die Vakuumpumpe den Unterdruck im System wiederherstellt. Dies stützt die Hypothese, dass Luftblasen für diese Verzerrungen verantwortlich sind. Die zuvor vorgestellte datengetriebene Korrekturmethode eignet sich nicht für solche zeitabhängigen Verzerrungen, da sie nicht ausreichend flexibel ist, um eine hohe Anzahl an Korrekturkarten in kurzen Zeitabschnitten zu erstellen. Aus diesem Grund werden analytische Modelle verwendet, die auf wenigen Parametern basieren und in kurzen Zeitabschnitten an die gemessenen DCAs angepasst werden. Die Parameter sind in der Online-Datenbank gespeichert und werden während der Teilchenspurrekonstruktion geladen, um die benötigten Korrekturkarten zu berechnen. Ende der Datennahme 2023 wurde das Wasser aus dem Kühlsystem entfernt, um diese Verzerrungen in der weiteren Datennahme zu vermeiden.

Neben den Korrekturmethoden für Verzerrungen werden im Rahmen dieser Arbeit Korrekturen entwickelt, die eine präzise Teilchenidentifizierung ermöglichen. Bei der ersten Korrektur werden Auswirkungen der Teilchenspurtopologie und der Detektorgeometrie auf die Signalhöhe korrigiert. Hierfür werden Simulationen durchgeführt, um Auswirkungen wie den Spurwinkel oder die Nullunterdrückung auf die Signalhöhen zu simulieren und diese Auswirkungen anschließend zu parametrisieren. Diese Parametrisierungen sind in der Online-Datenbank gespeichert und werden in O^2 bei der Rekonstruktion des Energieverlustes automatisch angewendet.
Bei der zweiten Korrekturmethode wird der mittlere rekonstruierte Energieverlust der Teilchen verwendet, um eine zweidimensionale Karte mit residualen Variationen der gemessenen Signalhöhen zu erhalten. Diese zweidimensionalen Karten werden während der Datenaufnahme erstellt und in der Online-Datenbank gespeichert und können zur Korrektur der residualen Variationen und zur Qualitätskontrolle verwendet werden.

Die im Rahmen dieser Arbeit in O^2 implementierten Korrekturen werden von der ALICE-Kollaboration standardmäßig bei der Datenrekonstruktion verwendet. Die Korrektur der Verzerrungen aufgrund der zeitabhängigen Raumladungsdichte ist eine zwingende Voraussetzung für eine präzise Spurrekonstruktion und führt zu bis zu dreimal kleineren DCAs. Die Teilchenidentifizierung wäre ohne die implementierte Korrektur nicht durchführbar.

Contents

1 Introduction

In the early twentieth century, Ernest Rutherford discovered that the mass of an atom is concentrated in a nucleus [1]. For his famous experiment, alpha particles were directed at a thin gold foil. The scattered alpha particles were recorded solely by photographic plates positioned around the gold foil, enabling statistical analysis of the scattering angles. Shortly after this experiment, Charles Thomson Rees Wilson developed the first cloud chamber [2], which allowed for the measurement of full particle trajectories. The limitations of cloud chambers led to developments such as bubble chambers [3], which paved the way for the Gargamelle experiment [4] at CERN, designed to detect weakly interacting neutrinos through their interaction with nucleons. The particle tracks of the electrons produced by these interactions were visible in the detector as bubbles along the electron's trajectories and photographed by cameras located around the experiment. The time projection chamber (TPC) [5] was developed in the late 1970s, featuring groundbreaking technology at the time including a full electronic readout system, high detection efficiency and precise particle identification capabilities, especially in high track density environments. In the scope of this thesis, fundamental corrections for the TPC operated at the ALICE experiment [6, 7] at CERN are developed. The ALICE collaboration aims to study high-energy heavy-ion collisions in which an extremely hot and dense state of matter is formed. During the first two data-taking periods of the experiment, the TPC was operated in a triggered readout mode, which only allowed up to around 1000 collisions per second to be recorded. A state-of-the-art upgrade of the readout system [8] enables full continuous readout in the current data-taking period, which started in 2022, opening new possibilities in the search for rare processes. The upgrade required extensive advances in computing resources and the development of the high-performance software framework O^2 [9] for reconstruction and calibration. During continuous operation of the TPC, positive ions accumulate in the volume of the TPC, causing distortions in the measurements. In the scope of this work, corrections for these distortions and calibrations for the specific energy loss are developed and implemented in O^2. These corrections are used by the ALICE collaboration in the reconstruction of the recorded data to ensure precise tracking and particle identification capabilities.
In Section 2 of this thesis, an overview of the ALICE experiment in LHC Run 3 is given, followed by the upgraded TPC and the relevant physical principles in Section 3. The main topics of this thesis are presented in Sections 4 and 5 including observations and corrections of the distortions and the calibrations for the specific energy loss.

2 ALICE

ALICE is one of the four major experiments located underground at the CERN Large Hadron Collider (LHC) [10] in Geneva, Switzerland. With a circumference of almost 27 km, the LHC represents the world's largest particle accelerator, used to accelerate and collide protons (p) and heavy ions such as lead (Pb) nuclei. The time it takes the particles in the LHC to complete one revolution is defined as the LHC orbit duration:

$$T_{\text{orbit}} = \frac{C_{\text{LHC}}}{v_{\text{p}}} \approx \frac{C_{\text{LHC}}}{c} \approx \frac{26.659\,\text{km}}{c} \approx 88.9\,\mu\text{s}\,, \tag{2.1}$$

where:

C_{LHC} = circumference of the LHC,
v_{p} = velocity of the particles in the LHC,
c = speed of light.

The LHC has four crossing points where the particles collide. The ALICE experiment, operated at Point 2, was designed to measure particles produced in high-temperature and high-density environments, such as those occurring in heavy ion collisions. In these collisions, the constituents of the particles, the quarks and gluons, form a state of matter called quark-gluon plasma (QGP) [11]. This experimentally formed state of matter, where the fundamental particles are deconfined and no longer bound to hadrons, is expected to represent the conditions fractions of a second after the Big Bang. ALICE provides accurate measurements of the properties of the QGP, such as the temperature and energy density, to better understand the fundamental forces in our universe [12].
Figure 2.1 shows the ALICE experiment with all of its detectors. The particle collisions take place at the center of the experiment. The Inner Tracking System (ITS) [13] located around the beam pipe, shown in green, provides precise measurements of the particle tracks and the collision vertices. The cylindrical TPC [14], shown in blue, ensures excellent charged particle identification and tracking capabilities over a wide kinematic range. The Time-Of-Flight (TOF) [15] detector, shown in orange, allows precise time-of-flight measurements for particle identification. The Transition Radiation Detector (TRD) [16], shown in yellow, can be used for electron identification. The Fast Interaction Trigger (FIT) [17], consisting of the three forward detectors FT0, FV0 and FDD, provides accurate collision time and luminosity measurements. To determine the momentum and charge of the particles, the large L3 solenoid with magnetic fields of up to 0.5 T shown in red is used to bend the trajectories of charged particles.

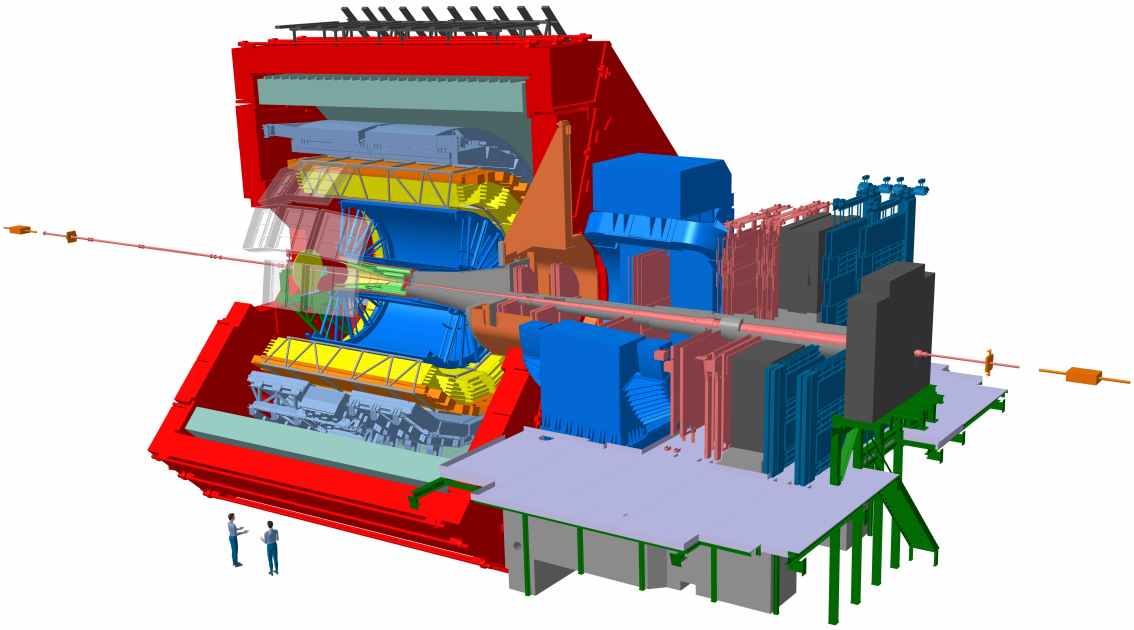

Figure 2.1: Schematic view of the ALICE experiment [18].

2.1 LHC Run 3

The LHC was first operated from 2010 to 2013 during Run 1, delivering Pb–Pb collisions with center-of-mass energies per nucleon $\sqrt{s_{\mathrm{NN}}}$ of 2.76 TeV [19]. For Run 2, from 2015 to 2018, an increase in peak luminosity and center-of-mass energies per nucleon to 5.02 TeV for Pb–Pb collisions were achieved [20]. Luminosity $\mathcal{L}$ is a measure of the ability of a particle accelerator to produce particle collisions and it translates to the number of collisions per second, the interaction rate IR, by multiplication with the cross-section σ_{p} of the collision [21]:

$$\mathrm{IR} = \mathcal{L} \cdot \sigma_{\mathrm{p}} \,. \tag{2.2}$$

The cross-section defines the probability that a process, i.e. a collision, occurs and it is typically given in units of barn (b) with 1 b = 10^{-24} cm^2. Figure 2.2 shows the integrated luminosity at Point 2 delivered by the LHC as a function of time for pp collisions in blue and for Pb–Pb collisions in red. For Run 3 [24], which started in 2022, upgrades of the LHC enable collisions at center-of-mass energies of up to 13.6 TeV in pp collisions and center-of-mass energies per nucleon of 5.36 TeV in Pb–Pb collisions. Additionally, a further increase in luminosity is achieved. Already in October 2023, the number of recorded Pb–Pb collisions exceeds those of the first two data-taking periods, as the

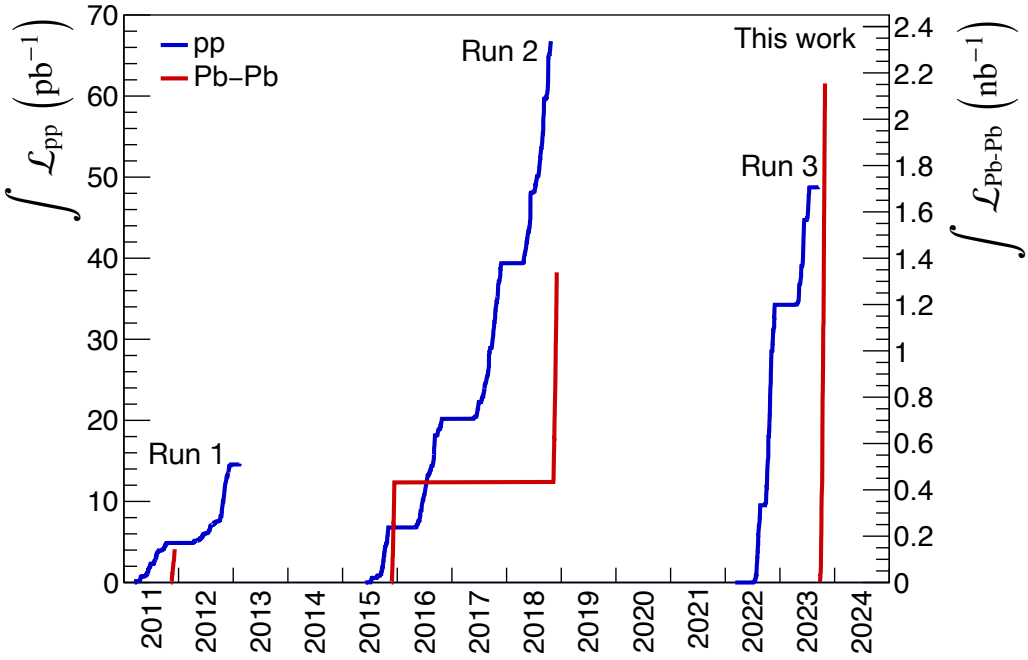

Figure 2.2: Integrated luminosity delivered by the LHC at Point 2 for pp and Pb–Pb collisions. Data taken from [22, 23].

LHC delivered Pb–Pb collisions at interaction rates up to 45 kHz at Point 2. To take full advantage of these high interaction rates, major upgrades of detectors, reconstruction software and the computing farm have been carried out to move from triggered readout to continuous readout.

2.2 Software framework O^2

High interaction rates of up to 50 kHz in Pb–Pb collisions and the continuous readout of the detectors in Run 3 lead to an increase in data throughput of up to two orders of magnitude compared to Run 1 [9]. To cope with the increased data rates, a new computing facility at LHC Point 2 and the new software framework O^2 [25] represent major parts of the upgrade for Run 3. Online data processing is achieved by graphics processing unit (GPU) based reconstruction, resulting in a reduction of the raw data rate from 3.5 TB/s to 100 GB/s compressed data written to disk.

O^2 is developed as an open-source project that provides the framework for the reconstruction, calibration and simulation for Run 3 and Run 4 and is used during the online and offline processing of the data. The software is written mainly in the C++ programming language with support for NVIDIA and Advanced Micro Devices (AMD) GPUs, but also provides full functionality on systems without a dedicated GPU. To allow

for easy maintainability, the central processing unit (CPU) and GPU implementations share the same source code. Simulation of particle production in collisions is provided by interfaces to event generators such as Pythia [26]. Transport of simulated particles through the detector material is performed by GEANT 4 [27].

2.3 Data acquisition

Stable data acquisition in Run 3 is achieved through a robust computing scheme that ensures efficient processing and compression of the recorded raw data. Raw data of about 3.5 TB/s are sent from the detectors to the computing farm of about 200 so-called First Level Processors (FLPs) located at Point 2 in the Counting Room (CR) 1, where a first reduction of the TPC data is performed by zero suppression [28]. Additionally, the data continuously received by the FLPs are divided into sub-time frames with a length of multiples of the LHC orbit duration. Since 2023, by default 32 orbits per sub-time frame are used, which corresponds to about 2.8 ms. Sub-time frames of about 630 GB/s are sent to Event Processing Nodes (EPNs) located at the computing farm at CR0. One EPN receives all sub-time frames that correspond to the same time interval. On the EPN, the sub-time frames are combined into one Time Frame (TF) with the same time length as the sub-time frames and processing such as clustering, tracking and further compression is performed. Around 250 EPNs equipped with GPUs are used to process the data online during data acquisition. After processing on the EPNs, the resulting data is stored in Compressed Time Frame (CTF) files on disk at a rate of approximately 100 GB/s. In addition, the EPNs send data to dedicated computing nodes where further processing and calibrations are performed. The resulting calibration objects are usually stored in the Condition and Calibration Database (CCDB) or as files on disk. The CTFs are used as input for an asynchronous reconstruction with updated calibration objects from the CCDB to produce the final output, which serves as input for physics analyses.
All data processed without interruption belong to the same run, which is identified by a unique increasing number. If processing is interrupted, for example due to problems in the processing chain or at the end of an LHC fill, a new run is started. The data is further classified into periods, which usually consist of several runs. Periods are named by the year of the data acquisition and an alphabetical letter, e.g. LHC23o. Typically, data that have been taken under similar conditions, such as interaction rate or collision type, are grouped into the same period.

3 The ALICE Time Projection Chamber

Due to its exceptional tracking and charged particle identification capabilities, the TPC serves as one of the most important detectors in the ALICE experiment [29].
Figure 3.1 shows a schematic view of the cylindrical TPC. The length of 5 m and the outer radius of about 2.5 m with an inner radius of about 80 cm result in an active volume of nearly 90 m^3, making it the largest TPC built to date. The central electrode operated at a nominal voltage of -100 kV divides the drift volume into the A-side pointing toward the ATLAS experiment and the C-side pointing toward the CMS experiment. The combination of the central electrode, the inner and outer field cages, and the electrodes of the readout chambers provides a homogeneous electric field of 400 V/cm within the drift volume. The volume of the TPC is filled with a specific gas mixture of $Ne-CO_2-N_2$ (90-10-5) to ensure stable measurement conditions.
A charged particle passing through the volume of the TPC loses a small fraction of its kinetic energy through ionization of the gas atoms. The produced positively charged ions drift to the central electrode. The free electrons drift in the opposite direction along the electric field lines to the readout chambers. The readout system is divided into 18 trapezoidally-shaped sectors providing full φ coverage. In the readout chambers, the electrons are amplified and measured on a segmented pad plane. The Multi-Wire Proportional Chambers used for the electron amplification in Run 1 and Run 2 have been replaced by stacks of four Gas Electron Multiplier (GEM) foils for Run 3, allowing for continuous operation of the TPC. The measured signals on the readout pads are merged to so-called clusters, providing precise space points of the particle tracks in the x-y direction. The z-coordinates of the space points are determined by a drift time measurement of the electrons and the electron drift velocity. A full particle track is reconstructed by connecting all measured three-dimensional space points of the track.
The L3 solenoid surrounding the central detectors of ALICE provides a magnetic field of up to ± 0.5 T, which bends the particle tracks due to the Lorentz force. The large readout plane allows precise determination of the curvature of the reconstructed tracks enabling accurate momentum measurements. In addition, the measured signal heights on the readout pads serve as an estimate of the energy loss per unit path length of the particle, which, in combination with the momentum measurement, allows precise particle identification. A more detailed description of the TPC, its upgrade for Run 3 and the relevant theoretical aspects are given in the following sections.

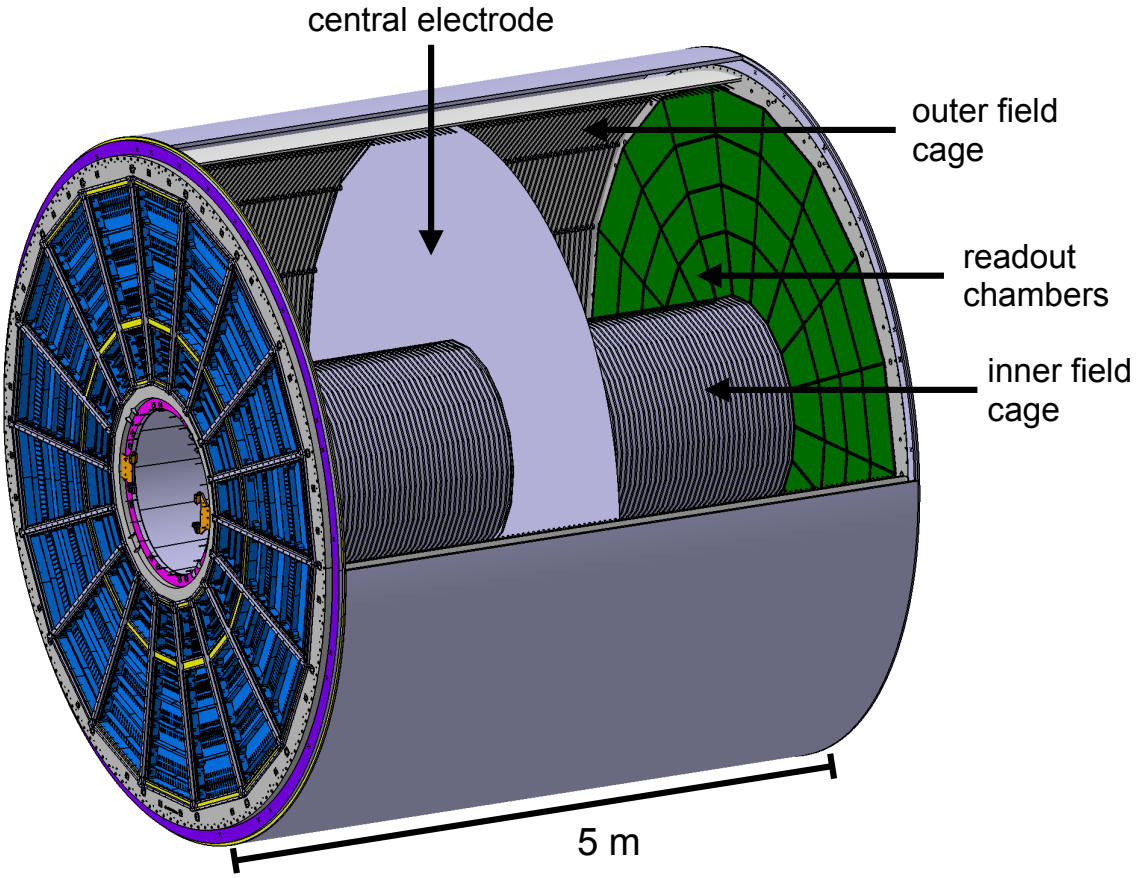

Figure 3.1: Schematic view of the ALICE TPC. Adapted from [8].

3.1 Energy loss of charged particles

Operating and designing particle detectors, such as TPCs, requires a comprehensive understanding of the physical processes involved in the movement of charged particles passing through matter. These processes are essential not only for particle detection but also for the interaction of particles with the material of the detector support structure, which can cause significant deterioration of the reconstructed particle tracks.

Charged particles passing through the active volume of the TPC lose energy through inelastic collisions with gas atoms, leading to ionization and excitation of the gas atoms [30]. These primary ionization processes occur randomly along the trajectories of the particles and result in the creation of a positive ion and the release of one or sometimes more electrons from the gas atom. If the released electron has sufficient energy, the electron can ionize further atoms in secondary ionization processes. In addition, due to Coulomb interactions of the traversing particles with gas atoms or the detector material, the trajectories of the traversing particles can change significantly as

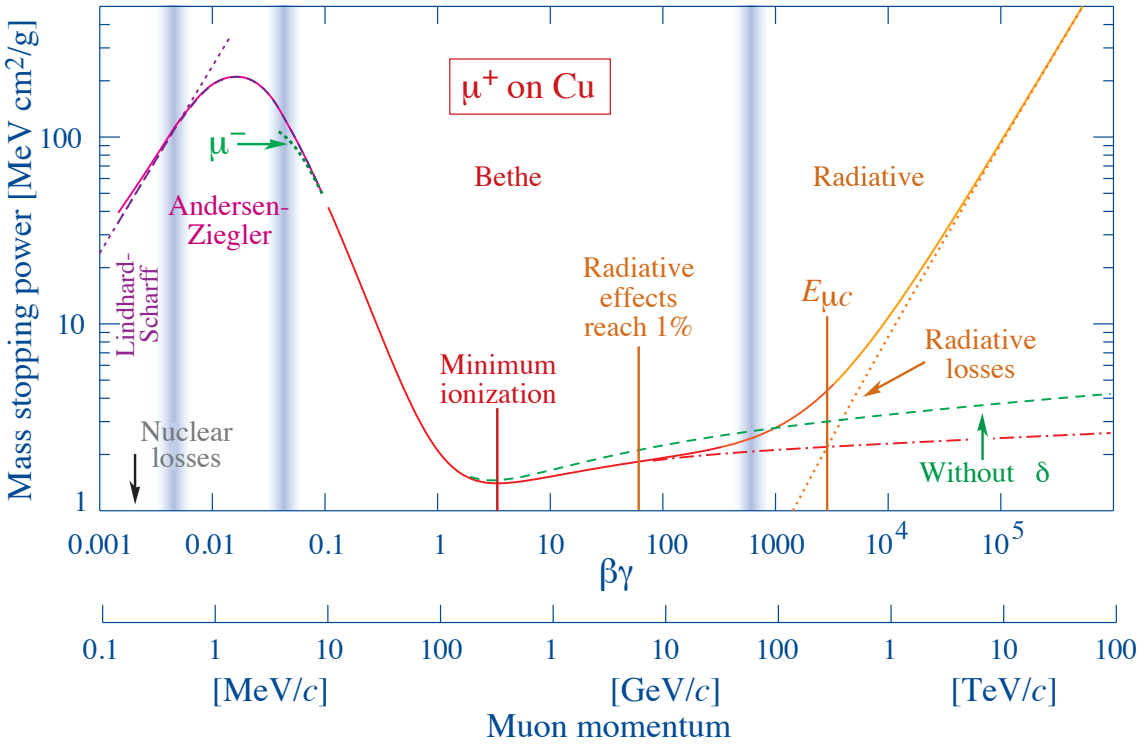

Figure 3.2: Energy loss of positive muons in copper over a wide kinematic range as a function of velocity and momentum [31]. Solid lines indicate the total energy loss. Dashed lines show single contributions to the energy loss. The most relevant energy loss for TPCs, described by the Bethe-Bloch formula, is shown as a red line.

they pass through the detector system. Each scattering process causes a small deflection of the particle's trajectory, which slightly changes the particle's path. Multiple scattering is most relevant for low-momentum tracks and needs to be carefully considered during the track reconstruction and analysis of those tracks. Figure 3.2 shows the energy loss for positive muons traversing copper as a function of the velocity $\beta\gamma$ and the momentum. In general, the energy loss strongly depends on the velocity of the particle and the traversed material. The vertical bands indicate velocity regions where a dedicated model is used to describe the energy loss:

- $0.1 \lesssim \beta\gamma \lesssim 1000$: The mean energy loss of charged particles in this velocity region for a given material depends only on the particle's velocity and charge and is most relevant for TPCs. Niels Bohr first described this energy loss with a classical approach in 1913 [32]. A quantum mechanical description was given later by Hans Bethe in 1930 [33] and extended by Felix Bloch in 1933 [34]. Fermi introduced a density correction term in 1939 to account for the polarization

of the surrounding medium, which shields the electric field of the traversing particle [35]. The Bethe-Bloch formula describes the mean energy loss dE per traveled distance dx of charged particles in a material and is given by [31]:

$$\left\langle -\frac{\mathrm{d}E}{\mathrm{d}x} \right\rangle = Kz^2 \frac{Z}{A} \frac{1}{\beta^2} \left[\frac{1}{2} \ln \left(\frac{2m_\mathrm{e} c^2 \beta^2 \gamma^2 W_\mathrm{max}}{I^2} \right) - \beta^2 - \frac{\delta\left(\beta\gamma\right)}{2} \right], \tag{3.1}$$

where:

m_e	= electron mass,
c	= speed of light,
ε_0	= vacuum permittivity,
e	= elementary charge,
r_e	= classical electron radius: $e^2/(4\pi\varepsilon_0 m_\mathrm{e} c^2)$,
N_A	= Avogadro constant,
K	= constant parameter $4\pi N_\mathrm{A} m_\mathrm{e} c^2 r_\mathrm{e}^2$,
z	= charge number of the traversing particle,
Z	= atomic number of the material,
A	= atomic mass of the material,
β	= ratio of the velocity of the particle to the speed of light: v/c,
γ	= Lorentz factor: $1/\sqrt{(1-\beta^2)}$,
W_max	= maximum energy transfer per collision,
I	= mean excitation energy,
$\delta\left(\beta\gamma\right)$	= density correction term.

The energy loss described by the Bethe-Bloch formula is shown as a red line in Figure 3.2. First, the energy loss decreases with $1/\beta^2$, reaching a minimum at about $\beta\gamma \approx 3$. Particles in the region of this minimum are called minimum ionizing particles (MIPs) and are often used for the calibration of particle detectors. The decrease in energy loss corresponds to shorter interaction times between the traversing particle and the atoms of the material [36]. Toward higher velocities, the energy loss rises due to an increase in the maximum energy transfer per collision and due to relativistic effects leading to an enhancement of the transverse electric field, described by the density correction term.

- $0.05 \lesssim \beta\gamma \lesssim 0.1$: Below the validity range of the Bethe-Bloch formula, the velocity of the traversing particle becomes comparable to the velocity of atomic

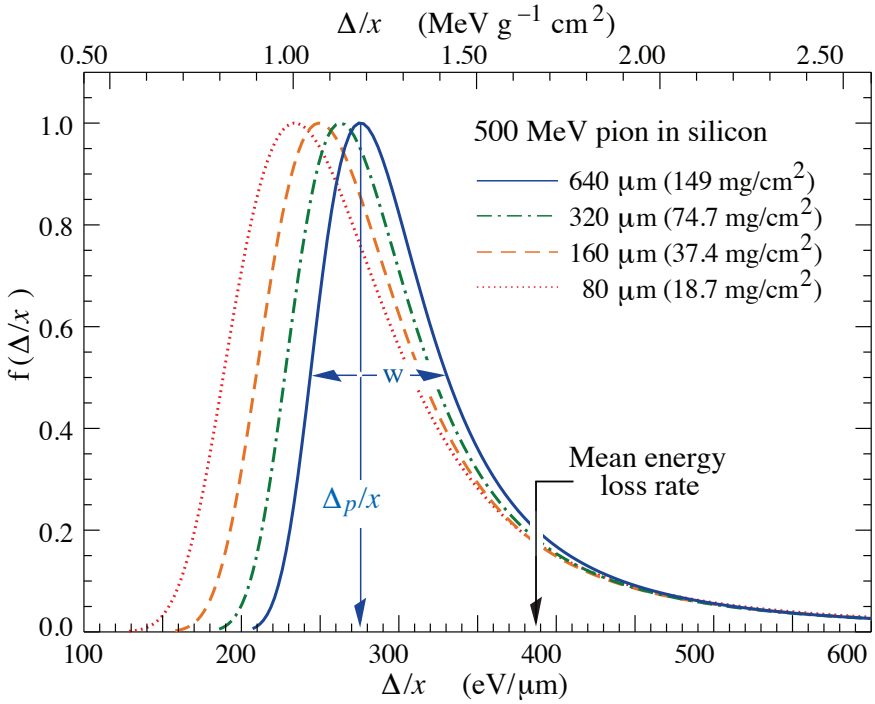

Figure 3.3: Probability distribution of the energy loss for 500 MeV pions in silicon layers of different thicknesses, normalized to unity at the most probable value [31].

electrons [37]. Therefore, correction terms are introduced into the Bethe-Bloch formula to describe the energy loss. Additionally, the sign of the charge of the traversing particle influences the energy loss, as indicated by the green dotted line in Figure 3.2 for negative muons.

- $0.01 \lesssim \beta\gamma \lesssim 0.05$: A phenomenological parameterization by Andersen and Ziegler is usually used, since no comprehensive theoretical model exists [38].
- $\beta\gamma \lesssim 0.01$: A model proposed by Lindhard is used to describe the energy loss [39].
- $\beta\gamma \gtrsim 1000$: Above the validity range of the Bethe-Bloch formula, radiative effects begin to dominate the energy loss, leading to a strong increase in the energy loss.

Figure 3.3 shows the probability distribution of the energy loss for pions with an energy of 500 MeV in silicon layers of different thicknesses between 80 μm and 640 μm. A valid approximation of this probability distribution is given by the Landau distribution which is highly skewed toward large values due to rare high-energy collisions of the traversing particle with atoms of the material [40]. During these collisions, high-energy δ-electrons are released, which usually deviate significantly from the particle's trajectory.

The asymmetry in the probability distribution needs to be carefully considered during the reconstruction of the specific energy loss of a particle, as particularly large values in the measured energy loss can introduce significant biases in the reconstructed specific energy loss if not treated properly. In Section 3.7.5, the robust procedure to reconstruct the specific energy loss applied for the ALICE TPC is described in detail.

3.2 Interactions of photons with matter

In addition to interactions of charged particles in the TPC, interactions of photons must also be taken into account, especially when considering the choice of the gas mixture [36]. Photons passing through the TPC can interact with the gas and the detector material through various processes such as the photoelectric effect, Compton scattering and pair production.
According to the Beer-Lambert law, the intensity of photons passing through matter decreases exponentially with distance:

$$N(x) = N_0 e^{-\mu x} \,, \tag{3.2}$$

where:

$N(x)$ = number of photons after distance x,
N_0 = number of photons at origin,
μ = attenuation coefficient,
x = traversed distance of the photon.

The material-dependent attenuation coefficient is proportional to the absorption cross-section and describes the inverse of the mean free path. Normalizing the attenuation coefficient to the density ρ of the material yields the mass attenuation coefficient μ_m expressed in units of cm^2/g:

$$\mu_\mathrm{m} = \mu/\rho \,. \tag{3.3}$$

Figure 3.4 shows the mass attenuation coefficient for photons in $\mathrm{Ne}-\mathrm{CO}_2-\mathrm{N}_2$ (90-10-5) for the photoelectric effect as red markers, for Compton scattering as green markers and for pair production as blue markers as a function of the energy of the photon. The total mass attenuation coefficient is shown as black markers. The lines indicate interpolations between the data points. For energies below 1 keV, only the mass attenuation coefficient

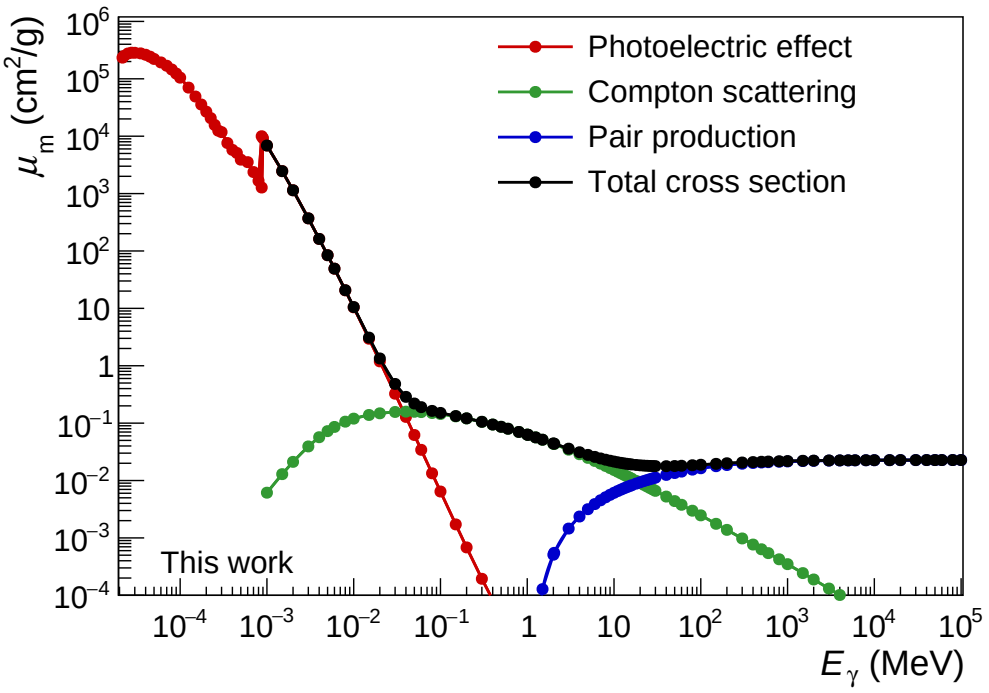

Figure 3.4: Mass attenuation coefficient for photons in Ne−CO_2−N_2 (90-10-5) for the photoelectric effect, Compton scattering, pair production and the total mass attenuation coefficient as a function of the energy of the photon. Values above 1 keV are taken from XCOM: Photon cross-sections Database. For photon energies below 1 keV, the mass attenuation coefficient for the photoelectric effect is shown using tabulated data from the NIFS database. The colored lines indicate interpolations of the data points. Data taken from [41, 42].

for the photoelectric effect is shown with data provided by the National Institute for Fusion Science (NIFS). In the following, the mass attenuation coefficient serves as a measure of the absorption cross-section and is used interchangeably. In general, the absorption cross-section strongly depends on the energy of the photon. For energies below 0.1 MeV the photoelectric effect dominates. For intermediate energies in the range of 0.1 MeV $\lesssim E_\gamma \lesssim$ 20 MeV mainly Compton scattering contributes to the total cross-section. At higher energies above 20 MeV pair production begins to dominate.

3.2.1 Photoelectric effect

The photoelectric effect describes the process by which a photon transfers all of its energy to an atom, leading to the release of a bound electron from its shell. For this process, the required energy of the photon E_γ needs to be larger than the binding energy of the electron E_B. The transferred energy to the released electron corresponds

to $E_e = E_\gamma - E_B$. The cross-section of the photoelectric effect $\sigma_{p.e.}$ scales with the nuclear charge number Z and the energy of the photon according to the relation:

$$\sigma_{p.e.} \propto Z^5 / E_\gamma^{3.5}. \tag{3.4}$$

When the energy of the photon corresponds to the binding energy of the outermost electron shell of the atom, the cross-section becomes largest. As the photon energy increases, the cross-section decreases proportional to $1/E_\gamma^{3.5}$ until the photon energy reaches the binding energy of the next inner electron shell, leading to a sharp rise in the cross-section. After an electron is emitted from its shell, the resulting hole is filled by an electron from a higher shell, leading to the emission of a photon or an Auger electron with a discrete energy value.

3.2.2 Compton scattering

Compton scattering describes the effect of inelastic scattering of a photon by a quasi-free electron. Electrons bound to an atomic nucleus can be considered free if their energy is negligible compared to the energy of the photon. During the inelastic scattering process, the photon transfers a fraction of its energy to the electron. The energy transferred to the electron depends only on the scattering angle θ of the photon, reaching a maximum at a 180° backscattering angle. The energy of the photon after the scattering process E'_γ can be expressed as:

$$E'_\gamma = \frac{E_\gamma}{1 + \frac{E_\gamma}{m_e c^2}\left(1 - \cos\left(\theta\right)\right)}. \tag{3.5}$$

3.2.3 Pair production

A photon with an energy greater than twice the rest mass energy of an electron can convert into an electron-positron pair in the Coulomb field of a nucleus. In the TPC, direct photon measurements are achieved by reconstructing the produced electron-positron pair and matching the electron and positron to the same vertex. This approach provides exceptional resolution of the photon's momentum, particularly at low transverse momenta [43].

3.3 Movement of charge carriers through gas

The drift path of an electron or ion, released by an ionization process of a charged particle or a photon, is determined by the electric and magnetic fields inside the TPC. The resulting equation of motion is described by the Langevin equation [30]:

$$m\frac{\mathrm{d}\vec{v}}{\mathrm{d}t} = q\vec{E} + q[\vec{v}\times\vec{B}] - K\vec{v}\,, \tag{3.6}$$

where:

m = mass of the particle,
t = drift time,
$\vec{v}$ = velocity vector,
q = electric charge of the particle,
$\vec{E}$ = electric field,
$\vec{B}$ = magnetic field,
K = friction coefficient.

The term $K\vec{v}$ takes into account the frictional force between collisions of the charge carrier with gas atoms. By introducing the parameter $\tau = m/K$, which can be interpreted as the average time between collisions of the charge carrier with gas atoms, and for $t \gg \tau$, the solution of Equation 3.6 becomes a steady state for which $\frac{\mathrm{d}\vec{v}}{\mathrm{d}t} = 0$. Thus Equation 3.6 can be rewritten as:

$$\frac{\vec{v}}{\tau} - \frac{q}{m}[\vec{v}\times\vec{B}] = \frac{q}{m}\vec{E}\,. \tag{3.7}$$

It can be shown that this equation can be solved for $\vec{v}$ [30]:

$$\vec{v} = \frac{q}{m}\tau|\vec{E}|\frac{1}{1+\omega^2\tau^2}\left[\hat{E} + \omega\tau[\hat{E}\times\hat{B}] + \omega^2\tau^2\left(\hat{E}\cdot\hat{B}\right)\hat{B}\right], \tag{3.8}$$

where $\hat{E} = \vec{E}/|\vec{E}|$ and $\hat{B} = \vec{B}/|\vec{B}|$ denote the unit vectors and ω the cyclotron frequency:

$$\omega = \frac{q}{m}|\vec{B}|\,. \tag{3.9}$$

In the case of a magnetic field, the dimensionless term $\omega\tau \neq 0$ defines the drift direction of the charge carrier. For small $\omega\tau$, the drift tends to be along the direction of the electric field whereas, for larger $\omega\tau$, the drift tends to be aligned with the direction of the magnetic field. In case no magnetic field is applied, $\omega\tau$ vanishes and Equation 3.8

can be expressed in terms of the mobility $\mu = \tau q/m$ as:

$$\vec{v} = \frac{q}{m}\tau\vec{E} = \mu\vec{E}\,. \tag{3.10}$$

A more detailed discussion of the movement of charge carriers through gas is given in [30].

3.3.1 Drift-field distortions

In real TPCs, the electric and magnetic fields are not perfectly aligned in the z-direction. For small drift distances $\mathrm{d}z$ where the electric and magnetic field inhomogeneities are rather small, Equation 3.8 can be simplified by neglecting higher order terms [44]:

$$\delta_{\mathrm{r}} = c_0 \int \frac{E_{\mathrm{r}}}{E_{\mathrm{z}}}\mathrm{d}z + c_1 \int \frac{E_{\varphi}}{E_{\mathrm{z}}}\mathrm{d}z - c_1 \int \frac{B_{\varphi}}{B_{\mathrm{z}}}\mathrm{d}z + c_2 \int \frac{B_{\mathrm{r}}}{B_{\mathrm{z}}}\mathrm{d}z\,, \tag{3.11a}$$

$$\delta_{\mathrm{r}\varphi} = c_0 \int \frac{E_{\varphi}}{E_{\mathrm{z}}}\mathrm{d}z - c_1 \int \frac{E_{\mathrm{r}}}{E_{\mathrm{z}}}\mathrm{d}z + c_1 \int \frac{B_{\mathrm{r}}}{B_{\mathrm{z}}}\mathrm{d}z + c_2 \int \frac{B_{\varphi}}{B_{\mathrm{z}}}\mathrm{d}z\,, \tag{3.11b}$$

$$\delta_{\mathrm{z}} = \int \frac{v'(E)}{v_0}\,(E - E_0)\,\mathrm{d}z\,, \tag{3.11c}$$

where:

$\delta_{\mathrm{r,r}\varphi,\mathrm{z}}$ = distortion of the drift path due to the electric and magnetic field components,
c_0 $= 1/\left(1+\omega^2\tau^2\right)$,
c_1 $= \omega\tau/\left(1+\omega^2\tau^2\right)$,
c_2 $= \omega^2\tau^2/\left(1+\omega^2\tau^2\right)$,
$\mathrm{d}z$ = passed distance of the drifting charge carrier,
E_0 = nominal electric field,
v_0 = drift velocity for the nominal electric field without a magnetic field,
$v'(E)$ = change in the drift velocity around the nominal electric field.

Equations 3.11a–3.11c yield, for a passed distance $\mathrm{d}z$ of the charge carrier, the distortion of the drift path due to the inhomogeneities of the field components. These distortions are referred to as space-point distortions as the reconstructed three-dimensional positions would deviate from the true position of the particle's trajectory without proper correction procedures.
Correcting these space-point distortions, which can be caused for example by positive ions that are produced in the readout chambers as described in Section 3.4.1, poses one of the most challenging tasks to achieve precise tracking in Run 3.

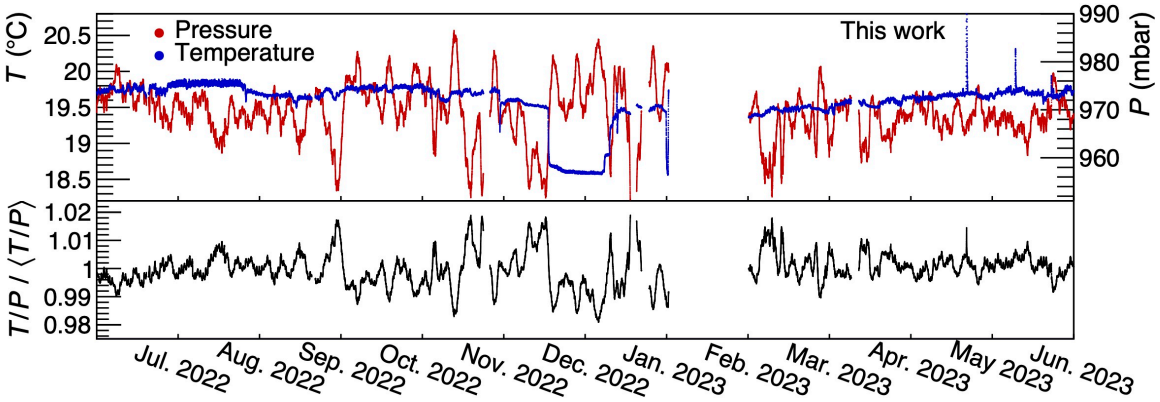

Figure 3.5: Top: Measured pressure and temperature in the TPC as a function of time. Bottom: Normalized ratio of temperature to pressure.

3.3.2 Ion drift velocity

While the electron drift velocity in electric fields for specific gas mixtures can be simulated by using common toolkits such as Garfield [45] or Magboltz [46], the ion drift velocity has to be obtained by measurements. The reduced ion mobility $\mu_{\text{ion},0}$ in $\text{Ne}-\text{CO}_2-\text{N}_2$ (90-10-5) can be described by the ion mobility μ_{ion} for a specific temperature T and pressure P of the gas and has been experimentally determined as [47]:

$$\mu_{\text{ion},0} = \mu_{\text{ion}} \frac{273.15\,\text{K}}{T} \frac{P}{1013\,\text{mbar}} = (2.92 \pm 0.04)\,\frac{\text{cm}^2}{\text{Vs}}\,. \tag{3.12}$$

Figure 3.5 shows the measured pressure in red and the temperature in blue in the TPC as a function of time in the top panel and the ratio of temperature to pressure normalized to the average ratio in the bottom panel, with maximum variations of the ratio of about 2%. Under typical conditions during the operation of the TPC, the ion drift velocity can be approximated using Equation 3.10 by assuming an ideal electric field $E = (0, 0, E_z)$ and vanishing $\omega\tau$ due to the large mass of the ions:

$$\begin{aligned} v_{\text{ion,z}} &= \mu_{\text{ion}} E_z \\ &= \mu_{\text{ion},0} \cdot \frac{T}{273.15\,\text{K}} \cdot \frac{1013\,\text{mbar}}{P} \cdot E_z \\ &= (2.92 \pm 0.04)\,\frac{\text{cm}^2}{\text{Vs}} \cdot \frac{292.92\,\text{K}}{273.15\,\text{K}} \cdot \frac{1013\,\text{mbar}}{971.99\,\text{mbar}} \cdot 400\,\text{V/cm} \\ &= (1.30 \pm 0.02)\,\text{cm/ms}\,. \end{aligned} \tag{3.13}$$

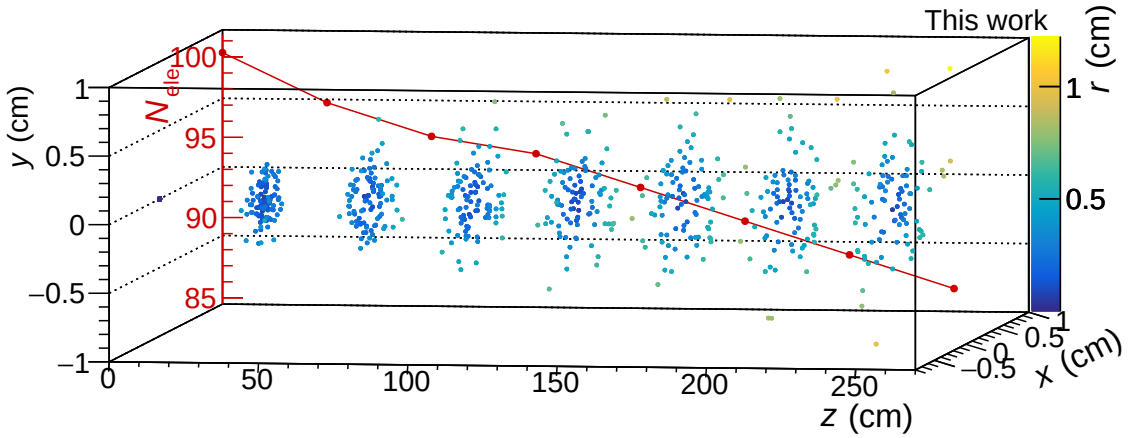

Figure 3.6: Simulation of the diffusion and attachment of drift electrons in the TPC as the electrons drift toward the readout chambers for an oxygen content of 5 ppm and an attachment coefficient of $R = 250\,\mathrm{m}^{-1}$. The red markers show the number of electrons, which decreases due to the attachment of electrons to electronegative molecules like oxygen.

3.3.3 Diffusion of drift electrons

The electrons that drift along the electric field lines toward the readout chambers are considered as electron clouds, which are subject to a stochastic diffusion process that leads to an expansion of the electron clouds in the transverse and longitudinal directions. The diffusion is mainly driven by random collisions of the electrons with gas atoms and by their thermal motion. Appropriate treatment of electron diffusion is crucial for achieving high-precision track reconstruction and accurate particle identification.
The density distribution n of the electrons after the drift time t can be expressed with the electron drift velocity v_{ele}, the longitudinal diffusion coefficient D_{L} and the transverse diffusion coefficient D_{T}, which describe the strength of the diffusion in the corresponding direction, in the following form [30]:

$$n(t) = \frac{1}{\sqrt{4\pi D_{\mathrm{L}} t}} \left(\frac{1}{\sqrt{4\pi D_{\mathrm{T}} t}} \right)^2 \exp\left[-\frac{x^2 + y^2}{4 D_{\mathrm{T}} t} - \frac{(z - v_{\mathrm{ele}} t)^2}{4 D_{\mathrm{L}} t} \right]. \tag{3.14}$$

Figure 3.6 shows a simulation of the diffusion process for one hundred electrons which start at the same origin in the TPC and drift toward the readout chambers. The color indicates the distance $r = \sqrt{x^2 + y^2 + (z - v_{\mathrm{ele}} t)^2}$ to the position without diffusion. The number of electrons, which decreases due to attachment to electronegative molecules, is also shown as red markers.

3.3.4 Electron attachment

In addition to diffusion, the drift electrons can attach to electronegative molecules such as oxygen or water, leading to the formation of negative ions. These molecules can be present as impurities in the TPC gas and are removed in the TPC gas system by copper catalysts [29]. The gas system circulates the gas in the TPC and provides periodic measurements of the gas composition. The electron attachment rate R can be expressed in terms of the density of the attaching molecule N and the attachment coefficient k [30]:

$$R = N \cdot k \, . \tag{3.15}$$

3.4 Readout chambers

The amplification of the drift electrons and the subsequent measurement of the amplified electrons are carried out within the readout chambers. For Run 3, the Multi-Wire Proportional Chambers used in Run 1 and Run 2 were replaced by stacks of four GEMs to allow for continuous operation of the TPC [29].
The readout chambers are divided into Inner Readout Chambers (IROCs) and Outer Readout Chambers (OROCs), which are arranged in 18 trapezoidally-shaped sectors on each TPC side. Figure 3.7 shows a schematic view of a sector in the local coordinate system with the four readout chambers IROC, OROC 1, OROC 2 and OROC 3. The pad plane on which the signals are measured is divided into ten regions of specific pad sizes. The digitization of the signals on the pads is performed at a sampling rate of 5 MHz by custom front-end cards (FECs). Each FEC processes the signals from 160 pads, resulting in 91 FECs per sector. The signals of the pads processed by the same FEC are distinguished by blue lines in Figure 3.7. The FECs send the digitized signals to the Common Readout Units (CRUs) where further processing such as pedestal subtraction, zero suppression, common-mode and ion tail correction takes place. The common-mode and ion tail corrections are briefly described in Section 3.7.6.

3.4.1 Gas Electron Multiplier

For Run 3, stacks of four GEMs are used for the electron amplification [8]. These GEMs are made of 50 µm thin polyimide (kapton) foils surrounded by two copper layers. The electron amplification takes place in double-conical holes in the foils as shown in Figures 3.8a and 3.8b. By applying a potential difference of about 300 V between the

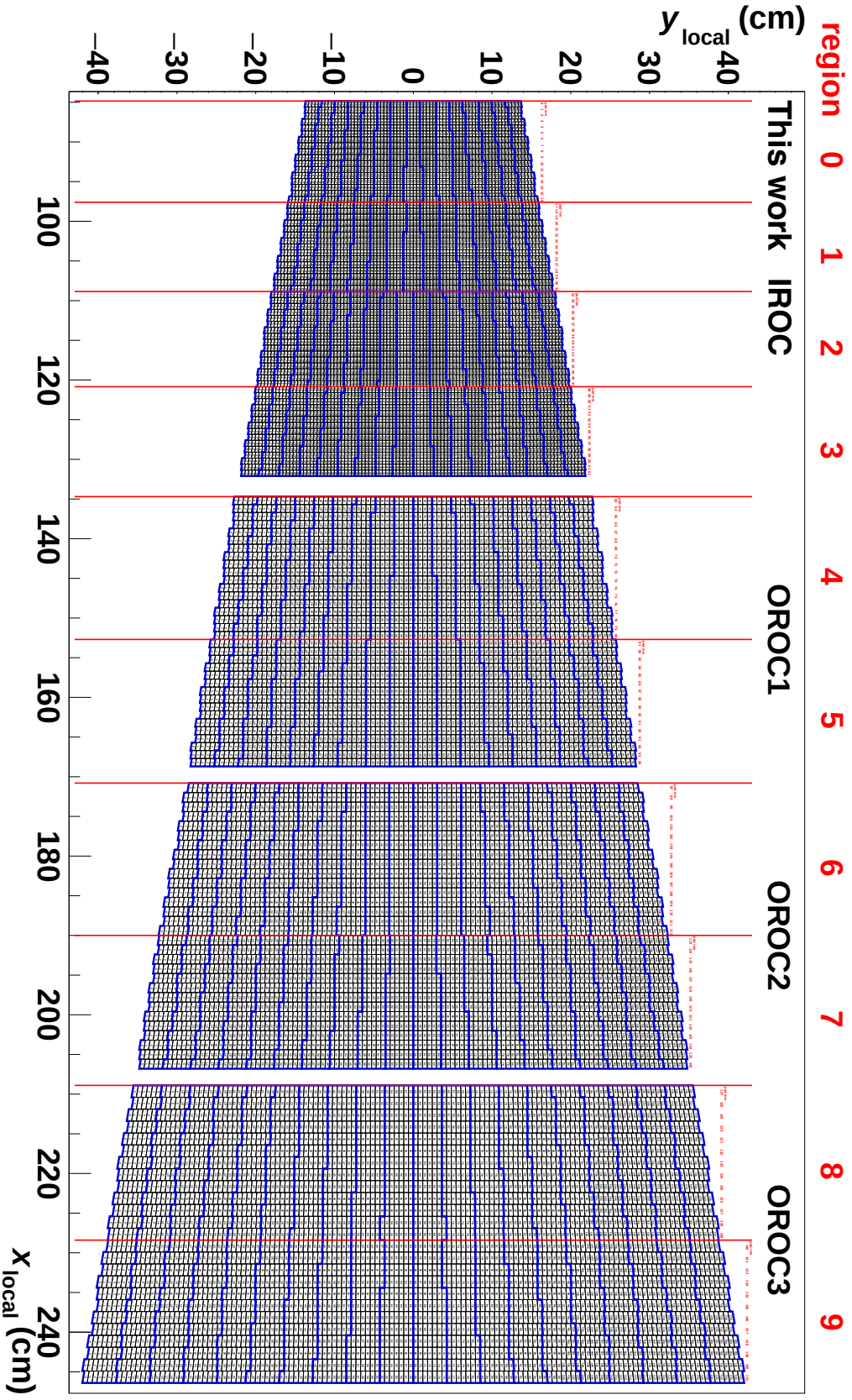

Figure 3.7: Schematic view of the readout plane of a TPC sector.

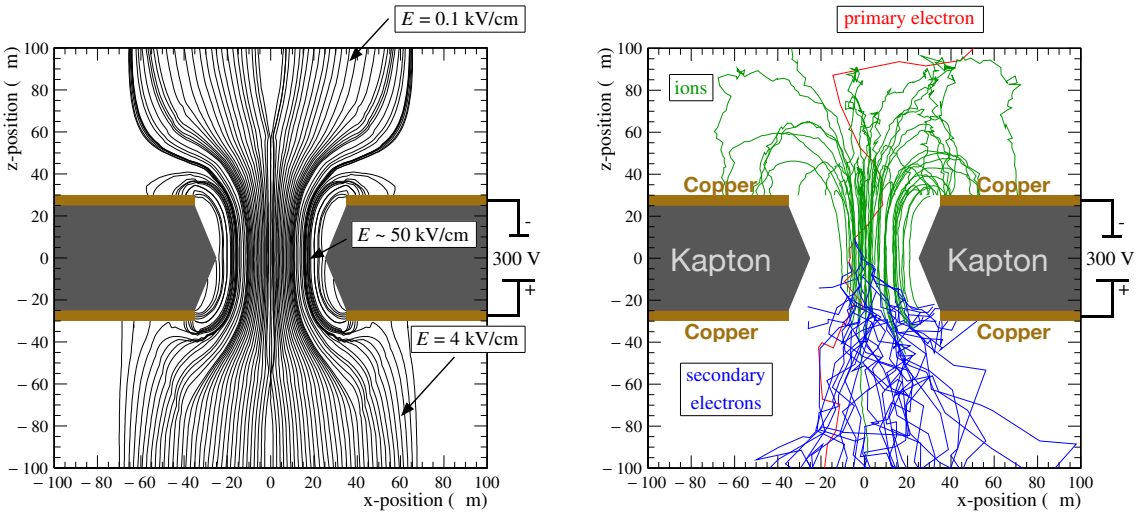

(a) (b)

Figure 3.8: (a) Electric field lines in a GEM hole when a potential difference of 300 V is applied between the upper and lower copper layers [48]. (b) Amplification of a primary electron in a GEM hole. Adapted from [48].

top and bottom copper layers, an electric field of about 50 kV/cm is generated inside the GEM holes, shown as black lines in Figure 3.8a. Figure 3.8b shows the simulation of a primary electron entering the GEM hole as a red line. The primary electron gets accelerated inside of the GEM hole and produces an avalanche of secondary electrons in ionization processes shown as blue lines. The number of secondary electrons dN is determined by the number of initial electrons N and the first Townsend coefficient α, which describes the number of electron-ion pairs generated per unit path ds as [30]:

$$\mathrm{d}N = N\alpha\mathrm{d}s. \tag{3.16}$$

The Townsend coefficient is typically measured for a given gas mixture as no fundamental description exists. In general, however, the Townsend coefficient depends on the gas mixture, the applied electric field and the ratio of temperature to pressure.

During amplification of the electrons, ultraviolet photons can be produced by the excitation of gas atoms. These photons can move away from the original electron avalanche and they can create, through the photoelectric effect, a free electron that starts a new avalanche of electron amplification. To prevent such processes, which can lead to discharges between GEM foils, a quench gas such as CO_2, C_2H_6 or CH_4 is commonly added to the gas mixture. These quench gases have larger photoabsorption cross-sections than the noble gases used as the main component of the gas mixture.

The positively charged ions produced during the ionization processes are shown as green lines in Figure 3.8b. While most of these ions end up on the top copper layer, a significant fraction enters the drift volume of the TPC, referred to as ion backflow (IBF). The IBF is defined as the ratio of the number of back drifting ions ε per electron entering the GEM system to the effective gain G_{eff}, the number of electrons producing the signal [29]:

$$\text{IBF} = (1 + \varepsilon) / G_{\text{eff}} \,, \tag{3.17}$$

where the average effective gain is around 2000 for the nominal GEM voltages. The addition of one ion takes into account the ion created in the primary ionization process. The time $t_{\text{d,ion}}$ until the back drifting ions reach the central electrode is defined by the ion drift velocity and the distance L_{TPC} of the central electrode to the GEM stacks as:

$$t_{\text{d,ion}} = \frac{L_{\text{TPC}}}{v_{\text{ion,z}}} = \frac{250\,\text{cm}}{(1.30 \pm 0.02)\,\text{cm/ms}} = (192.30 \pm 2.96)\,\text{ms} \,. \tag{3.18}$$

The drifting ions cause inhomogeneities in the electric field, leading to distortions of the nominal drift path of the electrons as described in Section 3.3.1, which are referred to as space-charge distortions in the following. In Run 3, these space-charge distortions are the main contributor to the space-point distortions at the nominal interaction rates. Figure 3.9 shows a simulation of the complete amplification process in the GEM stack for three primary electrons. The electrons from ionization processes are shown as blue lines. In each GEM foil, the electrons are further multiplied until they reach the pad plane where they generate the signals. The ions, shown as green lines, drift toward the drift volume of the TPC and then to the central electrode. In order to keep the IBF below 1% to reduce the space-charge distortions, several optimizations were found during the research and development (R&D) of the readout chambers [29]:

1. Using a stack of four GEMs: Extensive studies were carried out to optimize the number of GEMs used in a stack. It is found that a stack of three GEMs does not sufficiently suppress the IBF. By using a stack of four GEMs, the IBF and energy resolution requirements can be met.

2. Optimization of the voltage configurations: The voltages at which the GEMs are operated directly determine the gain and the IBF of each GEM foil. By performing scans on the voltages, optimal configurations are found that sufficiently suppress the IBF while maintaining the required energy resolution.

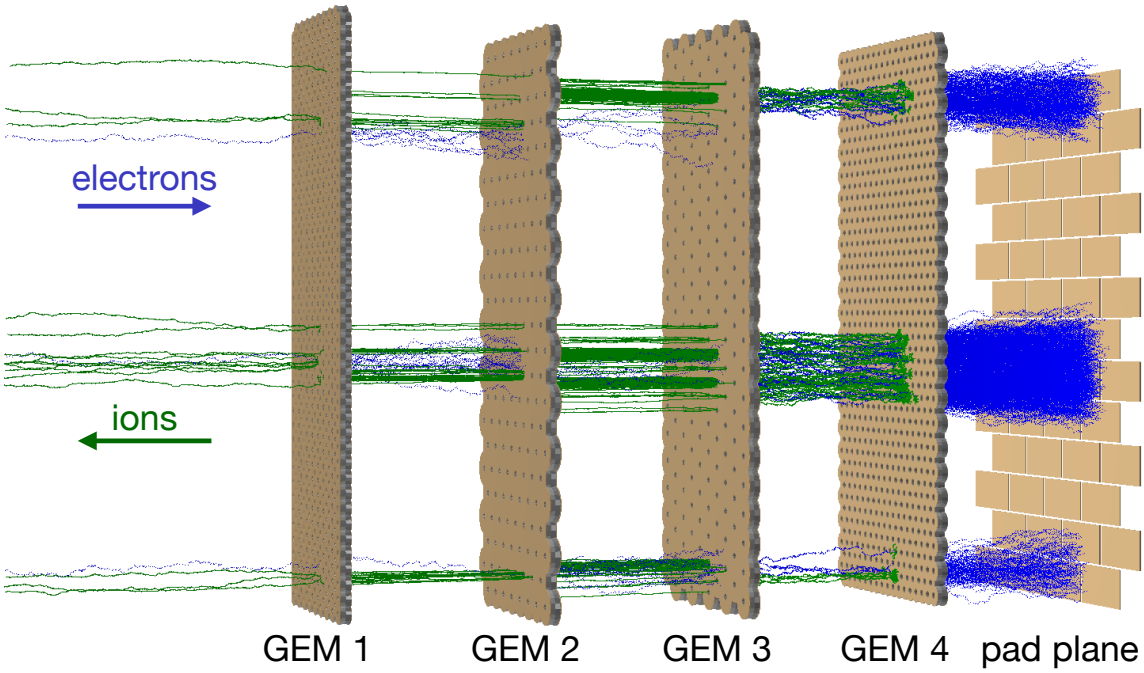

Figure 3.9: Simulation of the produced electrons and ions during ionization processes in the GEM stack [49].

3. Standard and large pitch GEMs: It is found that the IBF can be further optimized by using two standard pitch (S) and two large pitch (LP) GEM foils with different hole pitches of 140 µm and 280 µm in an S-LP-LP-S configuration.

3.4.2 Manufacturing process

The production of the GEM foils has been carried out by the CERN Micro-Pattern Technologies laboratory employing a single-mask technique [8]. Figure 3.10 schematically shows the production steps of a GEM foil [50, 51]:

1. Production of kapton foils which are surrounded by copper layers and coated with photoresistive material and masking of the hole pattern.
2. Exposing the unmasked photoresistive material on the top side to ultraviolet light.
3. Etching of the exposed top copper layer by liquid acid.
4. Etching of the kapton foil to a single conical shape.
5. Etching of the bottom copper layer by using the etched kapton as the mask.
6. Production of double-conical holes by etching the kapton foil.

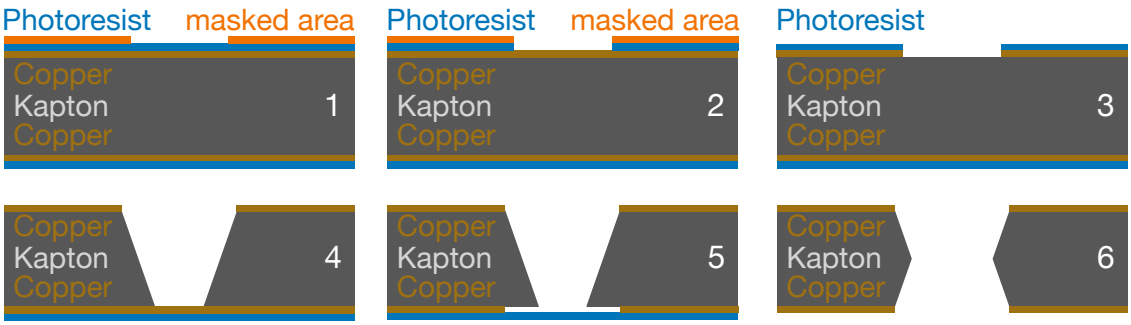

Figure 3.10: Illustration of the production steps of a GEM foil using the single mask technique.

This processing scheme allows for the production of the large-area GEMs that are used in the ALICE TPC. However, imperfections in the etching process lead to variations in hole size and shape, resulting in local variations in gain and IBF.
Figure 3.11 shows a technical drawing of an IROC. Each GEM foil is stretched and mounted on a GEM frame, which is made of an insulating material and consists of a 1.5 mm wide spacer cross. This spacer cross provides the necessary stability to prevent the GEM foils from approaching each other. The GEMs and the segmented pad plane, made of a multilayer printed circuit board (PCB), are attached to an aluminum body that not only provides the mechanical stability to hold the GEM foils, but also serves a cooling system. A fiberglass strongback guarantees insulation of the pad plane from the aluminum body.

3.4.3 Quality assurance

Extensive quality assurance (QA) has been carried out to validate the performance of the readout chambers, such as gain and IBF [8]. Local variations in gain and IBF are expected due to the stretching of the GEM foils on the frame, hole diameter variations due to the precision of the manufacturing process, the spacer crosses in the GEM frames and other effects such as sagging of the GEM foils. In order to quantify these effects, dedicated measurements are taken during the QA in a test facility, where the readout chambers are placed in a vessel filled with the nominal gas mixture. The electric field for the drift length of around 10–25 mm is provided by a cathode. An entrance window allows the active volume to be irradiated such that electrons from ionization drift to the readout chambers where the amplified electrons induce signals on the pad plane. By using custom grounding cards, all the pads are connected and their combined signal is read out at once.

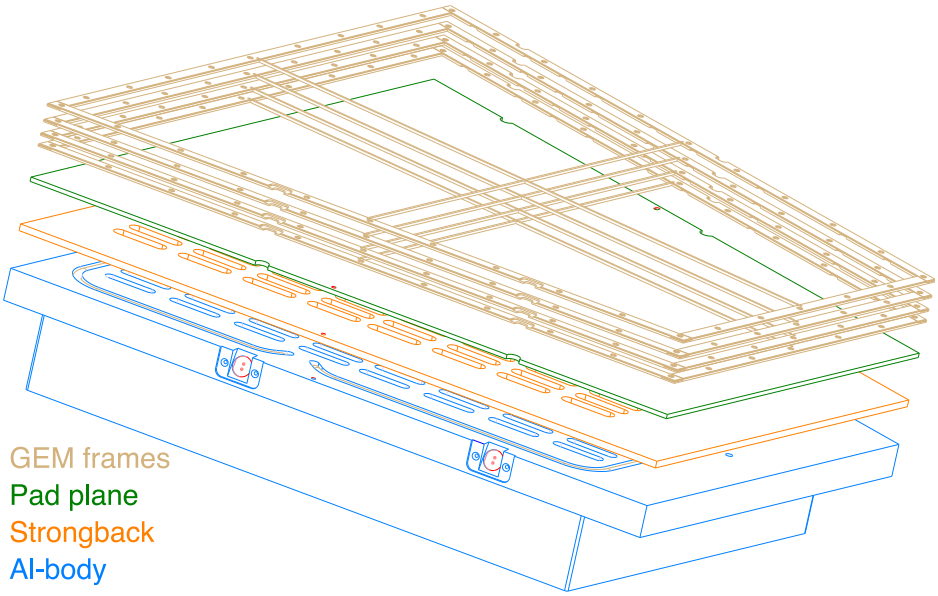

Figure 3.11: View of the IROC components [8].

For the measurements, a radioactive ^{55}Fe source is used to ionize the gas in the test setup. The radioactive iron decays to the stable isotope ^{55}Ma with a half-life of 2.75 years by mainly electron capture from the K-shell [52]. The K-shell is filled by an electron from a higher shell, resulting in the emission of a 5.19 keV Auger electron, with a probability of 60%. The emission of a photon occurs with a probability of 28%. Since the energies of the emitted photons for the $K_{\alpha 1}$ and $K_{\alpha 2}$ transitions are both close to 5.9 keV, the emitted photons are considered monoenergetic. Other low-energy transitions, which account for the remaining 12%, are not considered here. In the test facility, only the monoenergetic photons reach the active volume of the detector, leading to the ionization of single gas atoms as described in Section 3.2. For the measurements, the source was moved in steps of around 2.5 cm above the pad plane. For each step, the currents created by the electrons on the pads, I_{A}, and by the back drifting ions on the cathode, I_{C}, are measured. By using these measured currents, the IBF is defined as:

$$\mathrm{IBF} = I_{\mathrm{C}}/I_{\mathrm{A}}\,. \tag{3.19}$$

Figures 3.12a and 3.12b show the currents I_{A}, normalized to the average currents of each stack, which are used as an approximation of the relative gain G_{rel} for the A-side and C-side of the TPC. Values for each pad are obtained by interpolating the measurements. The small vertical and horizontal areas within a sector with low gain are caused by

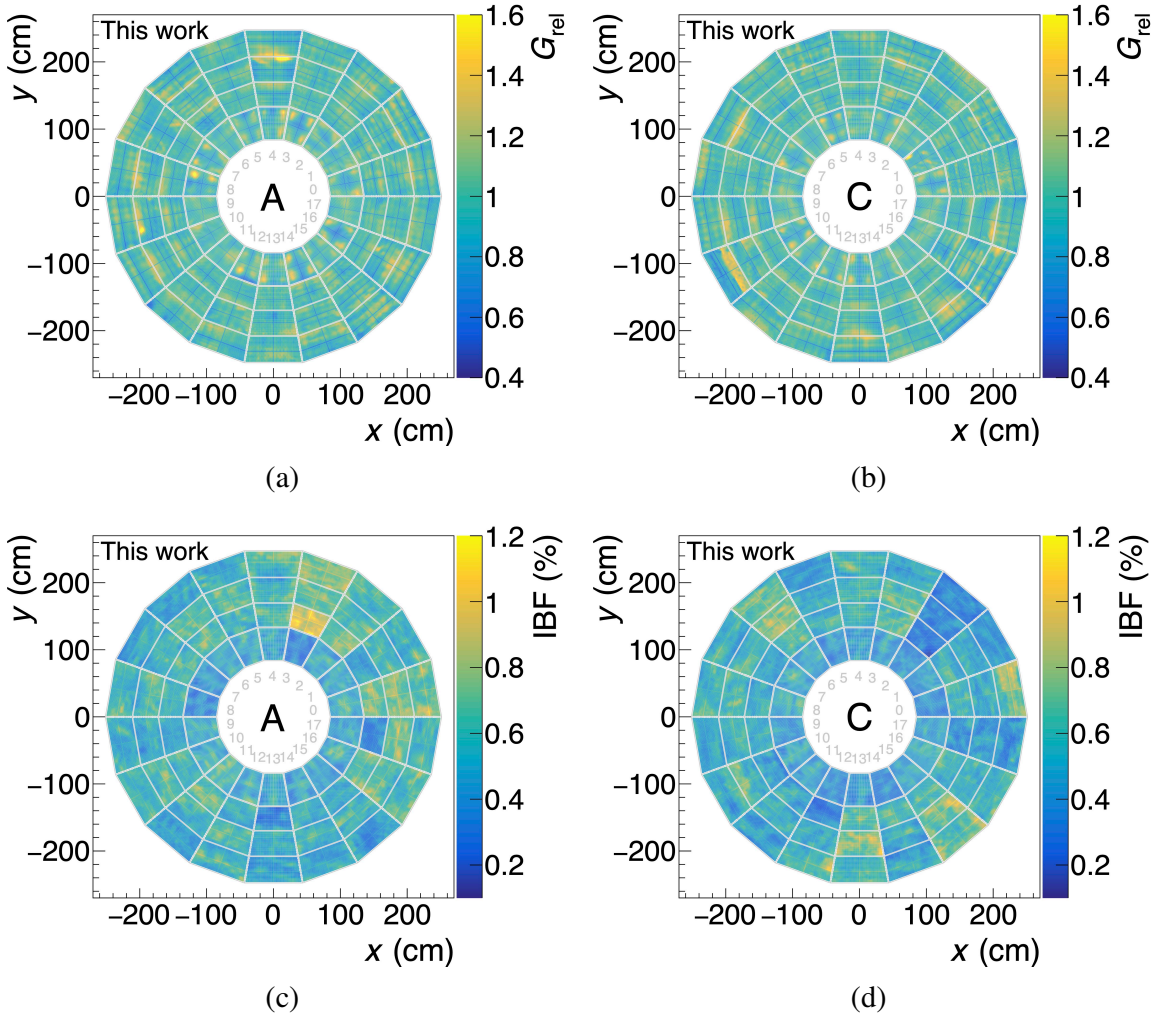

Figure 3.12: Relative gain G_{rel} of the readout chambers for the (a) A-side and (b) C-side and the IBF for the (c) A-side and (d) C-side. The values are obtained by interpolating data from measurements made during QA.

the spacer cross, which significantly reduces the gain in these areas. In the region of the edges in the IROCs, larger areas with high gain occur. Hotspots with high gain are also visible for example in the IROC at sector 1 on the C-side at the border to sector 2. Later, during the commissioning of the TPC, more accurate relative gain maps for correcting local gain variations were obtained by the krypton calibration method [53], which is briefly described in Section 3.7.6. Figures 3.12c and 3.12d show the IBF from Equation 3.19 which is on average well below 1%. The IBF shows significant variations between readout chambers, for example in the IROC for the third sector on the A-side and the neighboring OROC 1.

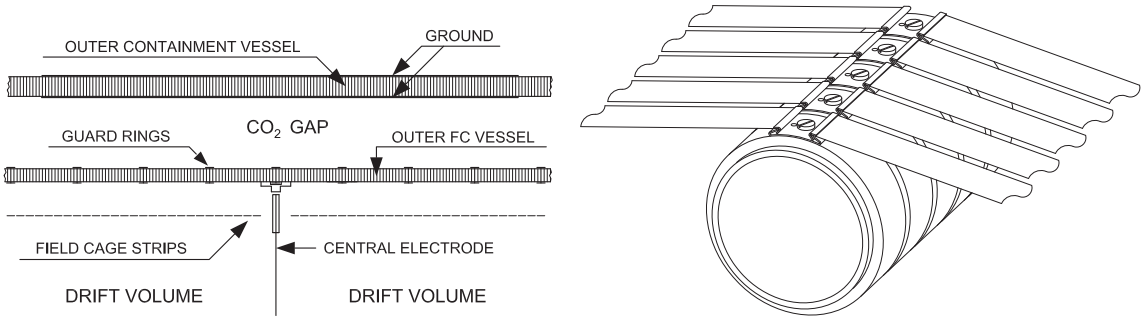

(a) (b)

Figure 3.13: (a) Components of the outer field cage close to the central electrode [54]. (b) Field cage strips attached to the resistor rod [54].

3.5 Field cage

The inner and outer field cages are used to provide a homogeneous electric field within the volume of the TPC to ensure the absence of distortions of the electron drift paths as described in Section 3.3.1 [54]. Figure 3.13a shows the outer field cage close to the central electrode. The field cage consists of field cage strips, a field cage vessel with coarsely spaced guard rings, a CO_2 gap for insulation and a containment vessel.

Field cage strips

Figure 3.13b shows five field cage strips attached to the resistor rod, which contains a chain of resistors to define the potentials of the field cage strips. The field cage strips at the inner and outer field cages consist of 165 mylar strips per side, which are wrapped around 18 rods placed between the sectors. The 13 mm wide strips are separated by a 2 mm gap. As indicated in Figure 3.13a, the first field cage strip next to the central electrode is left out due to mechanical considerations [54]. The potential of the last field cage strip is tuned to match the potential of the top electrode of the readout chambers.

Resistor rod cooling system

The water-based cooling system for the resistor rods, shown in Figure 3.14a, provides stable temperature conditions in the volume of the TPC along the resistor rod to reduce electron drift velocity variations. Highly purified water is circulated through ceramic tubes from the readout chambers toward the central electrode and back. The ceramic tubes are connected to the resistors by copper plates for heat transfer. Each of the four resistor rods has its independent cooling system, which is operated at underpressure to prevent water leakage in the event of a leak in a tube.

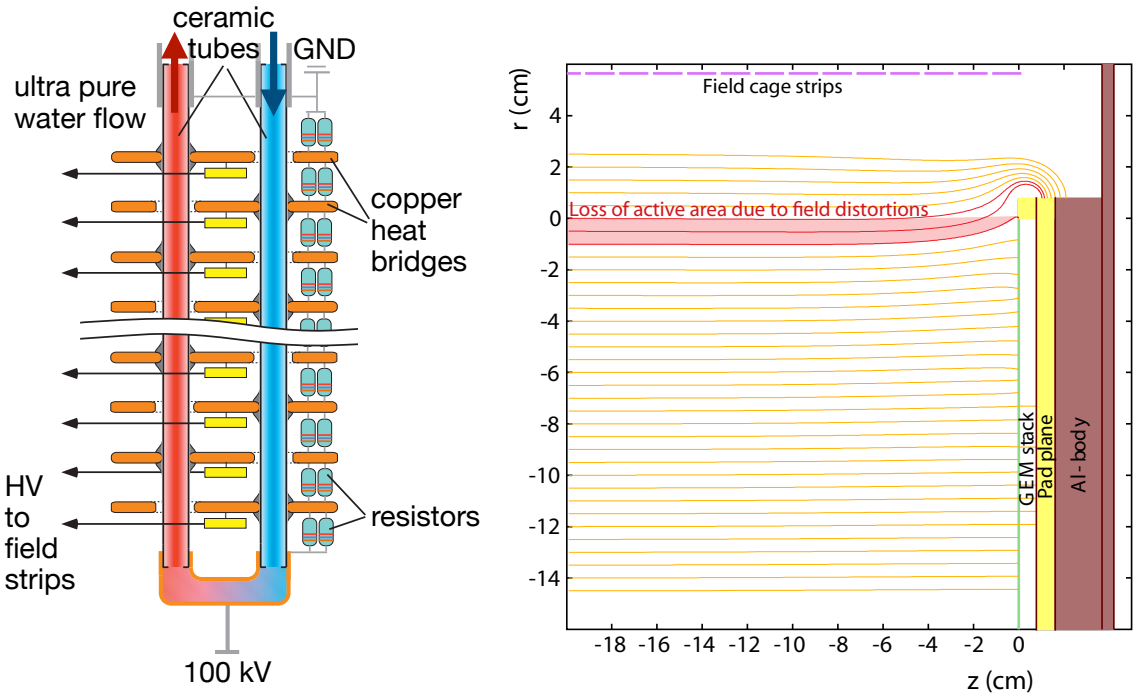

(a) (b)

Figure 3.14: (a) Schematic view of the resistor rod cooling system. Adapted from [54]. (b) Calculated electric field lines close to the readout chambers near the outer field cage without the skirt electrode [8].

Field cage vessels

The inner and outer field cage vessels are gas-tight structures and define the gas volume of the TPC. Coarsely segmented guard rings placed on the vessels reduce charge build-up on the surface of the vessels. An independent resistor chain defines the potential of these guard rings. The potential of the containment vessel is grounded and separated from the field cage vessel by an insulating CO_2 gap.

Removal of the skirt electrode

During Run 1 and Run 2, a skirt electrode was used to cover the gap between the outer field cage strips and the readout chambers to ensure a homogeneous electric field in the region of the gap. However, the skirt electrodes are not suitable for the high voltage at which the top electrode of the GEM 1 is operated, which made it necessary to remove the skirt electrodes for Run 3. Figure 3.14b shows the electric field close to the readout chambers near the outer field cage, calculated without the skirt electrode. The red area illustrates the drift region whose electric field lines no longer end at the readout plane due to the inhomogeneities introduced by the removal of the skirt electrode.

Parameter	Description	Value
$\omega\tau(B = 0.5\,\mathrm{T})$		0.32
N_t	total number of ionization electrons per MIP	36.1 e/cm
v_ion	ion drift velocity	1.168 cm/ms
v_ele	electron drift velocity	2.58 cm/µs
D_L	longitudinal electron diffusion coefficient	209 µm
D_T	transverse electron diffusion coefficient	221 µm

Table 3.1: Gas properties for $\mathrm{Ne}-\mathrm{CO_2}-\mathrm{N_2}$ (90-10-5) at 400 V cm^{-1} [8].

3.6 Choice of the gas mixture

The neon-based gas mixture $\mathrm{Ne}-\mathrm{CO_2}-\mathrm{N_2}$ (90-10-5) used in the TPC has been chosen mainly to reduce the ion drift time and the resulting space-charge distortions by a factor of about two compared to argon-based gas mixtures [29]. In addition, this gas mixture provides low multiple scattering cross-sections and sufficient diffusion properties [54]. The noble gas neon serves as the main component for primary ionization. $\mathrm{CO_2}$ added to the gas mixture acts as a quench gas to absorb photons that are produced during the electron amplification in the readout chambers. The $\mathrm{CO_2}$ concentration has been tuned such that it does not significantly increase the electron drift velocity. A small amount of $\mathrm{N_2}$ is added to the gas composition to further improve the stability and to reduce discharges between GEM foils with negligible effect on the gas properties. In addition, the admixture of $\mathrm{N_2}$ suppresses the amplification of electrons in the transfer fields between GEM foils. A summary of the most relevant properties of the gas mixture is given in Table 3.1.

3.7 Reconstruction

Accurate reconstruction of particle tracks and precise particle identification with the TPC are crucial for understanding high-energy particle collisions in ALICE. Reconstruction of particle tracks, determination of the momentum and particle identification by the specific energy loss are performed in several steps in O^2, which are outlined in the following sections.

3.7.1 Clustering

The first step in the reconstruction is the so-called clustering of the digitized signals. As an example, Figure 3.15a shows the measured digits for a TPC sector for a readout

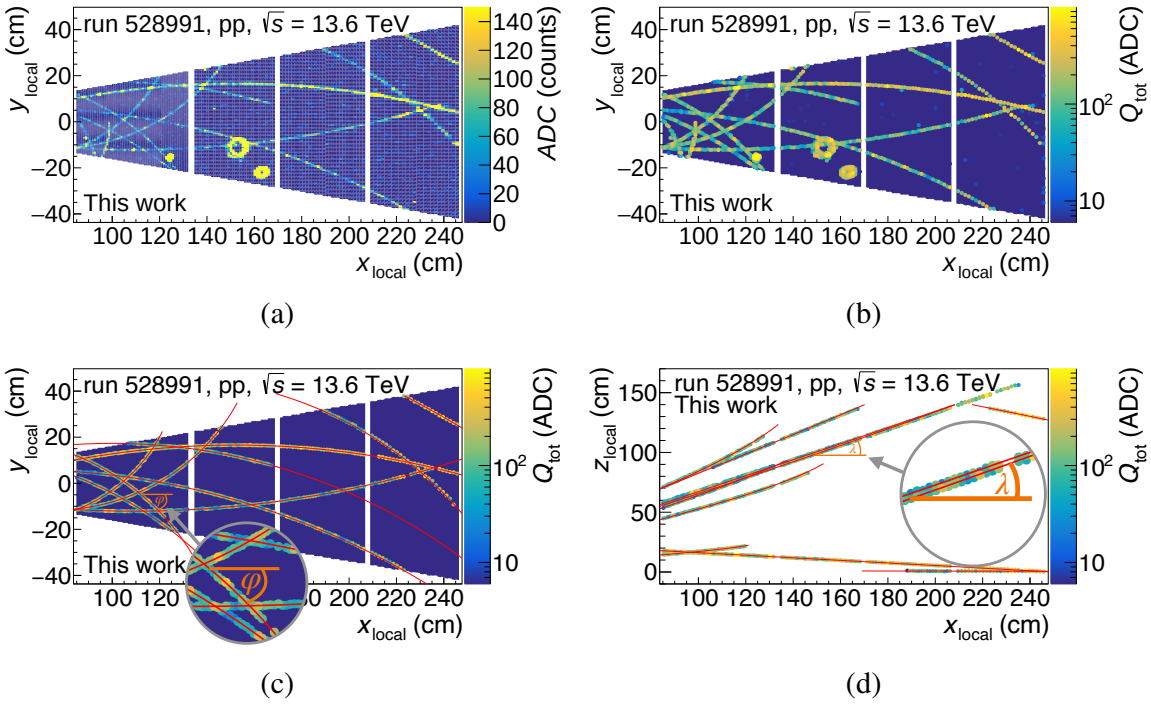

Figure 3.15: (a) Measured digits, (b) reconstructed clusters, (c) and (d) reconstructed tracks and attached clusters to the tracks for pp collisions for 10 ms of readout time in one TPC sector.

time of about 10 ms in pp collisions. A digit contains the information of the digitized charge q, the time information t from the 5 MHz sampling clock, the pad row and the pad number p in the pad row.

Figure 3.15b shows the reconstructed clusters of the digits. During clustering, the digits for each pad row are arranged in a two-dimensional matrix, where the pad and the time information define the dimensions [55]. If a digit in this matrix exceeds a certain threshold and defines a local maximum within a 5×5 submatrix, the n_{digits} digits in the 5×5 submatrix are used to extract the cluster properties summarized in Table 3.2.

3.7.2 Tracking

After clustering, the particle tracks are reconstructed. Figures 3.15c and 3.15d show as red lines the particle trajectories found after the track reconstruction along with their associated clusters. In general, the trajectory of a charged particle passing through the TPC in a magnetic field is deflected by the Lorentz force and can thus be described by a helix with the five track parameters $(y_{\text{local}}, z_{\text{local}}, \sin(\varphi), \tan(\lambda), q/p_{\text{T}})$. These track parameters are summarized in Table 3.3, together with the longitudinal momentum p_{L}

Cluster property	Symbol	Calculation
total cluster charge	Q_{tot}	$\sum_{i=1}^{n_{\mathrm{digits}}} q_i$
maximum cluster charge	Q_{max}	$\max\{q_1, \ldots, q_n\}$
position of the cluster in pad direction	μ_{p}	$1/Q_{\mathrm{tot}} \cdot \sum_{i=1}^{n_{\mathrm{digits}}} q_i \cdot p_i$
width of the cluster in pad direction	σ_{p}^2	$1/Q_{\mathrm{tot}} \cdot \sum_{i=1}^{n_{\mathrm{digits}}} q_i \cdot \left(p_i - \mu_{\mathrm{p}}\right)^2$
position of the cluster in time direction	μ_{t}	$1/Q_{\mathrm{tot}} \cdot \sum_{i=1}^{n_{\mathrm{digits}}} q_i \cdot t_i$
width of the cluster in time direction	σ_{t}^2	$1/Q_{\mathrm{tot}} \cdot \sum_{i=1}^{n_{\mathrm{digits}}} q_i \cdot (t_i - \mu_{\mathrm{t}})^2$

Table 3.2: Typical cluster properties and their definition [55].

and the total momentum p derived after the track reconstruction. The track inclination angle $\sin(\varphi)$ and the track dip angle $\tan(\lambda)$ are shown as examples in Figures 3.15c and 3.15d. The tracking is performed in two stages [56]:

1. Seeding and track following: During seeding, short-track candidates are identified. The track candidates are extrapolated through the TPC sector to find possible clusters that belong to the same track candidate. The track parameters are updated by a simplified Kalman filter as new clusters are attached to the track.

2. Track merging and re-fit: During the track merging, all track segments in a sector that belong to the same track and were not connected during the track following are merged. In addition, track segments from adjacent sectors are merged. Once the track segments are merged, a full re-fit is performed by using a full Kalman filter approach.

3.7.3 Kalman filter

The Kalman filter algorithm [57] provides a fast and robust approach to track reconstruction by accounting for uncertainties in cluster properties, particle deflection due to multiple scattering and energy loss of the particle along its trajectory.
The track reconstruction starts with a track seed, serving as a rough estimate of the track parameters summarized in Table 3.3. A cluster from the adjacent pad row is then found and attached to the track by extrapolating the track parameters to the next pad row, taking into account cluster errors and multiple scattering processes as uncertainties. The track parameters are updated with the newly attached cluster. This procedure is repeated until the last pad row is reached or until no clusters are found in several adjacent pad rows.

Track parameter	Description
1: y_{local}	local y-position of the track
2: z_{local}	z-position of the track
3: $\sin(\varphi)$	track inclination angle in the x_{local}-y_{local} plane relative to the x_{local} axis
4: $\tan(\lambda)$	track dip angle in the x_{local}-z_{local} plane relative to the x_{local} axis
5: q/p_{T}	charge of the particle over transverse momentum of the particle
p_{L}	longitudinal momentum: $\lvert p_{\text{T}}/q \rvert \cdot \tan(\lambda)$
p	total momentum: $\lvert p_{\text{T}}/q \rvert \cdot \sqrt{1 + \tan^2(\lambda)}$

Table 3.3: Track parameters used to describe the trajectory of a charged particle in the TPC.

3.7.4 Data-driven approach for space-point distortion correction

During the tracking, the space-point distortions of the reconstructed clusters due to inhomogeneities in the electric and magnetic field components, as described in Section 3.3.1, must be corrected to avoid biases in the track parameters. These biases in momentum and position resolution would deteriorate the overall data quality to such an extent that precise physics analyses would not be feasible without dedicated space-point distortion correction procedures.
During Run 1 and Run 2, a data-driven approach was developed and used to create precise three-dimensional correction maps. This data-driven approach was ported [58] to O^2 and is actively used as a fundamental part of the space-point distortion correction procedure. Figure 3.16 shows a schematic representation of this data-driven approach, which is performed in the following steps:

1. During the TPC tracking, relaxed tolerances are used in the cluster to track association. The distorted TPC clusters are shown as blue dots. The obtained track is shown as a dashed blue line.

2. The TPC tracks are matched with the ITS tracks and optionally with potential TRD and TOF track segments which are not affected by drift-field distortions. The measurements in the ITS, the TRD and TOF are shown as red dots.

3. The matched ITS tracks with the TRD and TOF track segments yield the reference tracks that are extrapolated to the same x_{local}-positions, indicated by small green dots, as the distorted TPC clusters. The extrapolated reference track is shown as a red line.

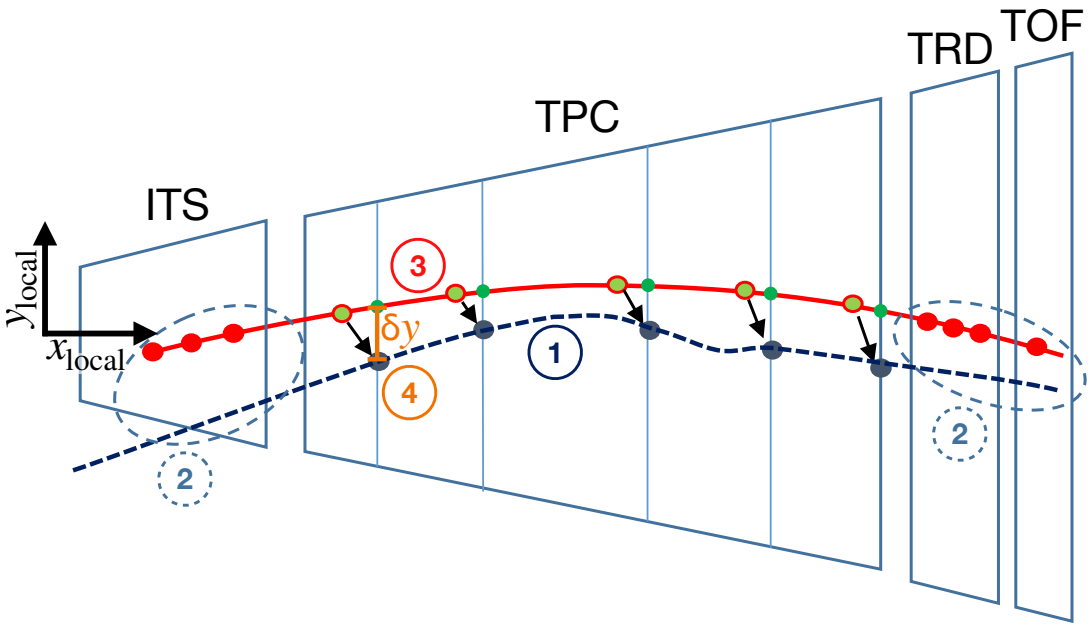

Figure 3.16: Illustration of the data-driven approach for extracting three-dimensional correction maps for the space-point distortions. Adapted from [58].

4. The residuals in y_{local}-direction between the TPC clusters and the extrapolated reference track, denoted by δy, are stored with the local angle φ of the reference track in a three-dimensional map. This δy residual is shown as an orange line for one cluster. Similarly, a three-dimensional map for the track-to-cluster residuals in the z-direction is created with the track angle λ, delivering the δz residuals.

5. Robust linear parameterizations of the measured track-to-cluster residuals are performed in each voxel of the three-dimensional map to extract the Δx, Δy and Δz corrections for the distorted TPC clusters. Figure 3.17a shows the relationship $\delta y = \Delta y - \Delta x \tan(\varphi)$ between the measured δy residuals and the corrections Δx and Δy indicated as blue arrows. An example of a robust linear parameterization for one voxel in the three-dimensional map is shown in Figure 3.17b. The parameters from the linear parameterizations yield directly the corrections Δx, Δy and Δz for each voxel.

6. For each pad row in each TPC sector, an individual smooth parameterization of the extracted corrections in the y_{local}-z plane is performed by smooth splines. These splines are stored in the CCDB and are automatically loaded during the track reconstruction to correct the distorted TPC cluster positions.

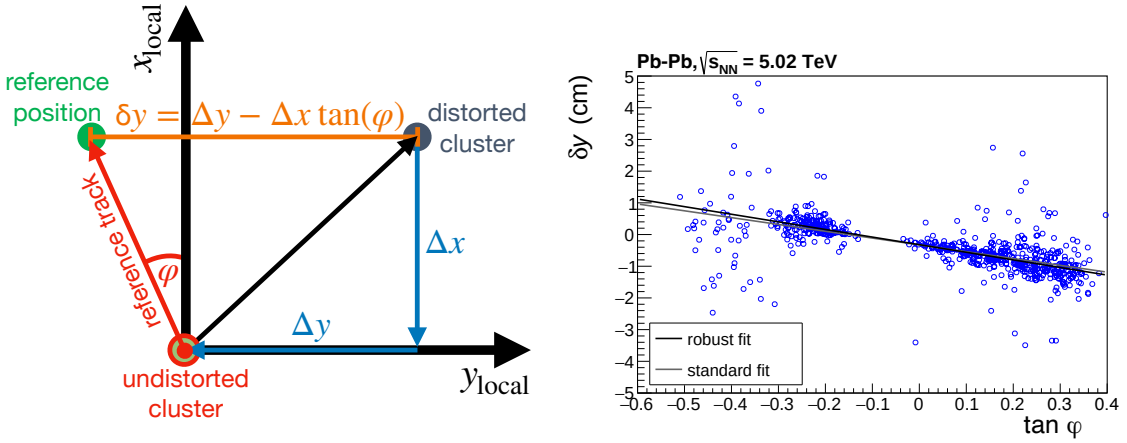

(a) (b)

Figure 3.17: (a) Relationship between the measured δy residual and the angle φ of the reference track to the corrections Δx and Δy. (b) Example of the measured δy residuals as a function of the reference track angle $\tan(\varphi)$. Adapted from [58].

3.7.5 Particle identification

Particle identification is performed after the tracking by combining the momentum with the reconstructed specific energy loss.

Figure 3.18 shows the reconstructed specific energy loss as a function of the momentum over the absolute charge of the particle. The black lines show the expected energy loss for various particle species from a parameterization of the Bethe-Bloch equation. For each track, the specific energy loss $\mathrm{d}E/\mathrm{d}x_{(\text{tot,max})}$ is calculated by the truncated mean of the distribution of the cluster charges Q_{tot} and Q_{max}. The truncated mean is used as a robust estimator of the most probable energy loss to avoid biases due to the tails in the energy loss probability distribution as described in Section 3.1. The truncated mean is defined with the number of clusters associated to a track, n_{cl}, as:

$$\mathrm{d}E/\mathrm{d}x_{(\text{tot,max})} = \frac{1}{0.6 \cdot n_{\text{cl}} - 0.015 \cdot n_{\text{cl}}} \sum_{i=0.015 \cdot n_{\text{cl}}}^{0.6 \cdot n_{\text{cl}}} Q_{(\text{tot,max}),i} \ . \tag{3.20}$$

During Run 1, detailed studies were carried out to determine the optimal lower and upper truncation ranges, which were found to be 1.5% and 60%, respectively [59]. The algorithms for calculating the specific energy loss are performed on GPUs directly during the online reconstruction of the data to provide possibilities for online QA of the particle identification performance.

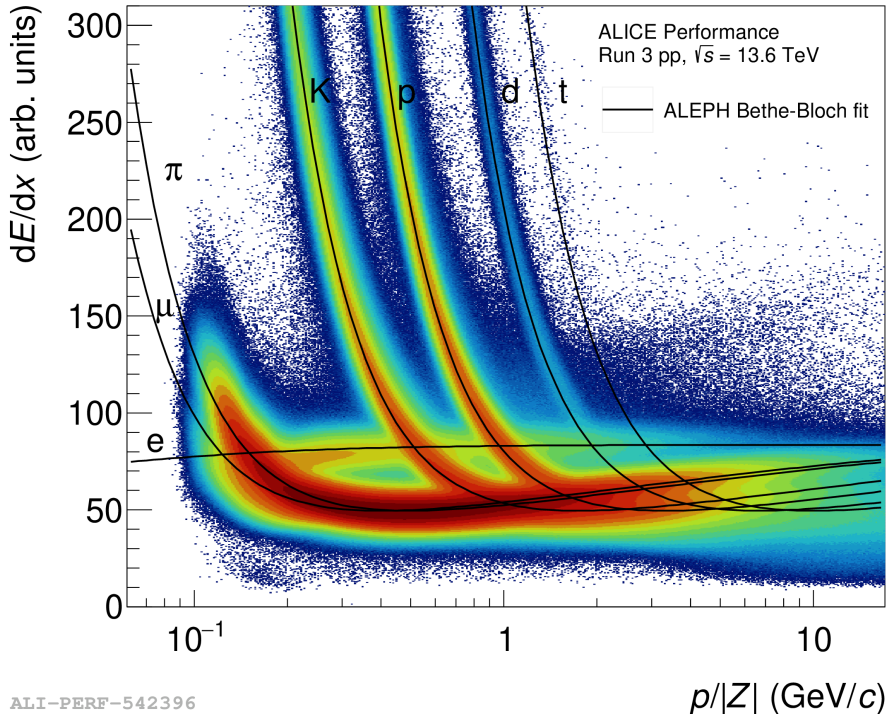

Figure 3.18: Reconstructed specific energy loss as a function of the momentum over absolute charge with the expectations from a parameterization of a Bethe-Bloch function [60].

To get an estimate of the quality of the reconstructed specific energy loss, the relative resolution and the separation power are usually used as measures for the particle identification performance. The relative resolution $\sigma_{\text{rel.},(\text{tot,max}),i}$ for a given momentum of the particle species i can be determined from the width $\sigma_{\mathrm{d}E/\mathrm{d}x_{(\text{tot,max})},i}$ of the reconstructed specific energy loss:

$$\sigma_{\text{rel.},(\text{tot,max}),i}(p) = \frac{\sigma_{\mathrm{d}E/\mathrm{d}x_{(\text{tot,max})},i}(p)}{\langle \mathrm{d}E/\mathrm{d}x_{(\text{tot,max})} \rangle_i(p)} \ . \tag{3.21}$$

Similarly, the separation power $S_{(\text{tot,max}),i,j}$ of two particle species i and j is defined as:

$$S_{(\text{tot,max}),i,j}(p) = \frac{\left| \langle \mathrm{d}E/\mathrm{d}x_{(\text{tot,max})} \rangle_i(p) - \langle \mathrm{d}E/\mathrm{d}x_{(\text{tot,max})} \rangle_j(p) \right|}{0.5 \left(\sigma_{\mathrm{d}E/\mathrm{d}x_{(\text{tot,max})},i}(p) + \sigma_{\mathrm{d}E/\mathrm{d}x_{(\text{tot,max})},j}(p) \right)} \ . \tag{3.22}$$

To achieve the desired separation power of about five to six [8], several corrections for the cluster charges Q_{max} and Q_{tot} are necessary. The most relevant corrections are described in the following section.

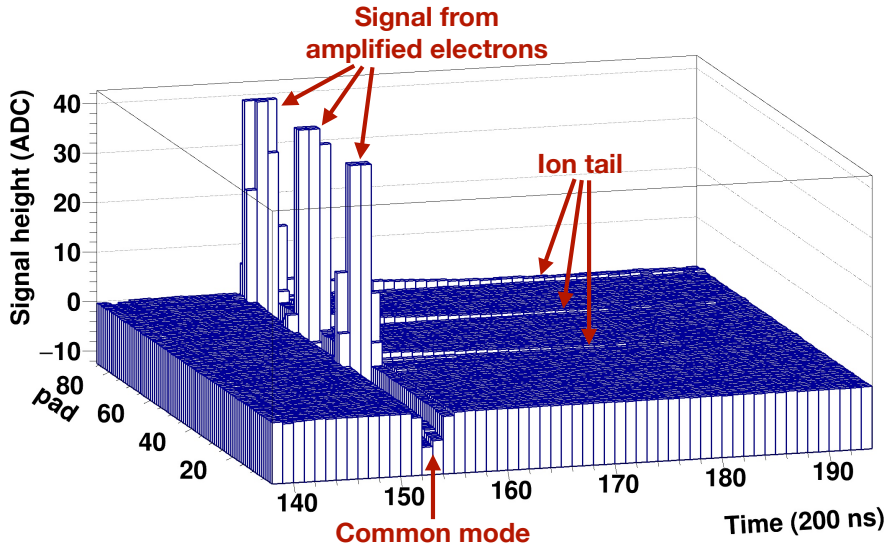

Figure 3.19: Laser signal and resulting common-mode and ion tail signal for a pad row as a function of time. The axis of the signal height is truncated at 40 ADC counts for better visualization. Adapted from [61].

3.7.6 Calibration of the specific energy loss

The following corrections are applied to optimize the relative resolution and separation power of the reconstructed specific energy loss:

1. Common-mode and ion tail correction [61, 62]: Figure 3.19 shows the induced signals on the pads due to the common-mode and ion tail effect for a pad row as a function of time and the pad number. The signals of the amplified electrons from three laser tracks are also shown. Both effects are corrected on the CRU before zero suppression.

    a) Ion tail effect: Positively charged ions produced during the electron amplification drift away from the readout plane and thus induce signals of negative polarity on the readout pads. Due to the slow drift velocity of the ions compared to the electrons, the induced signals from the ions are visible as a long tail after the fast signals from the electrons.

    b) Common-mode effect: Electrons drifting from GEM 4 to the readout plane induce a current on GEM 4, leading to a fast voltage drop across the GEM 4 foil. Due to this fast voltage drop, a signal of positive polarity is induced on all pads of the GEM stack, which is roughly suppressed by the area of the GEM stack. To correct for this effect and other possible couplings, a mean baseline correction is performed [63].

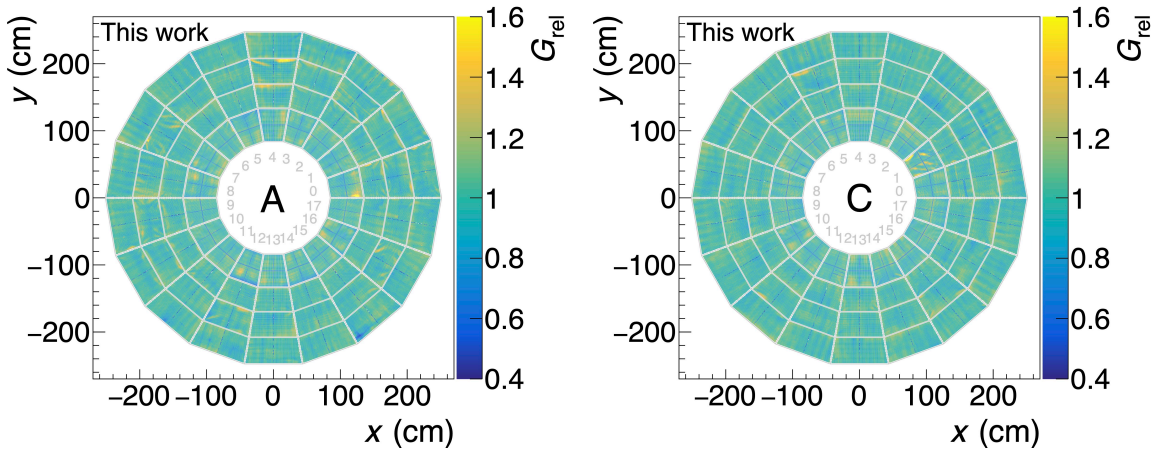

(a) (b)

Figure 3.20: Relative gain G_{rel} for the (a) A-side and the (b) C-side from the krypton calibration method as stored in the CCDB.

2. Krypton pad-by-pad gain calibration: As described in Section 3.4.3, local pad-by-pad gain variations are expected. Figures 3.20a and 3.20b show relative pad-by-pad gain maps created by the krypton calibration method for the A-side and the C-side, respectively. Releasing radioactive krypton into the TPC and measuring the decay spectrum in each pad is a commonly used technique to obtain accurate pad-by-pad gain maps. For each pad, the main peak of the decay spectrum is parameterized by a Gaussian function to extract the mean position of the peak. The pad-by-pad gain map is created by normalizing the extracted peak positions to unity. A detailed description of the extraction procedure can be found in [53].

3. Readout geometry, track topology, electron attachment, diffusion and zero suppression: The cluster charges Q_{tot} and Q_{max} depend on several properties such as the pad size and the local track topology. In addition, electron attachment and diffusion affect the cluster charges dependent on the drift distance of the electrons. Furthermore, the applied zero suppression can affect the total cluster charge if the measured signals on the pads are below this threshold. A detailed description of these dependencies and the applied correction is given in Section 5.1.

4. Time-dependent gain variations: As described in Section 3.4.1, pressure and temperature variations during the operation of the TPC result in gain variations that need to be taken into account. Additionally, variations in the gas mixture can affect the electron attachment, which influences the number of electrons reaching the readout chambers and, thus, influences the reconstructed cluster charges.

An iterative process is used to correct for these dependencies: In the first iteration, the mean of the reconstructed specific energy loss is monitored during the online reconstruction as a function of time in each sector for MIPs. The second iteration takes place later in an offline reconstruction, where the specific energy loss is recalculated by correcting the cluster charges with the extracted mean values from the first iteration to normalize the energy loss for MIPs to a fixed value of 50.

5. Residual pad-by-pad gain variations: To monitor the stability of the extracted krypton pad-by-pad gain map and the other calibrations over time and to correct for possible residual gain variations, particle tracks are used to extract residual pad-by-pad gain maps. A detailed description of the extraction procedure is given in Section 5.2.

4 Drift-field distortions

For Run 3, understanding, measuring and correcting drift-field distortions, which result in distortions of the measured space-points in the TPC, pose one of the most important and challenging tasks to achieve precise tracking. The combination of continuous readout and high interaction rates of up to 50 kHz for Pb–Pb collisions leads to space-point distortions of up to about 10 cm in the radial direction due to space-charge accumulation in the drift volume of the TPC [29]. In addition, the LHC beam behavior and space-charge density fluctuations on short timescales of about 10 ms have to be taken into account in the correction procedures. Time-dependent charging-up effects of detector components and imperfections in the magnetic field lead to additional significant space-point distortions. The development, implementation and maintenance of dedicated correction procedures for the space-point distortions is an ongoing effort by a team of TPC experts and represents the main part of this thesis.

The positively charged ions that are accumulating in the drift volume of the TPC due to the IBF, as described in Section 3.4.1, are treated as a position- and time-dependent space-charge density ρ generating the potential Φ. For simplicity, the time dependency of the space-charge density is neglected in the following. This potential is expressed with the permittivity $\varepsilon \approx \varepsilon_0$ according to Poisson's equation:

$$\Delta\Phi\left(r, \varphi, z\right) = -\frac{\rho\left(r, \varphi, z\right)}{\varepsilon_0}\,. \tag{4.1}$$

The electric field components are given by the gradient of the potential:

$$E_{\mathrm{r}}\left(r, \varphi, z\right) = -\frac{\partial\Phi\left(r, \varphi, z\right)}{\partial r}\,, \tag{4.2a}$$

$$E_{\varphi}\left(r, \varphi, z\right) = -\frac{\partial\Phi\left(r, \varphi, z\right)}{\partial \varphi}\,, \tag{4.2b}$$

$$E_{\mathrm{z}}\left(r, \varphi, z\right) = -\frac{\partial\Phi\left(r, \varphi, z\right)}{\partial z}\,. \tag{4.2c}$$

These electric field components and the magnetic field components of the L3 solenoid result in space-point distortions according to Equations 3.11a–3.11c.

In the following sections, analytical models of relevant sources of drift-field distortions, developed within the scope of this work, are presented and compared with the observed space-point distortions in real data. Additionally, the developed correction procedures for the space-point distortions, implemented in O^2 as part of this work, are described.

4.1 Simulation framework

Simulations of the expected space-point distortions and their comparison with real data provide useful insight into the mechanisms producing these distortions. In addition, simulations are a fundamental part of the development process of the space-point distortion correction procedures. The presented analytical models of the space-point distortions also serve as verification and as an alternative or extension to the purely data-driven approach described in Section 3.7.4 for correcting space-point distortions. Realistic simulations of the space-point distortions require accurate and fast algorithms to solve Equation 4.1 and the integrals in Equations 3.11a–3.11c. To meet these requirements, the old software framework [64] implemented in AliRoot [65] and used in Run 1 and Run 2 for calculating space-point distortions is rewritten within the scope of this work and is implemented into O^2 [66]. The numerical solution of Equation 4.1, using a relaxation multigrid method which is implemented in the old software framework [67], is ported to O^2. The calculations are performed on a three-dimensional grid consisting of the user-defined number of vertices in each dimension: $N_z \times N_r \times N_\varphi$. The electric field components, according to Equations 4.2a–4.2c, are obtained by the numerical gradient of the potential on the user-defined grid.

Figure 4.1 illustrates a slow algorithm for calculating the space-point distortions as an example for one vertex in the r-z plane and it illustrates the algorithm for calculating the corrections for several vertices. The space-point distortions $\delta_{(z,r,\varphi),\mathrm{dist}}$ are defined for each vertex on the grid as the difference between the measured distorted position P_M in the readout chambers to the origin P_0 of the electron at the given vertex:

$$P_M(z, r, \varphi) = P_0(z_V, r_V, \varphi_V) + \delta_{(z,r,\varphi),\mathrm{dist}}(z_V, r_V, \varphi_V)\,. \tag{4.3}$$

The positions (z_V, r_V, φ_V) denote the coordinates of the vertices on the grid. To calculate the space-point distortions, the electric field components are integrated along the drift path of an electron according to Equations 3.11a–3.11c using an iterative procedure: In the first iteration, a user-defined step size along the z-direction denoted as ε_z is used to obtain the electric field components at the position of the vertex $\vec{E}(z_0, r_0, \varphi_0)$, at $\vec{E}(z_0 + \varepsilon_z, r_0, \varphi_0)$ and at $\vec{E}(z_0 + \varepsilon_z/2, r_0, \varphi_0)$. To get the electric field components and all other quantities defined on the grid at arbitrary positions, tricubic interpolation [68] is used. The integrals in Equations 3.11a–3.11c are solved for the step size ε_z with the

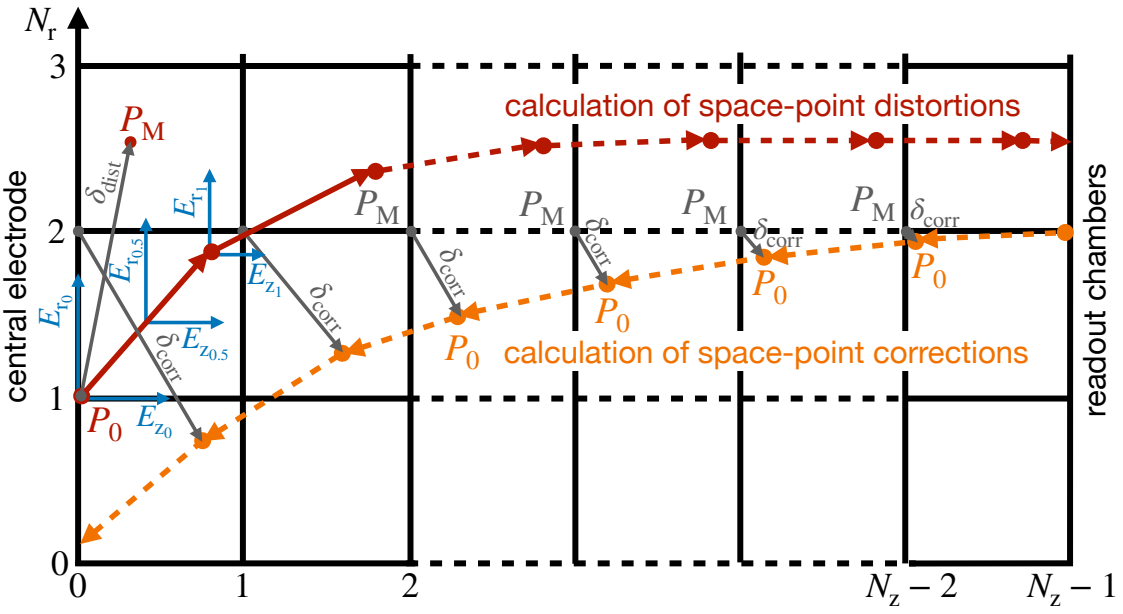

Figure 4.1: Illustration of the slow algorithm for calculating space-point distortions and corrections. The red arrows indicate the electron's drift path for one vertex. The orange arrows show the approach used to calculate the corrections for the space-point distortions.

interpolated electric field components by using Simpson's rule [69]:

$$\begin{aligned}\int_{a=z_0}^{b=z_0+\varepsilon_z} f(x)\mathrm{d}x &\approx \frac{b-a}{6}\left[f(a)+4f\left(\frac{a+b}{2}\right)+f(b)\right] \\ &= \frac{\varepsilon_z}{6}\left[f(z_0,r_0,\varphi_0)+4f(z_0+\varepsilon_z/2,r_0,\varphi_0)+f(z_0+\varepsilon_z,r_0,\varphi_0)\right].\end{aligned} \tag{4.4}$$

In the second iteration, the local space-point distortions from the first iteration are taken into account by solving the integrals in Equations 3.11a–3.11c along the distorted electron drift path, i.e. at:

$$E_{z_0,r_0,\varphi_0} = \vec{E}(z_0, r_0, \varphi_0)\,, \tag{4.5a}$$

$$E_{z_{0.5},r_{0.5},\varphi_{0.5}} = \vec{E}(z_0 + (\varepsilon_z + \delta_z)/2, r_0 + \delta_r/2, \varphi_0 + \delta_\varphi/2)\,, \tag{4.5b}$$

$$E_{z_1,r_1,\varphi_1} = \vec{E}(z_0 + \varepsilon_z + \delta_z, r_0 + \delta_r, \varphi_0 + \delta_\varphi)\,, \tag{4.5c}$$

as shown in Figure 4.1 by the first red arrow starting at P_0. The iterative procedure to calculate the local space-point distortions is repeated until the electron drift path, indicated by the red arrows, ends at the readout plane. The space-point distortions, indicated by a gray arrow at the starting position of the electron, are obtained by

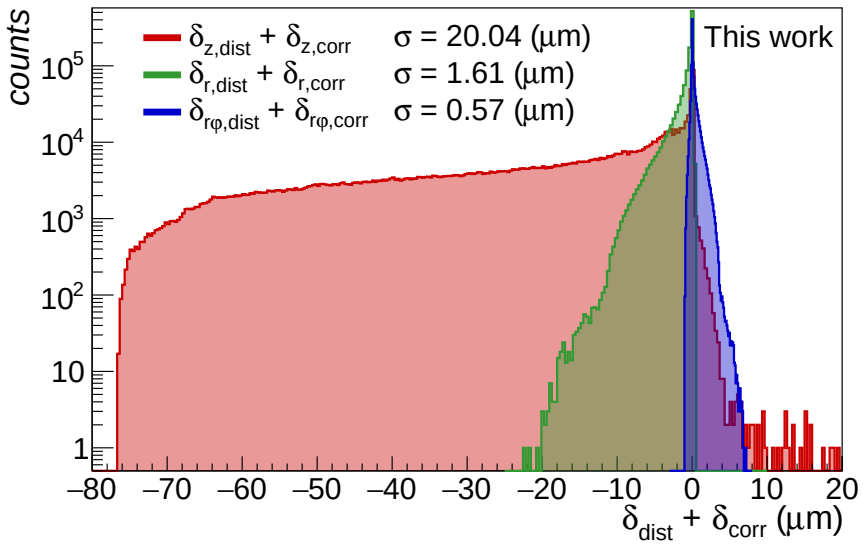

Figure 4.2: Deviations between the calculated space-point distortions and corrections for a grid granularity of $N_z \times N_r \times N_\varphi = 513 \times 129 \times 360$.

summing up all local space-point distortions and they are stored at the vertex of the starting position of the drift electron.

The corrections $\delta_{(z,r,\varphi),corr}$ are defined for the electrons that are measured at the positions of the vertices on the grid, where the drift time of the electron is defined by the z-position of the vertex:

$$P_0(z, r, \varphi) = P_M(z_V, r_V, \varphi_V) + \delta_{(z,r,\varphi),corr}(z_V, r_V, \varphi_V) \,. \tag{4.6}$$

The algorithm used to calculate the corrections is similar to the one that is used for the calculation of the space-point distortions. For the corrections, the drift path of an electron is traced back from the readout chambers to the central electrode, as shown by the orange dotted arrows in Figure 4.1. In contrast to the space-point distortions, tracing the electron drift path backward allows the calculation and storage of the corrections for all z-vertices for a given r-vertex and φ-vertex, as indicated by the gray arrows.

Figure 4.2 shows, for a grid granularity of $N_z \times N_r \times N_\varphi = 513 \times 129 \times 360$, a crosscheck between the calculated space-point distortions and the corresponding corrections, which should ideally cancel each other out. The simulation of the space-charge density used as input for these calculations is described in Section 4.1.1. The maximum deviation between the space-point distortions and the corrections is about 80 µm for the space-point distortions in the z-direction. For the space-point distortions in radial and $r\varphi$-directions, the deviations are well below 20 µm. The standard deviations, as indicated in the figure,

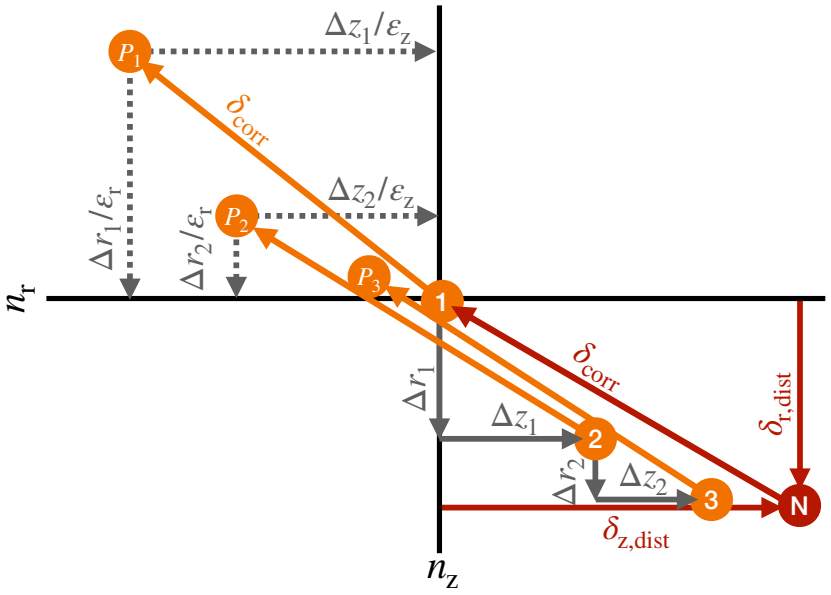

Figure 4.3: Fast iterative procedure to calculate the space-point distortions by interpolating the corrections.

are all well below the intrinsic resolution of the TPC of about 200 µm [70], confirming sufficient precision for the implemented algorithms. To further reduce the deviations between the space-point distortions and the corrections, a finer grid can be used.

The previously described procedure requires calculating the space-point distortions for each vertex on the grid individually, which becomes computationally expensive, especially when a fine grid is used. The computational cost for calculating the corrections is orders of magnitude smaller than for the space-point distortions, since, for the corrections, the electron drift paths are computed only for the last vertices at $N_z - 1$.

Figure 4.3 illustrates for one arbitrary vertex the new, fast and self-consistent iterative algorithm implemented in O^2 to speed up the calculation of the space-point distortions: After calculating the corrections on the grid, tricubic interpolation of the corrections is used to, for each vertex, iteratively approach the position where the interpolated corrections point to the vertex. In the first iteration, the corrections are queried at the position of the vertex of interest, for which the space-point distortions are calculated to obtain the corrected position P_1:

$$P_1(z_1, r_1, \varphi_1) = P_M(z_V, r_V, \varphi_V) + \delta_{(z,r,\varphi),corr}(z_V, r_V, \varphi_V)\,. \tag{4.7}$$

The correction vector is indicated by an orange arrow and the iteration by its number. In the second and subsequent iterations, the corrections are queried at a slightly different

position than in the previous iteration, defined by the step size $\varepsilon_{(\mathrm{z,r,\varphi})}$, chosen as 0.5 in Figure 4.3, and the corrected position from the previous iteration. The procedure is repeated until the difference between the position of the vertex of interest to the resulting corrected position is smaller than 1 µm or when a maximum of 100 iterations has been reached. The algorithm can be expressed with

$$\Delta(z_k, r_k, \varphi_k) = (\varepsilon_{\mathrm{z}}(z_{\mathrm{V}} - z_k), \varepsilon_{\mathrm{r}}(r_{\mathrm{V}} - r_k), \varepsilon_{\varphi}(\varphi_{\mathrm{V}} - \varphi_k)) \,, \tag{4.8}$$

where k denotes the iteration:

$$\begin{aligned} P_2(z_2, r_2, \varphi_2) &= P_{\mathrm{M}}(z_{\mathrm{V}} + \Delta z_1, r_{\mathrm{V}} + \Delta r_1, \varphi_{\mathrm{V}} + \Delta\varphi_1) \\ &\quad + \delta_{(\mathrm{z,r,\varphi}),\mathrm{corr}}(z_{\mathrm{V}} + \Delta z_1, r_{\mathrm{V}} + \Delta r_1, \varphi_{\mathrm{V}} + \Delta\varphi_1) \end{aligned} \tag{4.9}$$

$$P_2(z_2, r_2, \varphi_2) = P_{\mathrm{M}}(z_{2'}, r_{2'}, \varphi_{2'}) + \delta_{(\mathrm{z,r,\varphi}),\mathrm{corr}}(z_{2'}, r_{2'}, \varphi_{2'}) \,, \tag{4.10}$$

$$\begin{aligned} P_3(z_3, r_3, \varphi_3) &= P_{\mathrm{M}}(z_{2'} + \Delta z_2, r_{2'} + \Delta r_2, \varphi_{2'} + \Delta\varphi_2) \\ &\quad + \delta_{(\mathrm{z,r,\varphi}),\mathrm{corr}}(z_{2'} + \Delta z_2, r_{2'} + \Delta r_2, \varphi_{2'} + \Delta\varphi_2) \,, \end{aligned} \tag{4.11}$$

$$\vdots$$

$$P_{\mathrm{V}}(z_{\mathrm{V}}, r_{\mathrm{V}}, \varphi_{\mathrm{V}}) \approx P_{\mathrm{N}}(z_{\mathrm{N}}, r_{\mathrm{N}}, \varphi_{\mathrm{N}}) = P_{\mathrm{M}}(z_{\mathrm{N}'}, r_{\mathrm{N}'}, \varphi_{\mathrm{N}'}) + \delta_{(\mathrm{z,r,\varphi}),\mathrm{corr}}(z_{\mathrm{N}'}, r_{\mathrm{N}'}, \varphi_{\mathrm{N}'}) \,. \tag{4.12}$$

The signs of the interpolated corrections from the last iteration, indicated by a red arrow, are inverted and stored at the vertex of interest as the space-point distortions. Figure 4.4 shows the real-time for calculating the space-point distortions and corrections from a given space-charge density as input for different grid sizes. The performance of the old software framework in AliRoot is shown in blue, the performance of the new software framework in O^2 when using the slow algorithm illustrated in Figure 4.1 is shown in green and the performance when using the fast algorithm illustrated in Figure 4.3 is shown in red. The empty markers for the algorithms in O^2 indicate the performance when using one CPU thread, while the filled markers indicate the performance when using thirty CPU threads. The slow and fast algorithms to calculate the space-point distortions and corrections in O^2 feature modern C++, multi-threading and vectorization, resulting in a performance increase of up to two orders of magnitude compared to the old algorithms in AliRoot.

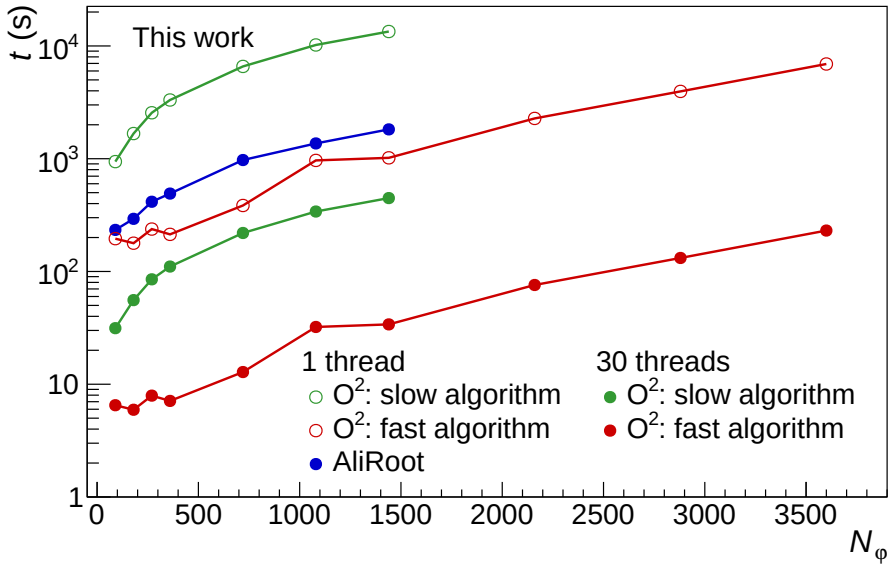

Figure 4.4: Real-time for calculating the space-point distortions as a function of the number of N_φ-vertices for the old framework in AliRoot and the new framework in O^2.

4.1.1 Space-charge density and distortions

For the simulation of the expected space-charge density and the resulting space-charge distortions for an interaction rate of 50 kHz, over 30 000 Pb–Pb collisions are generated with O^2. The number of particle collisions contributing to the accumulation of ions in the volume of the TPC is referred to as ion pileup events $N^{\text{ion}}_{\text{pileup}}$ in the following. The mean number of ion pileup events depends on the interaction rate IR and the time $t_{\text{d,ion}}$ it takes the ions to drift from the readout chambers to the central electrode. The statistical fluctuations in the number of ion pileup events follow a Poisson probability distribution. Using the ion drift time from Equation 3.18 and assuming an interaction rate of 50 kHz gives:

$$\left\langle N^{\text{ion}}_{\text{pileup}} \right\rangle = t_{\text{d,ion}} \cdot \text{IR} = 192.30\,\text{ms} \cdot 50\,\text{kHz} = 9615\,. \tag{4.13}$$

However, for simplicity, the mean number of ion pileup events is chosen as 10 000 for the space-charge density simulations for 50 kHz Pb–Pb collisions.

Figure 4.5a shows the simulated space-charge density as an example for one moment in time for 50 kHz Pb–Pb collisions as a function of the radius and the z-position in the TPC. The disks with high space-charge density correspond to Pb–Pb collisions with rather large multiplicities, where correspondingly a large number of ions is produced.

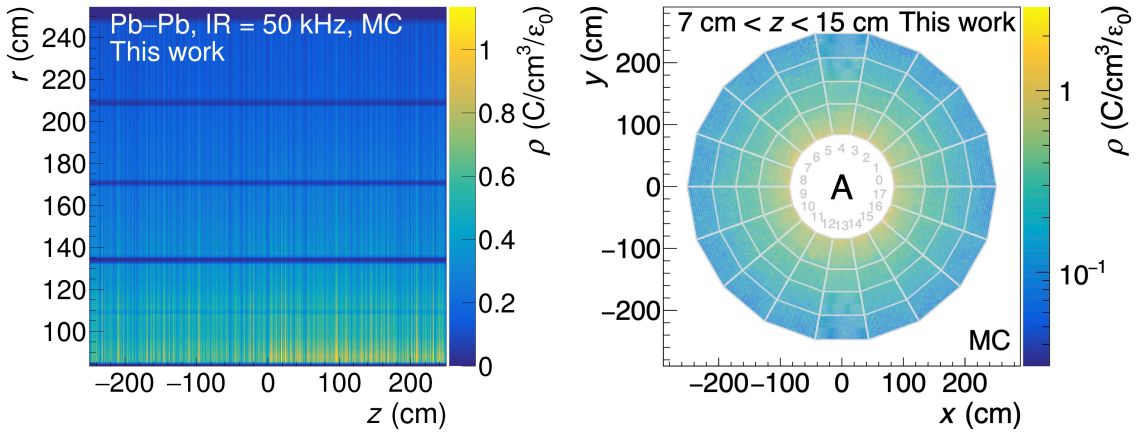

(a) (b)

Figure 4.5: Simulated space-charge density for one moment in time for 50 kHz Pb–Pb collisions in the (a) r-z plane and the (b) x-y plane for the A-side.

These space-charge density fluctuations are described in detail in Section 4.1.2 and their implications on the space-charge distortions in Section 4.1.3. The slightly lower space-charge density on the C-side compared to the A-side is caused by the muon absorber which blocks a small fraction of particles. Figure 4.5b shows one space-charge density disk for the A-side in the x-y plane. The radial decrease in the space-charge density is caused by the decreasing track density with increasing radius and low-momentum tracks not reaching the outer radii of the TPC. The simulation of the space-charge density maps is carried out in the following steps:

1. The number of ion pileup events $N^{\text{ion}}_{\text{pileup}}$ is drawn randomly from a Poisson distribution with a mean of 10 000.

2. $N^{\text{ion}}_{\text{pileup}}$ events are randomly drawn from the pool of 30 000 collisions.

3. For each drawn event, a random rotation of the hits is performed in the azimuthal angle φ, with the same rotation applied to all hits within an event. The hits describe the position where an ionization process occurs.

4. The propagation of the electrons from the ionization processes through the TPC gas volume to the readout chambers is performed by taking diffusion and attachment into account. The amplification of the electrons is based on the implementation in O^2 and is described in detail in [71]. Pad-by-pad gain variations during the amplification of the electrons are taken into account by using the krypton gain map described in Section 3.7.6.

5. The number of ions from the amplification stage drifting into the volume of the TPC is obtained by multiplying the number of electrons after amplification by the IBF extracted from the production QA data as described in Section 3.4.3.

6. For each event, a random ion drift length, i.e. a random z-position, is drawn. For simplicity in the simulations, the ions are propagated to the z-position along straight drift paths. The propagated positions of the ions from IBF and primary ionization are stored in a three-dimensional map. This map contains the number of ions for each given volume element within the TPC.

7. After propagating the ions from all drawn events, the number of ions in each element of the three-dimensional map is converted to the charge per volume element to obtain the space-charge density.

These three-dimensional space-charge density maps are used as input in the space-point distortion framework to calculate the resulting potential, the electric field components and the space-charge distortions for a given magnetic field as described in Section 4.1. Figure 4.6a shows the resulting space-charge distortions of the space-charge density shown in Figure 4.5a in the radial direction in the x-y plane for the A-side, with a magnetic field of 0.5 T and an electron drift distance of 240 cm. Figure 4.6b shows the corresponding space-charge distortions as a function of the radius and the z-coordinate. The radial space-charge distortions become the largest at inner radii, where they reach up to 10 cm. At outer radii, the radial space-charge distortions only reach up to -4 cm. The closer the drift electron is created to the readout chambers, the smaller the radial space-charge distortion. Due to these large radial space-charge distortions, drift electrons do not reach the first and last pad rows for long drift distances, effectively reducing the track lengths.
The space-charge distortions in the $r\varphi$-direction, shown in Figures 4.6c and 4.6d, reach nearly up to 4 cm at inner radii. The asymmetric pattern in the φ-direction within the sectors is created by the magnetic field, which breaks the symmetry. Similar to the radial space-charge distortions, the space-charge distortions in the $r\varphi$-direction are reduced at smaller radii.
The space-charge distortions in the z-direction, shown in Figures 4.6e and 4.6f, become the largest for drift electrons close to the center of a TPC side, reaching about 1.6 cm. The change in the sign between the A-side and C-side is caused by the definition of the z-coordinate, which becomes negative for the C-side.

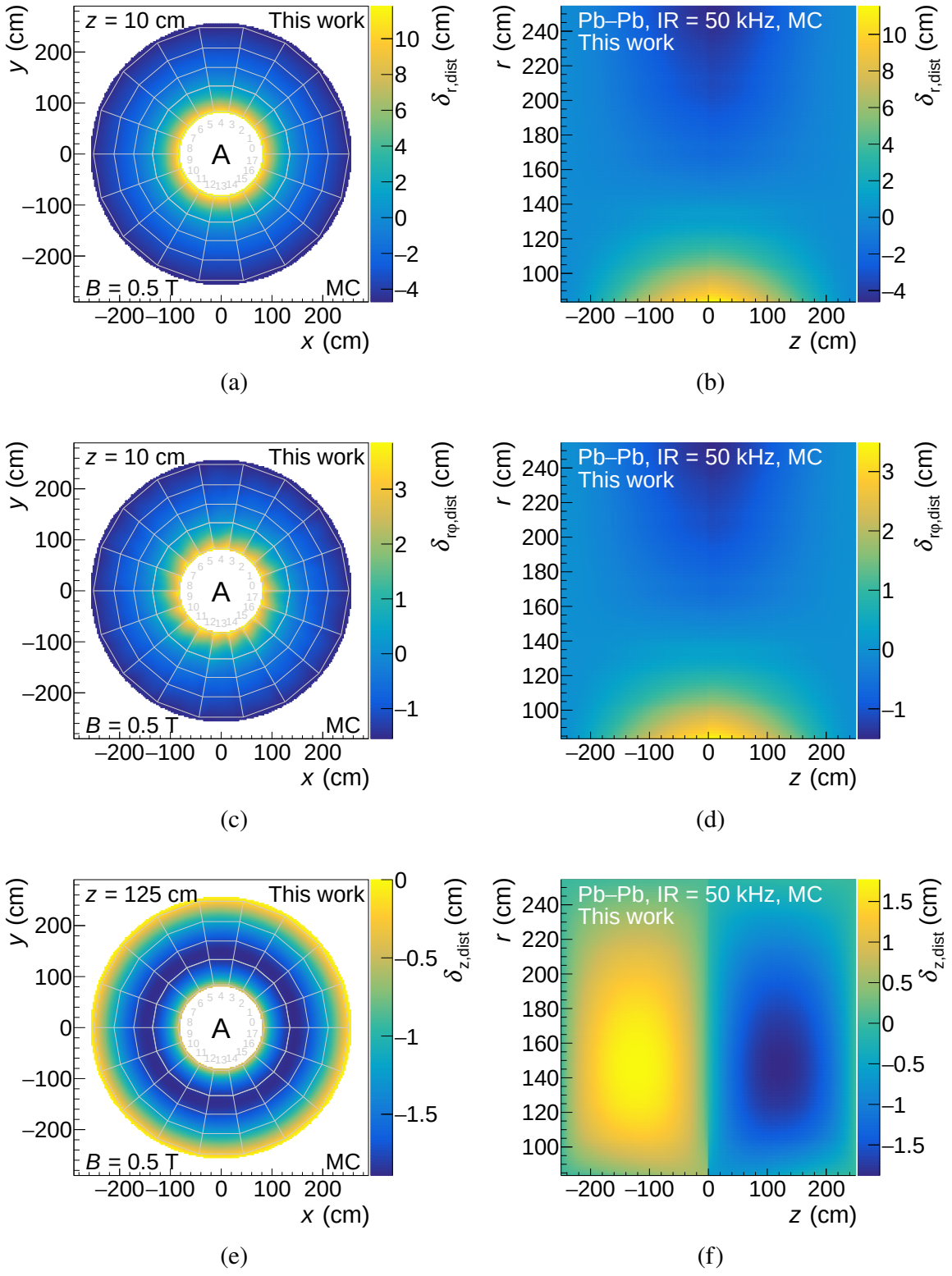

Figure 4.6: Simulated space-charge distortions for a magnetic field of 0.5 T for 50 kHz Pb–Pb collisions in (a) and (b) the radial direction, in (c) and (d) the $r\varphi$-direction and in (e) and (f) the z-direction.

4.1.2 Space-charge density fluctuations

For a precise correction of the space-charge distortions, not only the long-term average space-charge density defined by the interaction rate and the collision type has to be taken into account, but especially the fluctuations of the space-charge density on short timescales. The relative space-charge density fluctuations are defined by the ratio of the root mean square (RMS) of the space-charge density σ_{sc} to the average space-charge density μ_{sc}. The relative space-charge density fluctuations due to statistical fluctuations in the number of collisions, variations in the primary and secondary track multiplicity, the track distribution within the TPC and energy loss variations of the tracks can be approximated by the expression derived in the TDR [29], extended with terms for secondary tracks from particle decays or conversions:

$$\frac{\sigma_{\mathrm{sc}}}{\mu_{\mathrm{sc}}} = \frac{1}{\sqrt{N^{\mathrm{ion}}_{\mathrm{pileup}}}} \sqrt{1 + \left(\frac{\sigma_{\mathrm{N}^{\mathrm{prim}}_{\mathrm{mult}}}}{\mu_{\mathrm{N}^{\mathrm{prim}}_{\mathrm{mult}}}}\right)^2 + \left(\frac{\sigma_{\mathrm{N}^{\mathrm{rel\,sec}}_{\mathrm{mult}}}}{\mu_{\mathrm{N}^{\mathrm{rel\,sec}}_{\mathrm{mult}}}}\right)^2 + \frac{1}{F}\left[1 + \left(\frac{\sigma_{\mathrm{Q}^{\mathrm{prim}}_{\mathrm{track}}}}{\mu_{\mathrm{Q}^{\mathrm{prim}}_{\mathrm{track}}}}\right)^2 + \left(\frac{\sigma_{\mathrm{Q}^{\mathrm{sec}}_{\mathrm{track}}}}{\mu_{\mathrm{Q}^{\mathrm{sec}}_{\mathrm{track}}}}\right)^2\right]}, \tag{4.14}$$

where:

σ_{sc} = RMS of the space-charge density,
μ_{sc} = average space-charge density,
$N^{\mathrm{ion}}_{\mathrm{pileup}}$ = average number of collisions which contribute to the space-charge density,
$\sigma_{\mathrm{N}^{\mathrm{prim}}_{\mathrm{mult}}}$ = RMS of the primary track multiplicity,
$\mu_{\mathrm{N}^{\mathrm{prim}}_{\mathrm{mult}}}$ = average primary track multiplicity,
$\sigma_{\mathrm{N}^{\mathrm{rel\,sec}}_{\mathrm{mult}}}$ = RMS of the number of secondaries per primary,
$\mu_{\mathrm{N}^{\mathrm{rel\,sec}}_{\mathrm{mult}}}$ = average number of secondaries per primary,
F = average number of primaries and secondaries in a subvolume of the TPC,
$\sigma_{\mathrm{Q}^{\mathrm{prim}}_{\mathrm{track}}}$ = RMS of the energy loss variations of primaries,
$\mu_{\mathrm{Q}^{\mathrm{prim}}_{\mathrm{track}}}$ = average energy loss variations of primaries,
$\mu_{\mathrm{Q}^{\mathrm{sec}}_{\mathrm{track}}}$ = RMS of the energy loss variations of secondaries,
$\sigma_{\mathrm{Q}^{\mathrm{sec}}_{\mathrm{track}}}$ = average energy loss variations of secondaries.

Figure 4.7 shows the relative space-charge density fluctuations from Equation 4.14 and from different Monte Carlo (MC) simulations as a function of the number of ion pile-up events. The individual contributions in Equation 4.14 are obtained by MC simulations. The black line shows the expected space-charge density fluctuations due only to the Poissonian fluctuations in the number of collisions. The black diamonds show

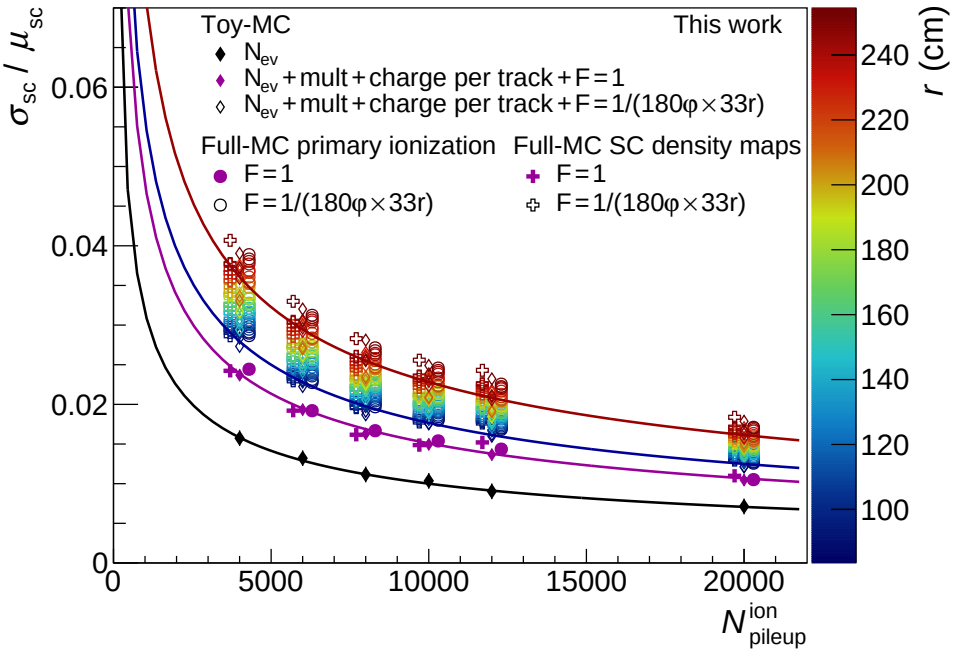

Figure 4.7: Space-charge density fluctuations from different MC simulations as a function of the number of ion pile-up events with the expectations from an analytical formula. Data taken from [72].

the corresponding results from a simple Toy-MC. The magenta line and the magenta markers, which are shifted next to each other along the x-axis for better visualization, show the average space-charge density fluctuations in the full volume of the TPC. The magenta crosses show the results from the simulated space-charge density maps described in the previous section. The magenta circles show the fluctuations of the primary ionization from MC and the diamonds represent the results from a Toy-MC. For 50 kHz Pb–Pb collisions, corresponding to 10 000 ion pile-up events, the space-charge density fluctuations in the full volume in the TPC reach about 1.5%, leading to space-charge distortion fluctuations of the order of millimeters, which have to be corrected on the relevant timescales of only about 10 ms [29]. The colored open markers show the space-charge density fluctuations in smaller volume elements, subdividing the full TPC volume into 180×33 sections in the φ-r plane, as a function of the radius. The blue and red lines show the corresponding expected fluctuations according to Equation 4.14 at the inner and outer radii, respectively. The relative space-charge density fluctuations increase toward larger radii due to larger statistical fluctuations, as low-momentum particles do not reach the outer radii of the TPC.

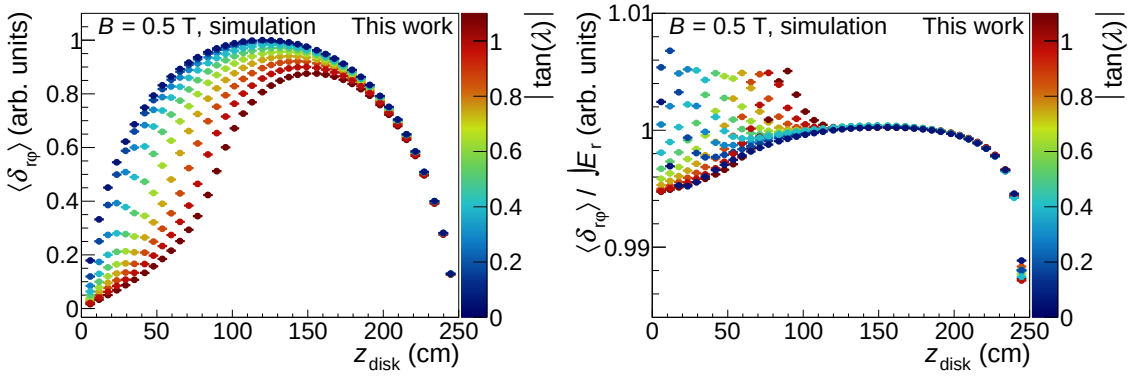

(a) (b)

Figure 4.8: (a) Mean space-charge distortions in the $r\varphi$-direction of space-charge disks at different z-positions in the TPC, normalized to unity at their maximum, and (b) their ratio to the electric field in the radial direction integrated to the readout chambers and normalized to unity at its maximum.

4.1.3 Space-charge disks

The space-charge density due to IBF in the TPC is interpreted as space-charge disks constantly drifting from the readout chambers to the central electrode. The mean space-charge density of each space-charge disk varies due to the fluctuations discussed in the previous section. To get an estimate of the impact of these space-charge disks on the space-charge distortions, simulations are carried out by placing space-charge density disks at fixed z-positions. Figure 4.8a shows the mean space-charge distortions in the $r\varphi$-direction, with the maximum normalized to unity, as a function of the z-position of the space-charge disks z_{disk} for different track dip angles, indicated on the color axis. In general, the response of the space-charge distortions strongly depends on the z-position of the space-charge disk and the dip angle of the track respectively the z-position of the drift electron. Figure 4.8b shows the ratio of these space-charge distortions to the integrated electric field in the radial direction along the z-direction to the readout chambers, with the maximum normalized to unity. The ratio between these normalized quantities is less than 1%, implying that the space-charge distortions are primarily driven by the shape of the electric field in the radial direction. Thus, the space-charge disks close to the central electrode or to the readout chambers contribute significantly less to the space-charge distortions than space-charge disks near the center of the TPC. The inclusion of these z-dependent contributions of the space-charge disks in the space-charge correction procedure is described in detail in Section 4.3.

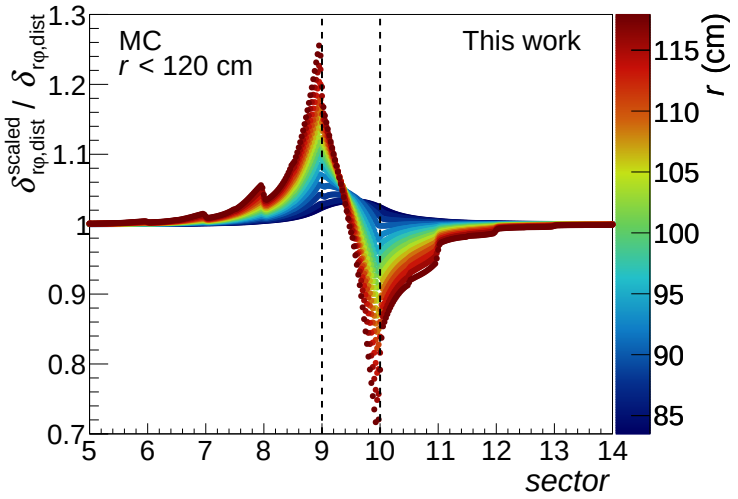

Figure 4.9: Simulation of the impact on the space-charge distortions in the $r\varphi$-direction when the IBF at the IROC in sector nine is lowered by 10% compared to the IBF of adjacent readout chambers.

4.1.4 Space-charge variations across readout chambers

To quantify the impact of a slightly higher or lower IBF for one readout chamber compared to adjacent readout chambers, the IBF at the different GEM stacks are individually reduced by 10%. The resulting space-charge distortions are calculated and compared to the space-charge distortions with nominal IBF. As an example, Figure 4.9 shows the ratio of the $r\varphi$-distortions after lowering the IBF in the IROC in sector nine to the corresponding nominal distortions. The change in IBF for one readout chamber leads to space-charge distortions with a steep gradient in the φ-direction, which becomes the largest close to the sector boundaries. In addition, the drift field in adjacent sectors is also strongly affected, resulting in space-charge distortions with rather steep gradients.

4.1.5 Magnetic field inhomogeneities

In 2005, the magnetic field components B_{r}, B_{φ} and B_{z} were measured by placing a probe inside of the L3 solenoid at different positions to be able to quantify the magnetic field components and the misalignment between the magnetic and the electric field, the $\vec{E} \times \vec{B}$ misalignment [73].

To get a smooth estimate of the magnetic field within the full volume of the TPC, a global parameterization of the measured magnetic field components is performed. Figures 4.10a and 4.10b show the magnetic field components within the TPC volume in the radial direction and in the φ-direction for a magnetic field of $-0.5\,\text{T}$ at $z = 10\,\text{cm}$,

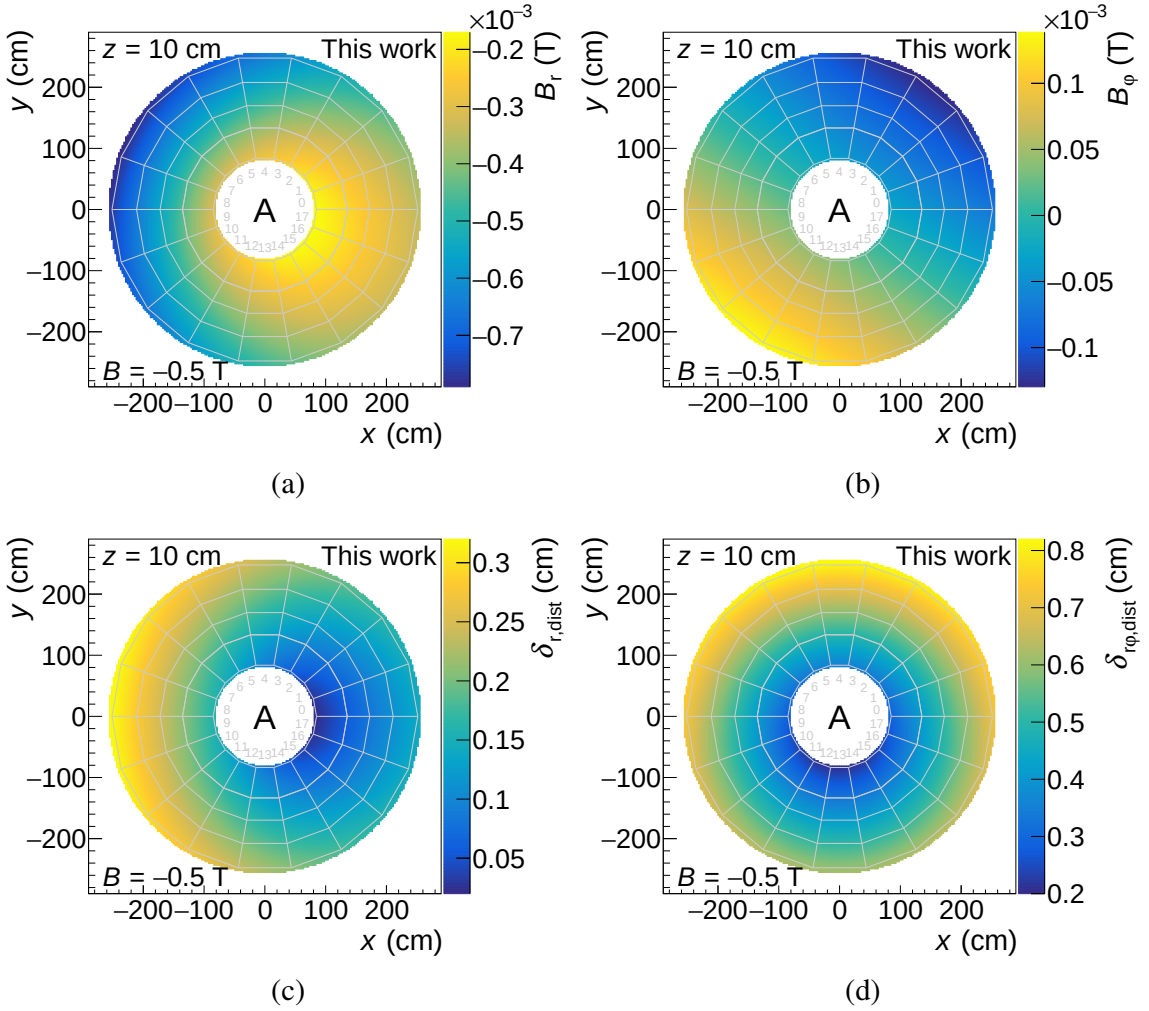

Figure 4.10: Magnetic field components of the L3 solenoid (a) in the radial direction and (b) in the φ-direction from a global parameterization of the magnetic field components within the volume of the TPC. The resulting space-point distortions due to the inhomogeneities of the magnetic field (c) in the radial direction and (d) in the $r\varphi$-direction.

from the global parameterization. These magnetic field components are about three orders of magnitude smaller than the magnetic field component in the z-direction, but they still cause significant space-point distortions. The global parameterization of the magnetic field components is used in the space-point distortion framework to calculate the space-point distortions due to the inhomogeneities of the magnetic field. Figures 4.10c and 4.10d show the resulting space-point distortions in the radial direction and in the $r\varphi$-direction. These static and rather smooth space-point distortions reach up to about 0.8 cm at the outer radii and they dominate the space-point distortions at low interaction rates when space-charge becomes negligible.

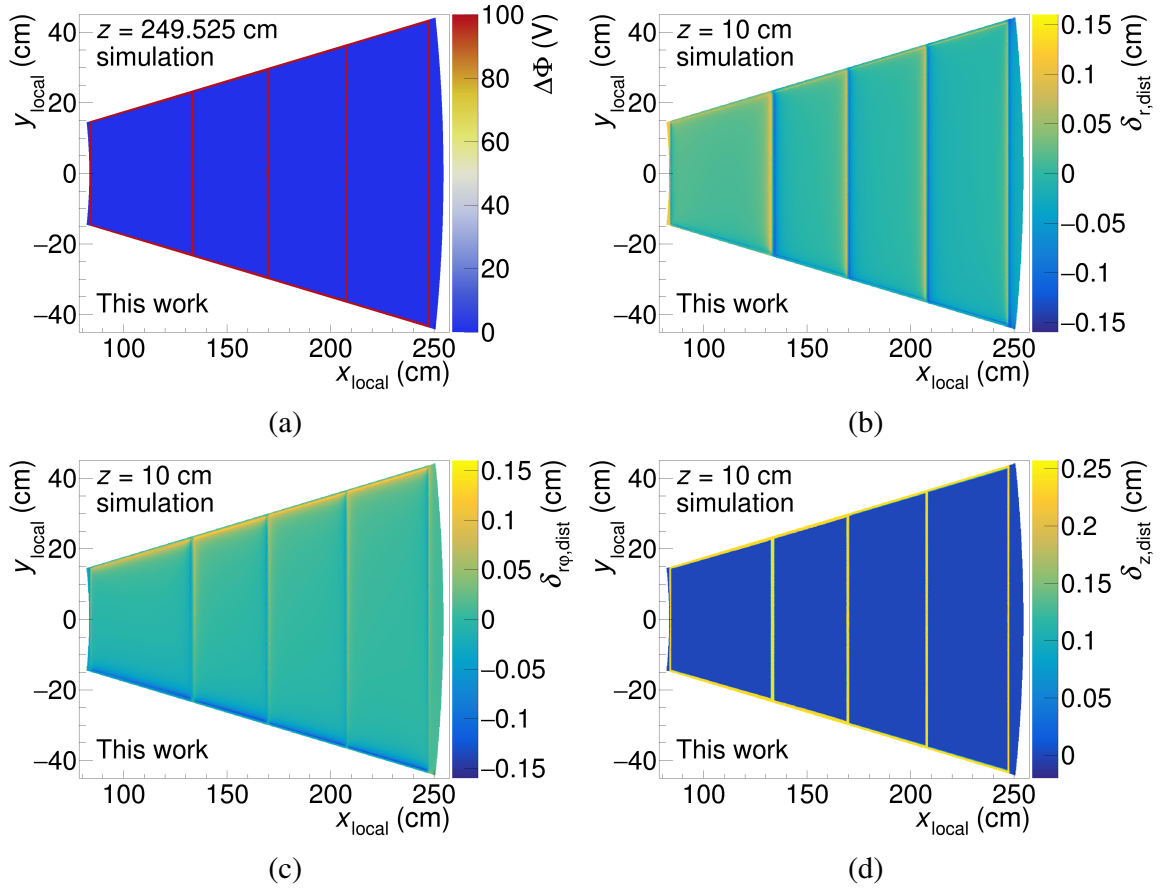

Figure 4.11: Simulation of the charging-up of the GEM frames: (a) Arbitrary potential of 100 V at the GEM frames and resulting space-point distortions (b) in the radial direction, (c) in the $r\varphi$-direction and (d) in the z-direction.

4.1.6 Charging-up of the GEM frames

In general, the 10 mm wide GEM frames on which the GEM foils are stretched charge up when electrons are attached to them. Since the GEM frames are made of an insulating material, electrons remain on the surface of the GEM frames for a certain amount of time, resulting in a change in the potential of the GEM frames. During the operation of the TPC, the GEM frames charge up by electrons drifting to the readout chambers until no electric field lines end on the GEM frames. This charging-up process leads to interaction rate and time-dependent space-point distortions at the sector boundaries. The inhomogeneities of the electric field components due to charging-up of the GEM frames are simulated in the space-point distortion framework by defining the potentials at the GEM frames as boundary conditions of the potential when solving Equation 4.1. Figure 4.11a shows the relative potential of the GEM frame with respect to the nominal potential, which is defined at an arbitrary value of 100 V, for one sector. Figures 4.11b–4.11d show the

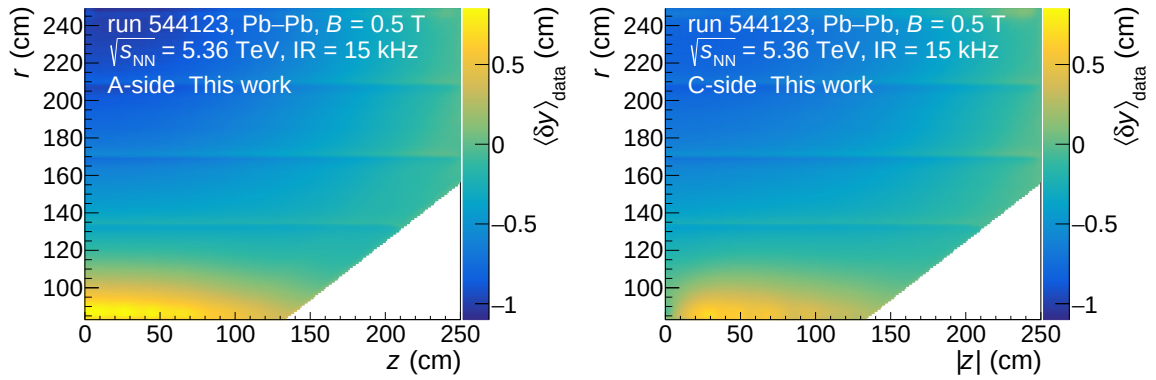

(a) (b)

Figure 4.12: Mean δy residuals for the (a) A-side and (b) C-side as a function of the radius and the z-position.

resulting space-point distortions due to the potential difference at the GEM frame in the radial direction, in the $r\varphi$-direction and in the z-direction. The space-point distortions occur mostly between the GEM stacks for the radial distortions and for the $r\varphi$-distortions at the sector edges. The space-point distortions in the z-direction are equally strong along the GEM frame and very well localized. Since the charging-up process is difficult to predict and depends on variables such as interaction rate and collision type, the absolute value of the boundary potential is a free parameter, which has to be determined from measured data.

4.1.7 Charging-up of the inner field cage vessel

Already during Run 1 and Run 2, significant φ-symmetric space-point distortions were observed on the C-side near the inner field cage close to the central electrode [74]. These space-point distortions were treated in the track reconstruction only by increasing the errors in the cluster-to-track association. However, the exact mechanism producing these space-point distortions remained unknown.

To analyze and model these space-point distortions in Run 3, data extracted with the procedure described in Section 3.7.4 is used. The δy residuals are stored in a two-dimensional map as a function of the radius and the z-position due to the symmetry of these space-point distortions in the φ-direction. For each position in the two-dimensional map, the mean of the δy residuals is extracted as an estimate of the space-point distortions. Figures 4.12a and 4.12b show the extracted mean values of the δy residuals from the two-dimensional map for the A-side and C-side for one Pb–Pb run. The space-point distortions, which are dominated mostly by space-charge and $\vec{E} \times \vec{B}$ misalignment, reach

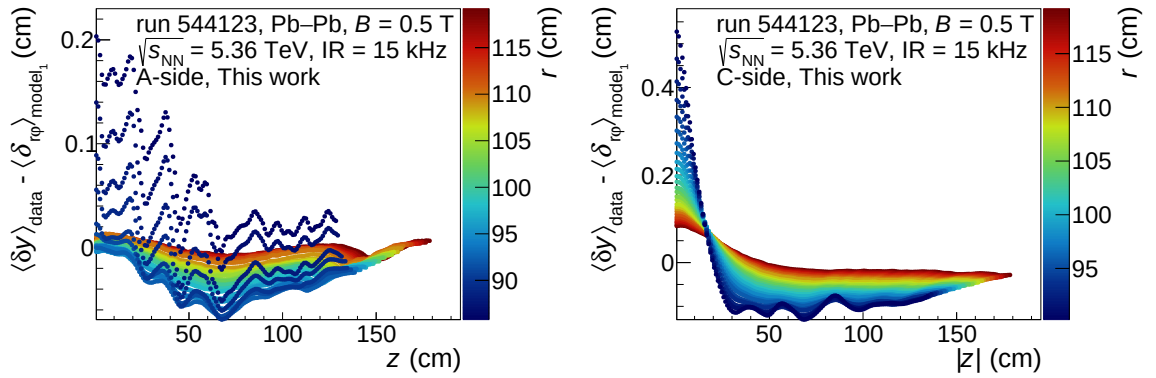

(a) (b)

Figure 4.13: Residuals between the mean δy residuals and the space-point distortions from the analytical models for space-charge, the $\vec{E} \times \vec{B}$ misalignment and the charging of the GEM frames for the (a) A-side and (b) C-side.

up to one centimeter at inner radii. The steep change in the space-point distortions at $r \approx 135\,\text{cm}$, $r \approx 170\,\text{cm}$ and $r \approx 210\,\text{cm}$ along the z-direction is caused by the charging of the GEM frames as discussed in the previous section.

To get an estimate of the space-point distortions close to the inner field cage due to charging-up and other possible effects, the analytical space-point distortion models shown in the previous sections for the space-charge (model_{SC}), $\vec{E} \times \vec{B}$ misalignment ($\text{model}_{\vec{E}\times\vec{B}}$) and charging of the GEM frames ($\text{model}_{\text{Frame}}$) are combined into a composed model referred to as model_1 in this section. This composed model is expressed with the linear scaling parameters c_{SC} and c_{Frame} as:

$$\text{model}_1 = \text{model}_{\vec{E}\times\vec{B}} + c_{\text{SC}} \cdot \text{model}_{\text{SC}} + c_{\text{Frame}} \cdot \text{model}_{\text{Frame}} \,. \tag{4.15}$$

The scaling parameter c_{SC} is used to account for uncertainties, mostly in IBF, in the simulation of the space-charge density. The scaling parameter c_{Frame} accounts for the unknown magnitude of the charging of the GEM frames. Both scaling parameters are extracted by a multidimensional linear parameterization of the combined analytical model fitted to the data. Figures 4.13a and 4.13b show the difference between the mean δy residuals and the mean space-point distortions in the $r\varphi$-direction of the combined analytical model_1 as a function of the z-position for the A-side and C-side, respectively. The radial position is indicated on the color axis. On the A-side, oscillating space-point distortions of up to 0.2 cm occur in data, most likely due to the finite field cage strips and the coarsely spaced guard rings as described in Section 3.5. To develop

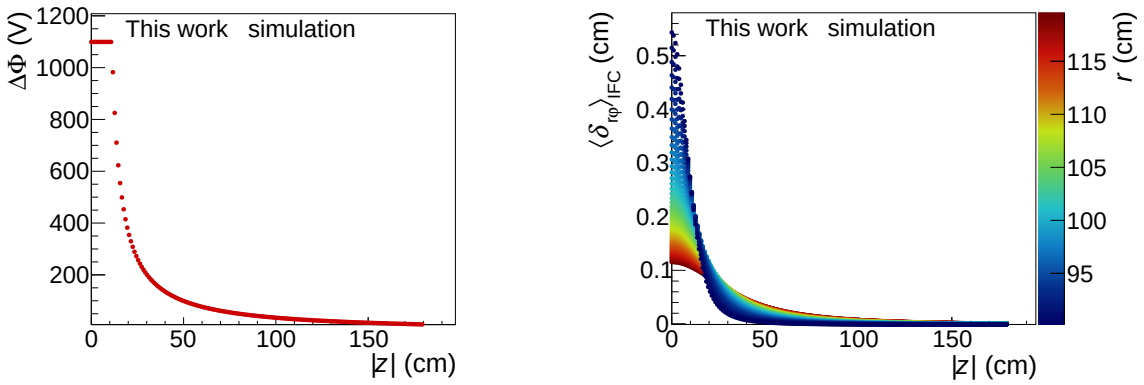

(a) (b)

Figure 4.14: (a) Boundary potential used to describe the charging of the inner field cage vessel on the C-side and (b) resulting space-point distortions in the $r\varphi$-direction.

an analytical model for these space-point distortions, further studies are needed with tools such as Garfield [45].

On the C-side, in addition to the oscillating space-point distortions, a strong increase of up to 0.5 cm in the space-point distortions in the data to the central electrode occurs. This increase is assumed to be caused by an imperfection in the first guard ring, resulting in charging of the inner field cage vessel from the central electrode to the first guard ring. Due to the missing first field cage strip and the finite size of the field cage strips, the potential of the charged field cage vessel can leak significantly into the volume of the TPC, causing the observed space-point distortions. Figure 4.14a shows the analytical boundary potential relative to the nominal potential at the inner field cage strips used for the approximation of the charging of the inner field cage vessel as a function of the z-position. The potential of the charged inner field cage vessel is approximated at the inner field cage strips by a homogeneous potential from the central electrode to the z-position of the first guard ring, which then falls off with the inverse of the z-position of the inner field cage strips. The height of the boundary potential is tuned such, that the resulting space-point distortions match the observed distortions in the data. Figure 4.14b shows the resulting space-point distortions in the $r\varphi$-direction from the assumed boundary potential. This analytical model is referred to as model$_{\text{IFC}}$ in this section. The space-point distortions of this analytical model fall steeply from the central electrode to about $z = 50$ cm and are most relevant for radii up to about $r = 120$ cm. The shape of the space-point distortions up to about $z = 20$ cm is comparable to the observed shape of the space-point distortions in the data shown in Figure 4.13b.

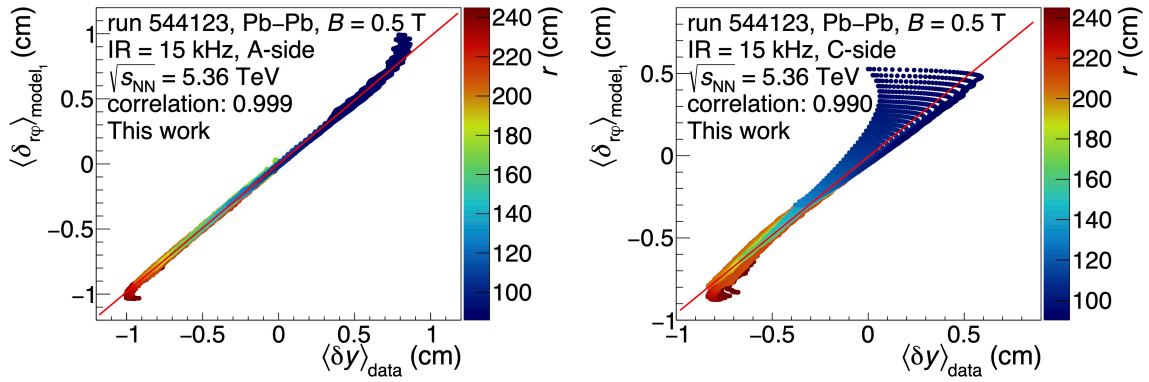

(a) (b)

Figure 4.15: Correlation between the mean δy residuals from data and from model$_1$ for the (a) A-side and (b) C-side.

Figure 4.15a shows the correlation of the space-point distortions from the combined model$_1$ and the mean δy residuals from the data for the A-side. The radius is shown on the color axis. The red line shows a linear parameterization to indicate the correlation between the data and the simulation. The analytical model of the space-point distortions agrees with the data with a nearly perfect correlation. For the regions near the central electrode at the inner radii, where the oscillating space-point distortions occur, and at the outer radii, where the space-point distortions due to the missing skirt electrode occur, larger deviations appear as no analytical models have yet been developed for these types of drift-field distortions. Figure 4.15b shows similarly as Figure 4.15a the correlation of the space-point distortions from the combined model$_1$ and the mean δy residuals from the data for the C-side. Also for the C-side, the largest deviations from the analytical models to the data occur at the inner radii due to the charging of the inner field cage vessel and at the outer radii.

The composed analytical model, referred to as model$_2$, contains in addition to model$_1$ the model for the charging of the inner field cage vessel model$_{\text{IFC}}$ and is defined as:

$$\text{model}_2 = \text{model}_{\vec{E}\times\vec{B}} + c_{\text{SC}} \cdot \text{model}_{\text{SC}} + c_{\text{Frame}} \cdot \text{model}_{\text{Frame}} + c_{\text{IFC}} \cdot \text{model}_{\text{IFC}} \,, \quad (4.16)$$

where c_{IFC} takes into account the magnitude of the charging of the inner field cage vessel. Figures 4.16a and 4.16b show the correlation between the space-point distortions from model$_2$ and the mean δy residuals from the data for the A-side and the C-side, respectively. As expected, the usage of the analytical model for the charging of the inner field cage vessel is nearly negligible for the A-side. The usage of model$_2$ for the C-side

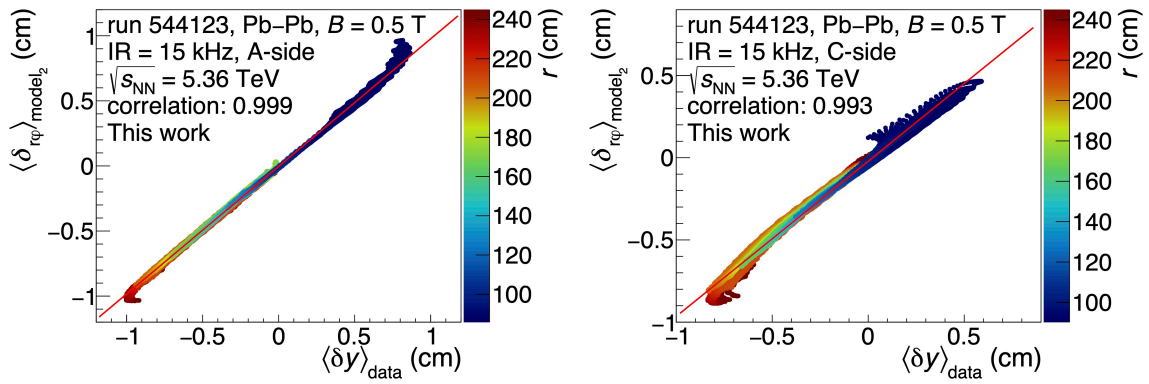

(a) (b)

Figure 4.16: Correlation between the mean δy residuals from data from model$_2$ for the (a) A-side and (b) C-side.

significantly improves the analytical description of the space-point distortions compared to model$_1$. Thus, model$_2$ provides sufficient agreement for a first-order description of the space-point distortions due to the charging of the inner field cage vessel.

For different runs with varying interaction rates and collision types, similar two-dimensional space-point distortion maps, as shown in Figures 4.12a and 4.12b, are created to quantify the dependence of the space-point distortions, caused by the charging of the inner field cage vessel, on the track density. For each two-dimensional map, the analytical models of the space-point distortions due to space-charge, $\vec{E}\times\vec{B}$ misalignment and charging of the GEM frames are fitted to the data and then subtracted from the data. Afterward, the analytical model for the charging of the inner field cage vessel is scaled to match the mean δy residuals for each analyzed run to extract the scaling factors c_{IFC} for the A-side and the C-side. Figure 4.17 shows these scaling factors for the analyzed Pb–Pb and pp runs as a function of the mean Integrated Digital Current (IDC) value of the corresponding run, used as a rough proxy for the track density. The IDCs are described in detail in Section 4.2.1. The scaling factors for the A-side are shown as diamonds and the scaling factors for the C-side are shown as circles. In general, for the A-side and C-side an increase in the space-point distortions due to the charging of the inner field cage vessel toward larger track densities occurs. This increase is caused by higher charge accumulation on the inner field cage vessel. For the A-side, however, the resulting space-point distortions are minor compared to the C-side. At high track densities, a saturation of the charging of the inner field cage vessel seems to occur on the C-side. In general, the sign of the $r\varphi$-distortions depends on the sign of the magnetic field, due to the dependence of the $r\varphi$-distortions on $\omega\tau$.

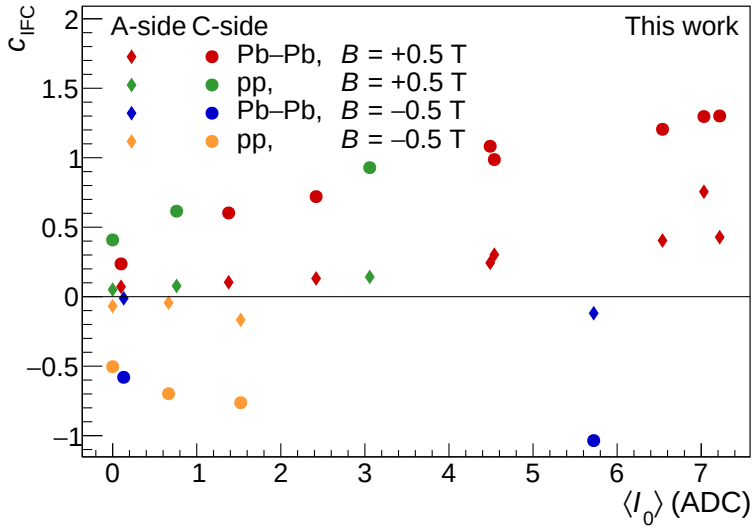

Figure 4.17: Scaling factor c_{IFC} of the analytical model for the charging of the inner field cage vessel as a function of the mean IDC value, used as a proxy for the track density, for Pb–Pb with interaction rates IR $<$ 40 kHz and for pp runs with interaction rates IR $<$ 1 MHz.

To correct the space-point distortions due to the charging of the inner field cage vessel, interaction rate dependent correction maps from the data-driven approach as described in Section 3.7.4 are created by the TPC experts with rather fine granularities to describe the steep decrease of the space-point distortions near the central electrode. However, further studies are needed to analyze the time evolution of these space-point distortions within a run to develop time-dependent correction procedures.

4.2 Time-dependent space-charge density variations

Short-term fluctuations in the interaction rate, the decay of the LHC beam and other effects cause time-dependent variations in the space-charge density, which have to be taken into account in the space-point distortion correction procedure.

4.2.1 Integrated Digital Currents

For the correction of the space-charge distortions and space-charge distortion fluctuations, a precise knowledge of the evolution of the space-charge density in the volume of the TPC is required. Since no direct measurement of the space-charge density in the TPC is possible, the measured signals on the readout pads are integrated over about one millisecond and are used as a proxy for the ions that are produced in the corresponding

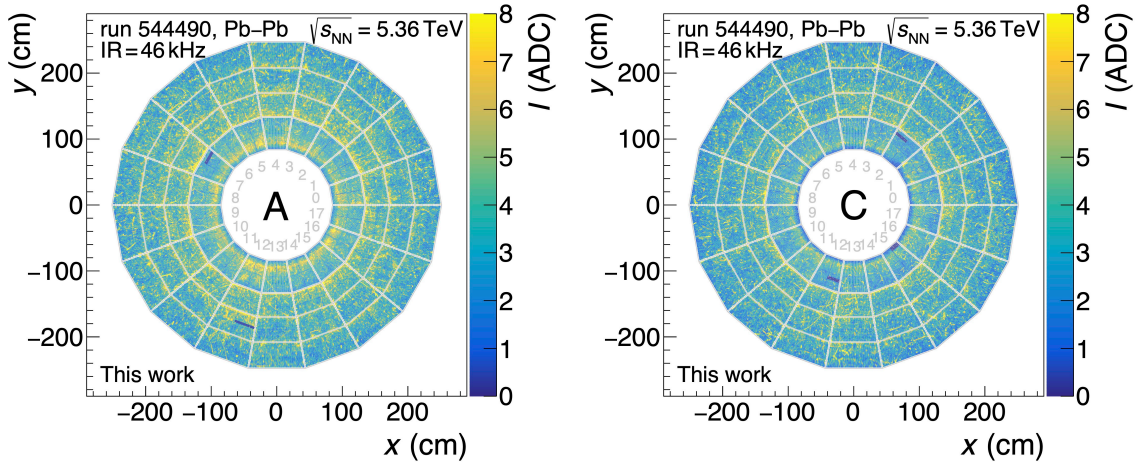

(a) (b)

Figure 4.18: IDCs for one integration interval of twelve orbits for (a) the A-side and (b) the C-side.

time interval. These integrated digits, referred to as IDCs, are shown as an example in Figures 4.18a and 4.18b for one integration interval for the A-side and the C-side, respectively. Single highly ionizing particle tracks are visible, as well as dead high voltage segments in sectors seven and twelve for the A-side, and sectors two, twelve and fifteen for the C-side. The IDCs serve as the main input for correcting time-dependent space-charge distortion variations on short timescales of the order of milliseconds and long timescales of the order of minutes. In addition to the IDCs, the reconstructed clusters from further detectors such as TOF, FT0, FV0 and FDD are integrated similarly. These integrated clusters are used to independently verify the IDCs and to provide redundancy for the IDCs in case of problems during the online processing of the IDCs. The integration of the TPC digits is performed on the Field Programmable Gate Arrays (FPGAs) of the CRUs during data taking in time intervals of twelve orbits. The raw IDCs are written to disk only for a small fraction of the data due to their large data rate of 1.8 GB s^{-1}. To get the full data-taking time covered with the IDCs, a dedicated online processing scheme is developed in the scope of this work to reduce the data rate of the IDCs. Figure 4.19 shows this processing scheme of the IDCs during the synchronous reconstruction: The FPGAs send the IDCs to the FLPs, where the IDCs are buffered for about one second. After buffering, the IDCs are sent to a calibration node, where the IDCs from all FLPs are merged and aggregated for about ten seconds. After aggregation of the IDCs, further processing is performed to be able to store the IDCs in the CCDB for the correction of the space-charge distortions and QA purposes. This processing

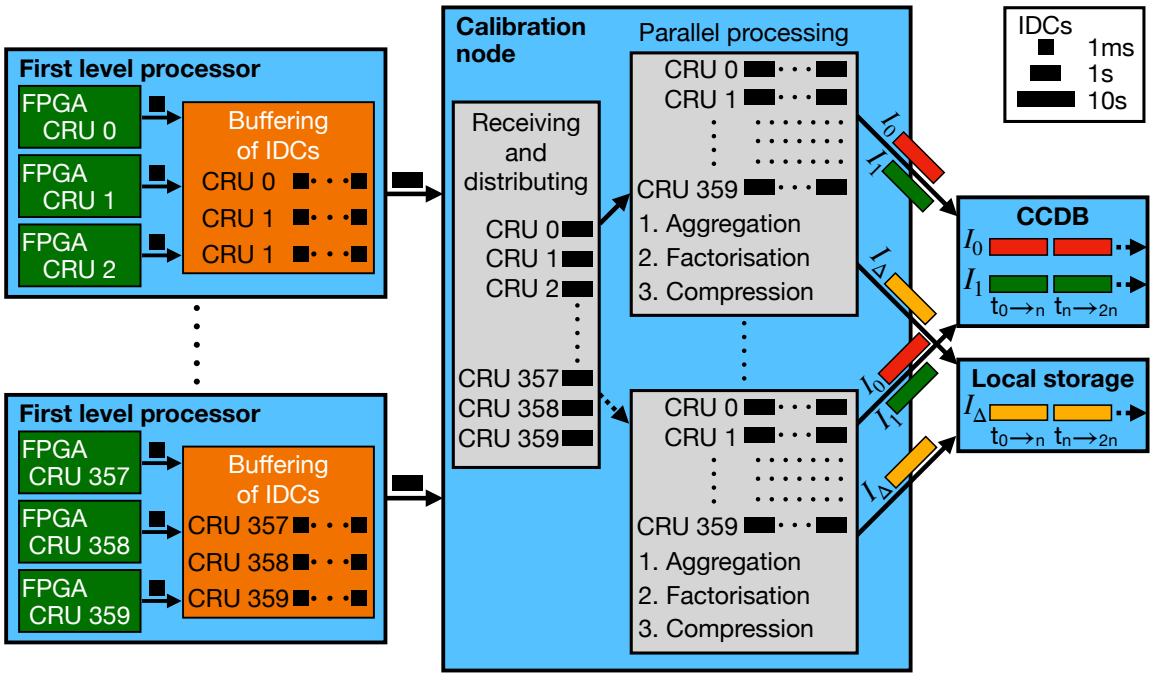

Figure 4.19: Schematic representation of the processing scheme of the IDCs during data acquisition.

reduces the data volume of the raw IDCs of 1.8 GB s^{-1} to about 40 MB s^{-1}, which is achieved through a factorization of the IDCs into the so-called zero-dimensional IDCs, the one-dimensional IDCs and the delta IDCs.

4.2.2 Zero-dimensional IDCs

In the first step, the IDCs I are averaged in time windows of $n_{\text{intervals}} \approx 10\,000$ integration intervals, corresponding to about ten seconds, for each readout pad per TPC side. This averaging yields the zero-dimensional IDCs I_0, which are stored in the CCDB and named for their coarse time sampling:

$$I_0(pad, t_{10\,\text{s}}) = \frac{1}{n_{\text{intervals}}} \sum_{t_{1\,\text{ms}}=0}^{n_{\text{intervals}}} I(pad, t_{10\,\text{s}} + t_{1\,\text{ms}}) \,, \tag{4.17}$$

where $t_{10\,\text{s}}$ denotes the sampling every ten seconds and $t_{1\,\text{ms}}$ denotes the integration interval of the IDCs of twelve orbits, which is expressed as one millisecond for simplicity. As an example, Figures 4.20a and 4.20b show these zero-dimensional IDCs for the A-side and the C-side, respectively, for a Pb–Pb run with an interaction rate of about 46 kHz. The pad-by-pad gain variations described in Section 3.4.3 are visible as the

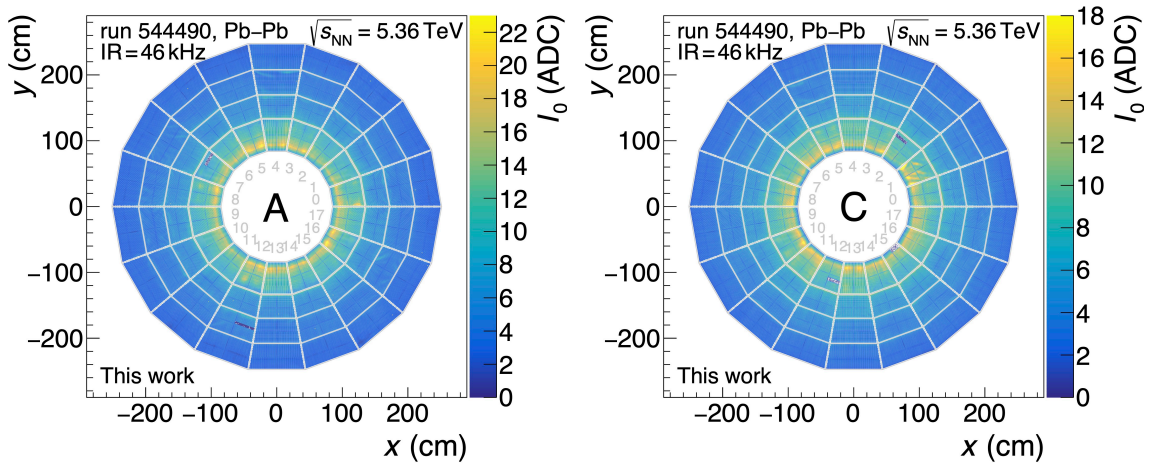

(a) (b)

Figure 4.20: Average IDCs over about ten seconds for the (a) A-side and the (b) C-side.

krypton gain map is not applied to the IDCs. The maximum I_0 is shifted from the inner radii of the TPC to halfway to the center of the IROCs due to the large radial space-charge distortions. As for the space-charge density, the general decrease in I_0 as a function of the radius is caused by the geometry of the TPC and tracks with low transverse momenta not reaching the outer radii of the TPC.
Averaging the zero-dimensional IDCs over all readout pads of a TPC side n_{pads} provides a precise measure of the mean space-charge density sampled every ten seconds:

$$\langle I_0 \rangle (t_{10\,\text{s}}) = \frac{1}{n_{\text{pads}}} \sum_{pad=0}^{n_{\text{pads}}} I_0(pad, t_{10\,\text{s}}) \,. \tag{4.18}$$

Figure 4.21 shows these averaged zero-dimensional IDCs as a function of the interaction rate and the corresponding ratio of temperature to pressure, indicated on the color axis, for the full 2023 Pb–Pb data. The spread of the averaged zero-dimensional IDCs for a given interaction rate is mostly caused by temperature and pressure variations, leading to gain variations due to the dependence of the first Townsend coefficient on temperature and pressure, as briefly described in Section 3.4.1. In addition, changes in the gas mixture can also affect, for example, the electron attachment, which directly influences the amplitudes of the measured signals. The use of the averaged zero-dimensional IDCs $\langle I_0 \rangle$ as a measure of the mean space-charge density takes by construction all environment variables into account that affect the gain and thus the corresponding space-charge density due to IBF.

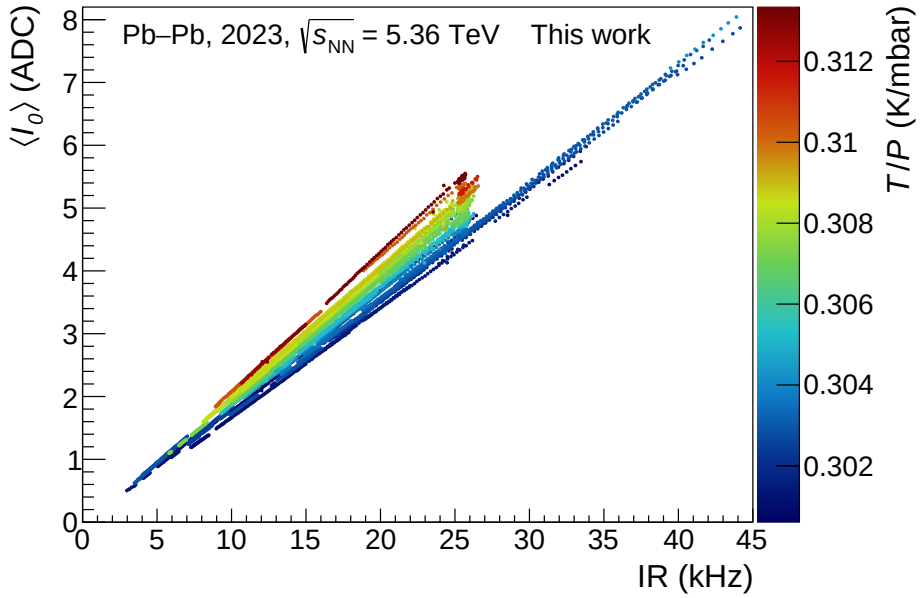

Figure 4.21: Averaged zero-dimensional IDCs $\langle I_0 \rangle$ as a function of the interaction rate for Pb–Pb collisions with the ratio of temperature to pressure on the color axis.

4.2.3 One-dimensional IDCs

The one-dimensional IDCs I_1, sampled every millisecond, describe the average fluctuations of the IDCs per TPC side with respect to the zero-dimensional IDCs and are obtained according to:

$$I_1(t_{1\,\mathrm{ms}}) = \frac{1}{n_{\mathrm{pads}}} \sum_{pad=0}^{n_{\mathrm{pads}}} \frac{I(pad, t_{1\,\mathrm{ms}})}{I_0(pad, t_{10\,\mathrm{s}})} \ . \tag{4.19}$$

Figure 4.22a shows the reconstructed one-dimensional IDCs for the A-side as a function of time for one Pb–Pb run. The distribution of these one-dimensional IDCs lies by definition around unity. The width of this distribution is mostly dominated by variations in the number of produced particles per collision and fluctuations in the interaction rate. The one-dimensional IDCs give a precise estimate of the fluctuations in the number of produced ions as a function of time. They are stored in the CCDB and are used as the main source for correcting the space-charge distortion fluctuations on short timescales of the order of milliseconds. Figure 4.22b shows the correlation of the one-dimensional IDCs of the A-side to the corresponding one-dimensional IDCs of the C-side. The red line shows a linear parameterization with a slope of 0.99. As expected, these IDCs

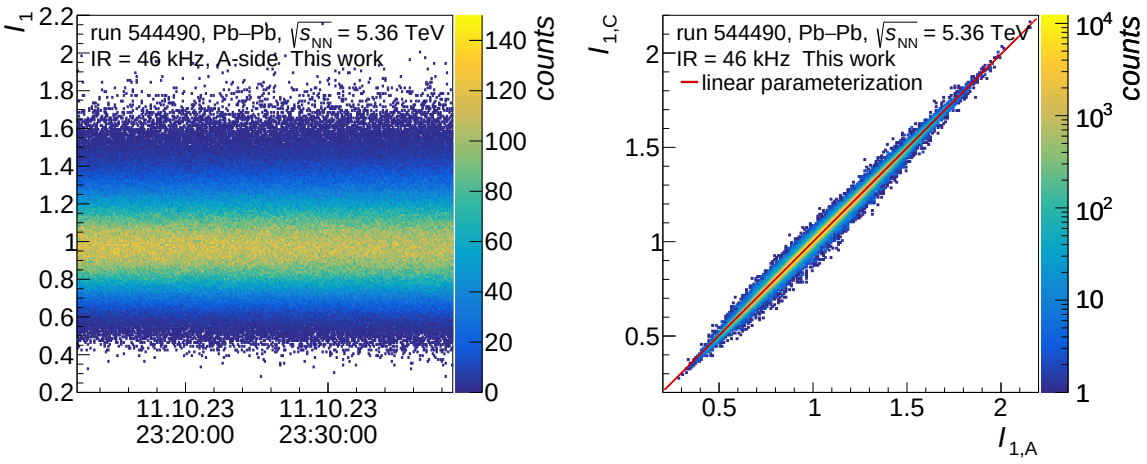

(a) (b)

Figure 4.22: (a) One-dimensional IDCs for the A-side as a function of time. (b) Correlation of the one-dimensional IDCs between the A-side and the C-side.

and thus the resulting average space-charge distortion fluctuations are nearly perfectly linearly correlated at these high interaction rates, due to the symmetry of the TPC and the centered collision vertex.

Figure 4.23 shows, similar to Figure 4.7, the space-charge density fluctuations from the different MC simulations, which are described in detail in Section 4.1.2, and additionally from data. The orange markers show the average space-charge density fluctuations in the full volume of the TPC from the data. These average fluctuations are derived from the widths of the distributions of the one-dimensional IDCs, subdivided into time windows of 100 seconds and averaged over an ion drift time of 200 milliseconds, as assumed in the corresponding simulations. The fluctuations from the one-dimensional IDCs agree very well with the results from the different MC simulations and the expectation from Equation 4.14. This agreement between data and MC confirms the approach to use the one-dimensional IDCs as a measure of the space-charge density fluctuations. Thus, the one-dimensional IDCs serve as an ideal input source for dedicated space-charge distortion correction procedures, as outlined in detail in Section 4.3.

4.2.4 Delta IDCs

The three-dimensional local fluctuations of the IDCs in space and time, sampled every millisecond, are denoted as I_Δ and referred to as delta IDCs. These delta IDCs are extracted by normalizing the IDCs by their ten-second average and the corresponding

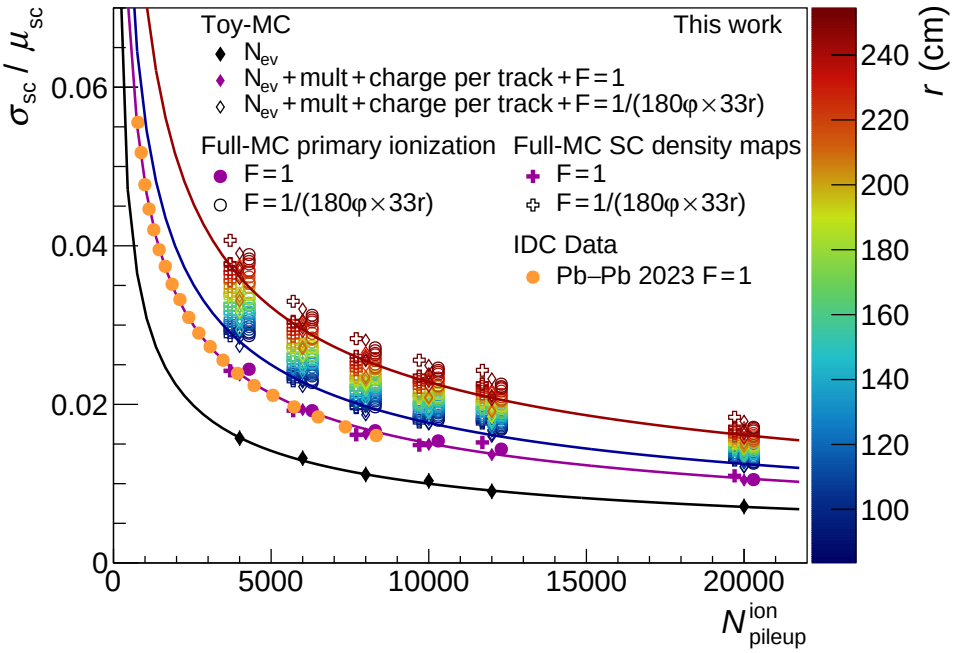

Figure 4.23: Space-charge density fluctuations from different MC simulations and for Pb–Pb data as a function of the number of ion pile-up events with the expectations from an analytical formula. Data taken from [72].

one-dimensional IDCs according to:

$$I_{\Delta}(pad, t_{1\,\mathrm{ms}}) = \frac{I(pad, t_{1\,\mathrm{ms}})}{I_0(pad, t_{10\,\mathrm{s}}) \cdot I_1(t_{1\,\mathrm{ms}})} - 1\,. \tag{4.20}$$

As an example, Figure 4.24a shows the delta IDCs for the IDCs shown in Figure 4.18a. The applied normalization of the IDCs to their long-term average effectively removes the radial dependence from the delta IDCs. In addition, the average fluctuations due to variations in the number of produced particles per collision and the fluctuations in the interaction rate are eliminated, leading to a narrower distribution than for the raw IDCs that is more suitable for compression algorithms.

Figure 4.24b shows the delta IDCs $I_{\Delta'}$ averaged over larger groups of pads. This averaging effectively reduces the data volume by about 90%. After averaging, further compression is performed by storing the averaged delta IDCs with one-byte precision instead of four-byte floating point precision. Nevertheless, these objects are not stored in the CCDB due to their file size, but rather on the same disk storage as the CTFs. The averaged delta IDCs could be used as input for a full three-dimensional correction of the space-charge distortion fluctuations by taking into account local variations of the track densities, which is beyond the scope of the present work.

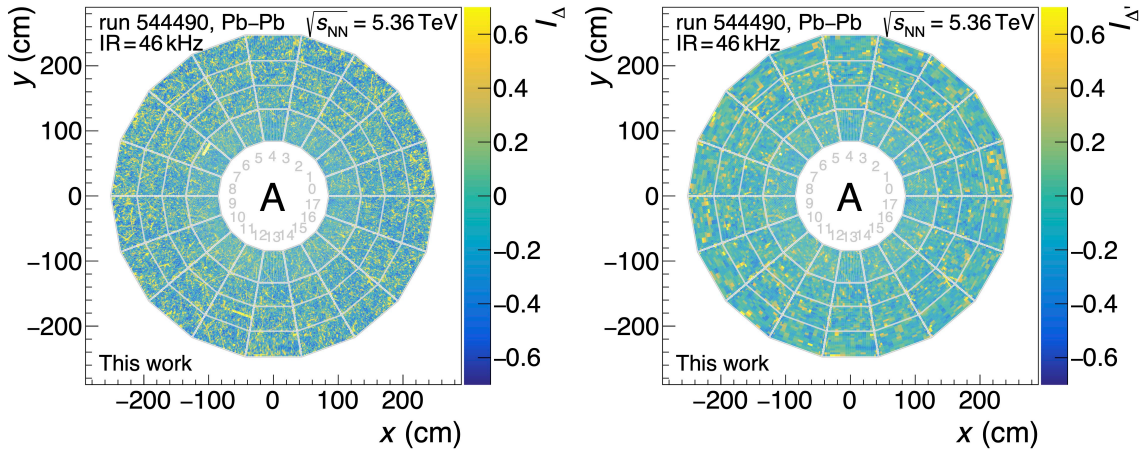

(a) (b)

Figure 4.24: Delta IDCs for one integration interval of twelve orbits (a) per readout pad and (b) averaged in larger groups of pads.

4.2.5 LHC beam profile in pp collisions

The scaled one-dimensional IDCs I_S, used as a precise measure of the LHC beam profile, are obtained by multiplying the one-dimensional IDCs sampled roughly every millisecond with their long-term averaged zero-dimensional IDC over about ten seconds according to:

$$I_S(t_{1\,\mathrm{ms}}) = I_1(t_{1\,\mathrm{ms}}) \cdot \langle I_0 \rangle (t_{10\,\mathrm{s}}) \,. \tag{4.21}$$

Figure 4.25a shows these scaled one-dimensional IDCs as a function of time for a pp run for the A-side. The sudden jumps in the LHC beam profile are caused by an automatic procedure called luminosity levelling [75], which is usually used during pp data taking to keep the interaction rate at ALICE around a fixed value. During levelling, the luminosity can change significantly on very short timescales, leading directly to a change in space-charge density and the corresponding distortions. Figure 4.25b shows in black the raw frequency spectrum up to 13 Hz from the Fast Fourier Transform (FFT) [76] of the scaled one-dimensional IDCs that are shown in Figure 4.25a. The red line shows smoothed values of the raw frequencies. The green line shows the smoothed frequency spectrum from the FFT of the integrated TOF clusters as an additional independent measure. The amplitudes in the frequency spectra translate directly to luminosity oscillations. It is confirmed by LHC experts [77] that the oscillations occur due to vibrations of the quadrupole magnets used for the luminosity levelling and focusing of the LHC

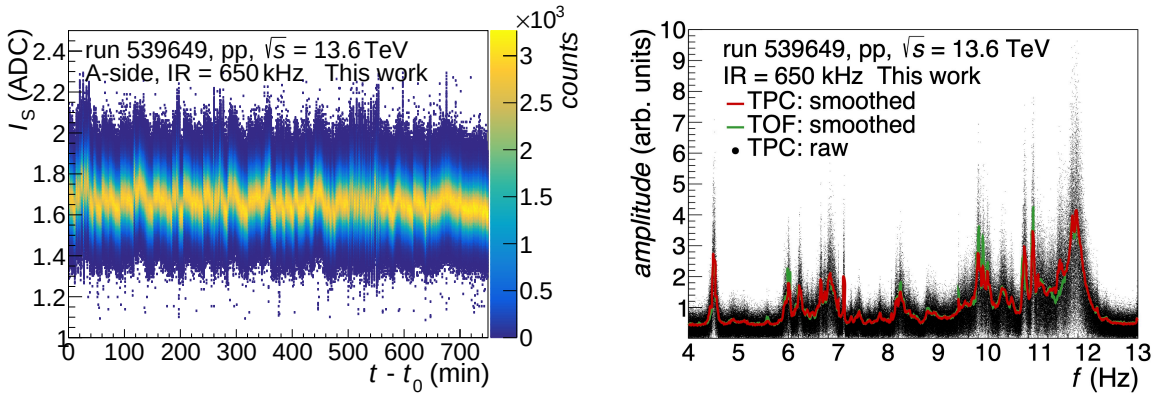

(a) (b)

Figure 4.25: (a) Scaled one-dimensional IDCs as a function of time for one pp run. (b) Raw and smoothed frequency spectra for the pp run.

beam. The final focusing of the beam to the interaction points at the LHC is performed by the so-called inner triplet system consisting of three quadrupoles. The mechanical resonance frequency of these quadrupoles, specifically the inner triplets, lies in the range of 5–40 Hz [77], leading to the luminosity oscillations. These oscillations lead to space-charge density oscillations on correspondingly short timescales.

4.2.6 LHC beam profile in Pb–Pb collisions

Figure 4.26a shows the LHC beam profile as a function of time for a typical Pb–Pb run. The rather large fluctuations compared to the pp run are mainly caused by the lower interaction rate for the Pb–Pb run in the range of 27 kHz down to 4 kHz compared to about 650 kHz for the pp run. These low interaction rates for Pb–Pb collisions lead to larger statistical fluctuations in the number of collisions for a given time interval than for pp collisions. In addition, rather large variations in the event multiplicity in Pb–Pb collisions further increase the fluctuations. The fluctuations of the space-charge density are covered in detail in Section 4.1.2. During Pb–Pb data taking in 2023, the maximum interaction rate was usually reduced down to below 30 kHz to provide stable beam conditions. At the beginning of the run shown in Figure 4.26a, the interaction rate is levelled to about 27 kHz for about 110 minutes. Afterward, the intensity of the LHC beam is too low to maintain stable interaction rates, leading to an exponential decay of the LHC beam down to about 4 kHz without levelling. The decay of the LHC beam results in significant time-dependent space-charge density and distortion variations. Figure 4.26b shows in black the raw frequency spectrum of the first 110 minutes. The red and green

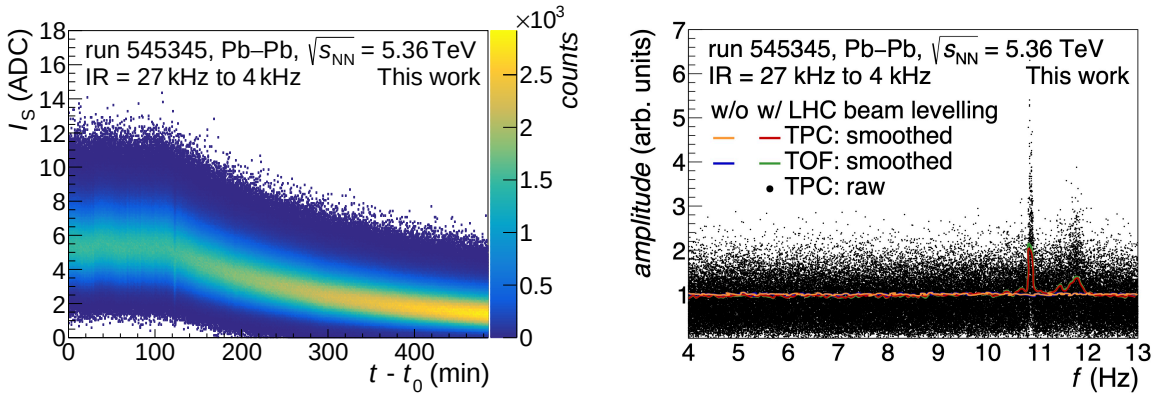

(a) (b)

Figure 4.26: (a) Scaled one-dimensional IDCs as a function of time for a Pb–Pb run. (b) Raw and smoothed frequency spectra for the Pb–Pb run.

lines show the smoothed frequency spectra for the TPC and TOF, respectively, which exhibit at about 10.8 Hz and 11.8 Hz a factor two lower amplitudes compared to the amplitudes in the pp run. The differences between these frequency spectra could be caused by the use of different levelling techniques. The orange and blue lines show the smoothed flat frequency spectra after the levelling is turned off, where no spikes in the frequencies occur. The strongly suppressed or absent luminosity oscillations, compared to the oscillations observed in pp runs, mitigate the space-charge density oscillations and the corresponding space-charge distortion variations in Pb–Pb data taking.

4.3 Time-dependent space-charge distortion correction

The correction procedure for the space-charge distortions applied during the track reconstruction is based on the correction maps produced by the data-driven approach described in Section 3.7.4.

For the correction of time-independent space-point distortions, such as the $\vec{E} \times \vec{B}$ misalignment and average space-charge distortions, correction maps M_{avg} created in an offline procedure by the TPC experts for every hour of the 2023 Pb–Pb data are used. These average correction maps describe, by construction, only the average space-point distortions for the time interval for which each correction map was created. For each correction map, the scaled one-dimensional IDCs I_S are averaged over the ion drift time for the time intervals used to create the correction map, denoted as $\langle I_{S,\text{avg}} \rangle$, to extract a measure of the mean space-charge density of the correction map.

A second correction map, denoted as M_Δ, is used to correct for short-term space-charge

distortion fluctuations of the order of milliseconds and long-term space-charge distortion variations, mainly due to the decay of the LHC beam, of the order of minutes. This second correction map describes the dependence of the space-point distortions on the change in space-charge density and is obtained by the numerical derivative of two correction maps for slightly different mean space-charge densities, ideally in the range of about 10% to 20%:

$$M_{\Delta} = \frac{M_{\text{avg+}} - M_{\text{avg-}}}{\langle I_{\text{S,avg+}} \rangle - \langle I_{\text{S,avg-}} \rangle} \ , \tag{4.22}$$

where $M_{\text{avg+}}$ is a correction map ideally for a slightly higher space-charge density $\langle I_{\text{S,avg+}} \rangle$ than that of the average correction map. The correction map $M_{\text{avg-}}$ is similarly a correction map for a slightly lower space-charge density $\langle I_{\text{S,avg-}} \rangle$ compared to the average correction map. For simplicity, the explicit dependencies of the correction maps on the three-dimensional position in the TPC are not given in Equation 4.22 and subsequent equations. The final correction map for a moment in time t is constructed from the average correction map and the linearly scaled derivative correction map, which are both combined according to:

$$M(t) = M_{\text{avg}} + M_{\Delta} \cdot \left(\frac{\sum_{t_{\text{sc}}=t_{\text{c}}}^{t} w(t_{\text{sc}} - t, z) \cdot I_{\text{S}}(t_{\text{sc}})}{\sum_{t_{\text{sc}}=t_{\text{c}}}^{t} w(t_{\text{sc}} - t, z)} - \langle I_{\text{S,avg}} \rangle \right), \tag{4.23}$$

where $t_c \approx t - t_{\text{d,ion}}$ describes the past time interval, approximately defined by the ion drift time, which contributes to the space-charge density. The weights w are defined at the relative time $t_{\text{sc}} - t$ and take into account that the impact of the space-charge disks from IBF on the space-charge distortions depends on their z-position, as shown in Section 4.1.3 for simulated space-charge disks. The position of the space-charge disks in the time direction is given by t_{sc} and the position of the drift electron from primary ionization by z. However, the weights used to scale the derivative correction map are extracted from real data, as described in the following section, instead of from the simulations, to take the proper ion drift time into account and to avoid assumptions and simplifications of the simulations. For a first-order correction, the weights can be set to unity.

4.3.1 Response of space-charge distortion fluctuations to IDCs

The space-charge density due to IBF in the TPC is interpreted as space-charge disks that contribute to the space-charge distortions with different weights depending on their position in the TPC and the z-position of the drift electrons. It is expected, as shown in Section 4.1.3 for simulations, that space-charge density disks close to the central electrode or the readout chambers contribute significantly less to the space-charge distortions than space-charge disks near the center of a TPC side. The contribution of the space-charge disks to the space-charge distortions is taken into account in the correction procedure by the weights in Equation 4.23. To determine these weights and to get an estimate of the space-point distortions, respectively the precision of the correction procedure, the TPC tracks are extrapolated to the collision vertex in the $r\varphi$-plane, and the distance of closest approach (DCA) to the primary vertex in radial direction ($\mathrm{DCA_r}$) is calculated. In the following, the term DCA always refers to the $\mathrm{DCA_r}$ in the radial direction and is used interchangeably. The sign of the DCAs is defined by the curvature of the extrapolated track with respect to the collision vertex. In case of uncorrected space-point distortions or imperfections in the space-point distortion correction procedure, the DCAs for particles originating from the collision are shifted from zero to larger values. The average DCAs per TF, denoted by $\langle DCA_\mathrm{r}\rangle_\mathrm{TF}$, are calculated for each TPC side for ten track dip angle intervals to get an estimate of the average space-point distortions, respectively the precision of the corrections, as a function of time and $\tan(\lambda)$.
As an example, Figure 4.27a shows in black the averaged DCAs for a Pb–Pb run for the A-side as a function of time since the start of the run. The time intervals in which the frequent spikes in the DCAs occur are excluded from the determination of the weights, as the drift-field distortions causing these spikes are unrelated to space-charge distortions. The origin of these drift-field distortions and the developed correction procedure for the resulting space-point distortions are described in detail in Section 4.4. The linear decrease of the DCAs is caused by the decay of the LHC beam, leading to a decrease in the space-charge distortions as a function of time which is not properly treated in the correction procedure as only an average correction map was used during the reconstruction of this data. The fluctuations of the DCAs are mainly driven by the fluctuations of the space-charge distortions. The average DCAs within time intervals of ten seconds, denoted by $\langle DCA_\mathrm{r}\rangle_\mathrm{avg}$, are shown in red. Figure 4.27b shows for the same run as in Figure 4.27a the scaled one-dimensional IDCs as a function of time for the A-side. The average scaled one-dimensional IDCs within time windows of ten seconds,

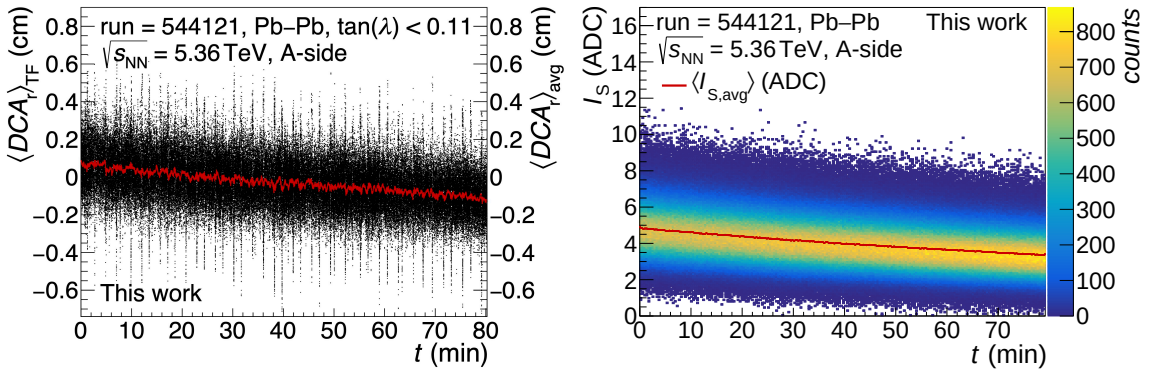

(a) (b)

Figure 4.27: (a) Average DCA of a TF ($\langle DCA_r \rangle_{TF}$) as a function of time in black, with its average in time windows of ten seconds ($\langle DCA_r \rangle_{avg}$) in red. (b) Scaled one-dimensional IDCs as a function of time with their averages in time windows of ten seconds in red.

denoted by $\langle I_{S,avg} \rangle$, are shown in red.

To extract the weights, Equation 4.23 is rewritten with the DCAs:

$$\langle DCA_r \rangle_{TF}(t) = \langle DCA_r \rangle_{avg}(t) + DCA_{r,\Delta} \left(\frac{\sum_{t_{sc}=t_c}^{t} w(t_{sc} - t, z) \cdot I_S(t_{sc})}{\sum_{t_{sc}=t_c}^{t} w(t_{sc} - t, z)} - \langle I_{S,avg} \rangle(t) \right), \tag{4.24}$$

where $DCA_{r,\Delta}$ describes the change in DCAs with respect to the change in IDCs. In the following expressions, the bounds of the summations and the dependencies of the variables are omitted for simplicity. By subtracting $\langle DCA_r \rangle_{avg}$ and defining $\langle \Delta DCA_r \rangle_{TF} = \langle DCA_r \rangle_{TF} - \langle DCA_r \rangle_{avg}$ Equation 4.24 is written as:

$$\langle \Delta DCA_r \rangle_{TF} = DCA_{r,\Delta} \left(\frac{\sum w \cdot I_S}{\sum w} - \langle I_{S,avg} \rangle \right), \tag{4.25}$$

Expanding $\langle I_{S,avg} \rangle$ by the sum of the weights yields:

$$\begin{aligned} \langle \Delta DCA_r \rangle_{TF} &= DCA_{r,\Delta} \left(\frac{\sum w \cdot I_S}{\sum w} - \frac{\sum w \cdot \langle I_{S,avg} \rangle}{\sum w} \right) \\ \langle \Delta DCA_r \rangle_{TF} &= \frac{DCA_{r,\Delta}}{\sum w} \sum \left(w \cdot I_S - w \cdot \langle I_{S,avg} \rangle \right) \\ \langle \Delta DCA_r \rangle_{TF} &= \frac{DCA_{r,\Delta}}{\sum w} \sum w \left(I_S - \langle I_{S,avg} \rangle \right). \end{aligned} \tag{4.26}$$

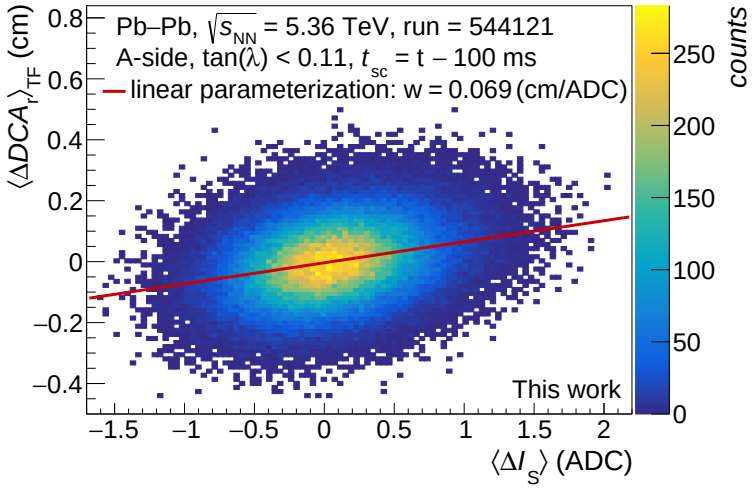

Figure 4.28: Correlation between $\langle \Delta DCA_r \rangle_{TF}$ and $\langle \Delta I_S \rangle$ for space-charge disks close to the center of the A-side.

The first term is neglected in Equation 4.26 when determining the weights, as this term is just a constant multiplicative factor that is the same for all weights:

$$\langle \Delta DCA_r \rangle_{TF}(t) \propto \sum_{t_{sc}=t_c}^{t} w(t_{sc} - t, z) \cdot \left(I_S(t_{sc}) - \langle I_{S,avg} \rangle(t) \right) . \tag{4.27}$$

The $\tan(\lambda)$ intervals of the DCAs are used in the following as a proxy for the z-position of the electrons. By assuming that the weights are constant over ten milliseconds yields with an arbitrary rather long ion drift time of $t_{d,ion} = 500\,\text{ms}$ and by defining the delta average IDCs over ten milliseconds as $\langle \Delta I_S \rangle(t_{sc}) = \frac{1}{10} \sum_{t_\Delta=t_{sc}}^{t_{sc}+10\,\text{ms}} \left(I_S(t_\Delta) - \langle I_{S,avg} \rangle(t) \right)$:

$$\begin{aligned} \langle \Delta DCA_r \rangle_{TF}(t) \propto \quad & w(-500\,\text{ms}, \tan(\lambda)) \cdot \langle \Delta I_S \rangle(t - 500\,\text{ms}) \\ & + w(-490\,\text{ms}, \tan(\lambda)) \cdot \langle \Delta I_S \rangle(t - 490\,\text{ms}) \\ & \dots \\ & + w(-10\,\text{ms}, \tan(\lambda)) \cdot \langle \Delta I_S \rangle(t - 10\,\text{ms}) \ . \end{aligned} \tag{4.28}$$

To extract the weights in Equation 4.28 as a function of $\tan(\lambda)$, $\langle \Delta DCA_r \rangle_{TF}$ and the corresponding $\langle \Delta I_S \rangle$ terms are calculated as a function of time for the three Pb–Pb runs which are available at the time of analysis. As an example, Figure 4.28 shows for the A-side the correlation between $\langle \Delta DCA_r \rangle_{TF}$ and $\langle \Delta I_S \rangle$ for the time $t - 100\,\text{ms}$, which corresponds to space-charge disks close to the center of the A-side. The red line shows a linear parameterization indicating the correlation between $\langle \Delta DCA_r \rangle_{TF}$ and $\langle \Delta I_S \rangle$. The

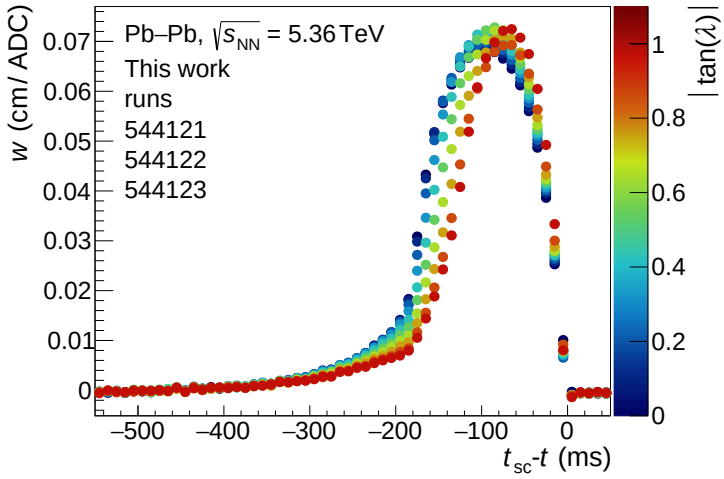

Figure 4.29: Weights of the contribution of space-charge disks to the space-charge distortions as a function of time and $\tan(\lambda)$.

slope of the linear parameterization yields directly the weight $w = 0.069\,\text{cm/ADC}$ for the given time interval.

For each of the analyzed runs, a multidimensional linear parameterization of $\langle \Delta DCA_r \rangle_{TF}$ as a function of the $\langle \Delta I_S \rangle$ terms is performed. The parameters from the parameterizations provide the weights for the ten $\tan(\lambda)$ intervals. Figure 4.29 shows the weights, averaged over the A-side and C-side and the three runs, as a function of the relative time with $\tan(\lambda)$ on the color axis. For the extraction of the weights, the time range for the space-charge density disks is extended to $-550\,\text{ms} < t_{sc} - t < 50\,\text{ms}$ to also extract the weights further in the past and in the future. The extracted weights consist of a short-term component up to about $-190\,\text{ms}$ and a long-term delayed component which decreases exponentially up to $-500\,\text{ms}$. The short-term component corresponds to space-charge disks from IBF and agrees with the expected ion drift time of about 190 ms from Equation 3.18. The origin of the long-term component needs further investigation. As expected, the weights are zero for time intervals in the future as these space-charge disks cannot contribute to the space-charge density for a given moment in time.

Figure 4.30 shows the correlation between $\langle \Delta DCA_r \rangle_{TF}$ and the sum in Equation 4.27 when the weights are set to unity as dashed lines and when the extracted weights are applied as full lines as a function of the relative time until which the weights are used. When the weights are applied, the correlation reaches a plateau at about $-250\,\text{ms}$ of up to a correlation of 0.93, which is significantly higher than the highest correlation of about 0.88 when all weights are set to unity. The correlation drops off sharply after about $-170\,\text{ms}$ when all weights are set to unity, as space-charge disks which contribute

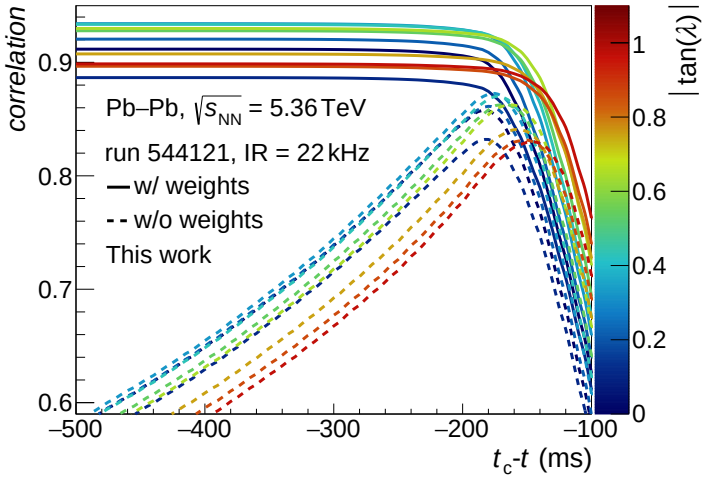

Figure 4.30: Correlation between $\langle \Delta DCA_r \rangle_{TF}$ and the sum in Equation 4.27 as a function of the relative time $t_c - t$. The full lines show the correlation when taking into account the weights from Figure 4.29. The dashed lines show the correlation when all weights are set to unity.

only marginally to the space-charge distortions are greatly overweighted. The high correlations between the IDCs and the DCAs indicate a very precise correction procedure when using the IDCs combined with the weights. For simplicity in the correction procedure, the extracted weights are averaged over $\tan(\lambda)$. These averaged weights are uploaded to the CCDB and automatically applied during the space-charge distortion correction procedure when composing the correction map for each TF according to Equation 4.23 with the weights up to $t_c - t = -500$ ms.

Figure 4.31a shows the correlation between the DCAs for the A-side $\langle DCA_{r,A} \rangle_{TF}$ and the corresponding DCAs for the C-side $\langle DCA_{r,C} \rangle_{TF}$ as a function of the absolute track dip angle for three different space-charge distortion correction procedures. The mean correlations of the different correction procedures are shown as dashed lines. The red markers show the correlations when the second term in Equation 4.23 is not taken into account in the space-point distortion correction procedure, i.e. when the space-charge distortion fluctuations are not corrected in the track reconstruction. The high correlation of about 0.8 between the DCAs of the A-side and the C-side indicates correlated space-point distortions due to the space-charge distortion fluctuations that are not corrected. The green markers show the correlations when the weights in Equation 4.23 are set to unity with a maximum relative time of $t_c - t = -170$ ms, which yields the best correlation when no weights are used as shown in Figure 4.30. This correction procedure gives a first-order correction of the space-charge distortion fluctuations and was applied in the

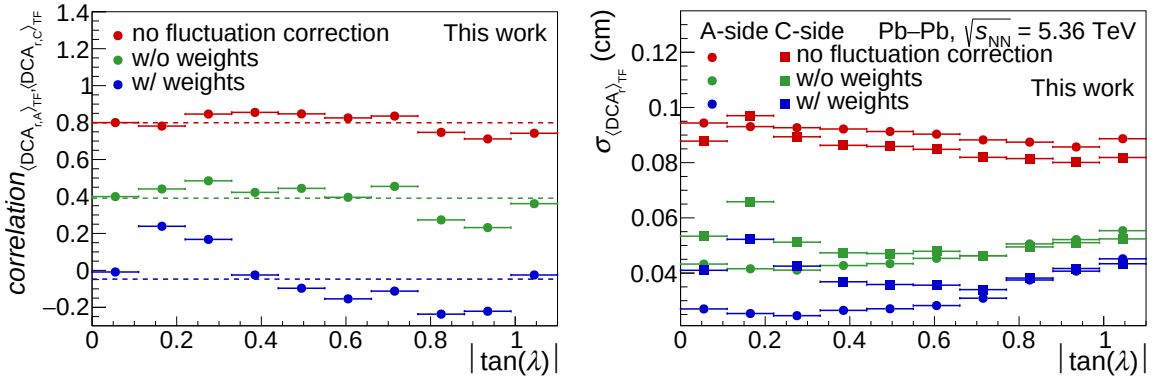

(a) (b)

Figure 4.31: (a) Correlation of the mean DCA per TF $\langle DCA_r \rangle_{TF}$ for the A-side and the C-side as a function of the absolute track dip angle for three space-charge distortion correction procedures. (b) Standard deviation of $\langle DCA_r \rangle_{TF}$ for the A-side and the C-side for the three correction procedures.

first asynchronous reconstruction pass of the Pb–Pb data in 2023. The blue markers show the correlations when using the averaged z-independent weights in Equation 4.23. These weights have been used in the space-charge distortion correction procedure since the second asynchronous reconstruction pass of the Pb–Pb data. The resulting correlation is on average -0.05, indicating on average a very precise space-charge distortion fluctuation correction. However, a residual dependence of the correlation as a function of the dip angle occurs, which could be further reduced by considering z-dependent weights. Figure 4.31b shows as another measure of the performance of the space-charge distortion fluctuation correction the standard deviation of $\langle DCA_r \rangle_{TF}$ for the A-side and C-side. The different marker colors represent the same space-charge distortion correction procedures as in Figure 4.31a. As expected, the space-charge distortion correction procedure is the most precise, with the smallest standard deviations, when composing the final correction map with the weights. The standard deviations of the DCAs are reduced by a factor of three for the A-side and by a factor of two for the C-side compared to the uncorrected space-charge distortion fluctuations. The worse resolution for the C-side compared to the A-side at small track dip angles might be caused by the charging-up of the inner field cage vessel.

The presented correction procedure for the space-charge distortion fluctuations provides sufficient precision such that other sources that are not covered in this work, such as biases in the extraction procedure of the correction maps or occupancy effects, dominate the tracking performance in the TPC.

4.4 M-shape distortions

The data taken in 2023 show a frequent, distinct M-shape pattern in the particle tracks DCAs for the A-side. These space-point distortions are referred to as M-shape distortions. Figure 4.32a shows, as an example for a selected time window, this M-shape pattern of the DCAs averaged over 30 TFs, denoted as $\langle DCA_{\mathrm{r}} \rangle_{30\,\mathrm{TFs}}$, as a function of time. For each DCA, its long-term moving median in a time window of 40 s, denoted as $\langle DCA_{\mathrm{r}} \rangle_{40\,\mathrm{s}}$, is subtracted to remove biases in the space-point correction procedure that affect the DCA. The red data points additionally show the currents of the power supply that is used to define the potential of the last inner field cage strip, i.e. the field cage strip closest to the readout chambers, on the A-side. The change in the potential of the last field cage strip, due to the change in the currents in the power supply, is transferred, decreasing linearly, through the resistor chain toward the central electrode where the potential is fixed. It is observed that the occurrence of the M-shape distortions and the spikes in the currents in the power supply are clearly correlated in time for the full 2023 data.
In addition, it is observed that the pressure in the water supply tank, which provides the liquid for the resistor rod cooling system, increases over time until it reaches a certain threshold, after which a vacuum pump is activated to restore the underpressure in the water supply tank to a low set point. The resistor rod cooling system is briefly described in Section 3.5. The increase in pressure over time is caused by bubbles being drawn into the underpressure resistor rod cooling system through a leak in the water supply [78]. Figure 4.32b shows the fraction of data affected by the M-shape distortions as a function of the time after which the vacuum pump is activated Δt_{pump}. The color axis indicates the pressure in the water supply tank P_{tank}. At the beginning of the operation of the vacuum pump, the amount of affected data increases significantly up to about 70%. The affected data drops steeply to about 20% within the first three hours after the vacuum pump is activated. Afterward, the affected data gradually decreases to about 10%, at which point the pressure exceeds its threshold, which leads to the activation of the vacuum pump. This clear correlation between the time after which the vacuum pump is activated and the fraction of affected data by the M-shape distortions indicates that the bubbles, in combination with the change in the currents of the power supply, are the cause of the M-shape distortions. These bubbles drift through the full resistor rod cooling system in the direction from the readout system toward the central electrode and back into the water supply tank. It is assumed that the bubbles charge up as they move through the cooling system due to the surrounding radiation. Thus, the charged

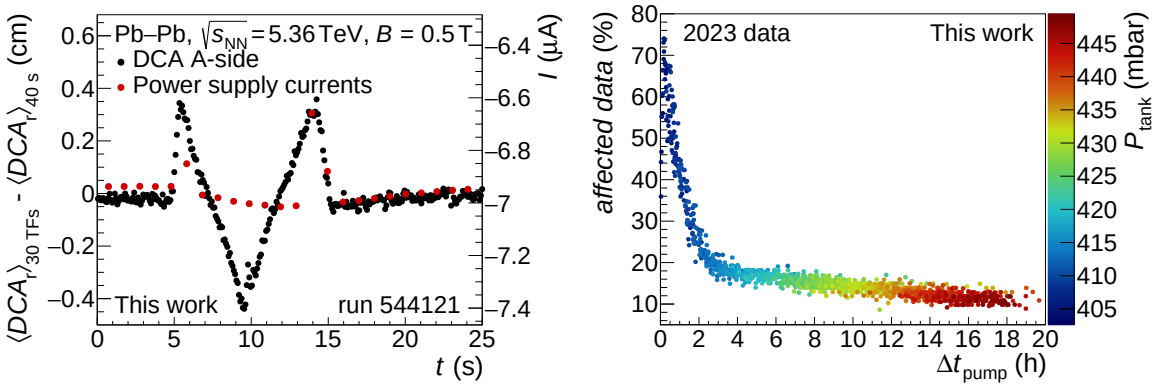

(a) (b)

Figure 4.32: (a) DCAs averaged over 30 TFs as a function of time in black for a selected time window and the currents of the power supply that are used to define the potential of the field cage strip closest to the readout chambers for the A-side in red. (b) Fraction of data affected by the M-shape distortions as a function of the time after a vacuum pump restores the underpressure in the water supply tank, with the pressure in the water supply tank on the color axis.

bubbles may induce currents in the inner field cage strips depending on their position in the cooling system. The increase of affected data by the M-shape distortions up to about 70% shortly after the vacuum pump is activated, could be caused by vibrations of the vacuum pump, which could significantly increase the number of bubbles being drawn into the cooling system. After about three hours, when the pump stops working, the relative pressure between the environment and the cooling system decreases further, such that fewer bubbles get drawn into the cooling system, reducing the affected data by the M-shape distortions to about 10%. However, further investigation is needed to determine the exact mechanisms by which the bubbles produce the M-shape distortions. Also, the cause of the change in the currents of the power supply used to define the potential of the last field cage strip requires further investigation.

4.4.1 Analytical correction approach

The data-driven approach described in Section 3.7.4 for creating space-point correction maps is not feasible for space-point distortions that change non-trivially on rather short timescales of the order of seconds, since either not enough particle tracks are available for the data-driven approach in these short time intervals, or it would be tedious to create thousands of correction maps. Therefore, an analytical approach is chosen to correct for the M-shape distortions. Figure 4.33a shows ten boundary potentials relative to the

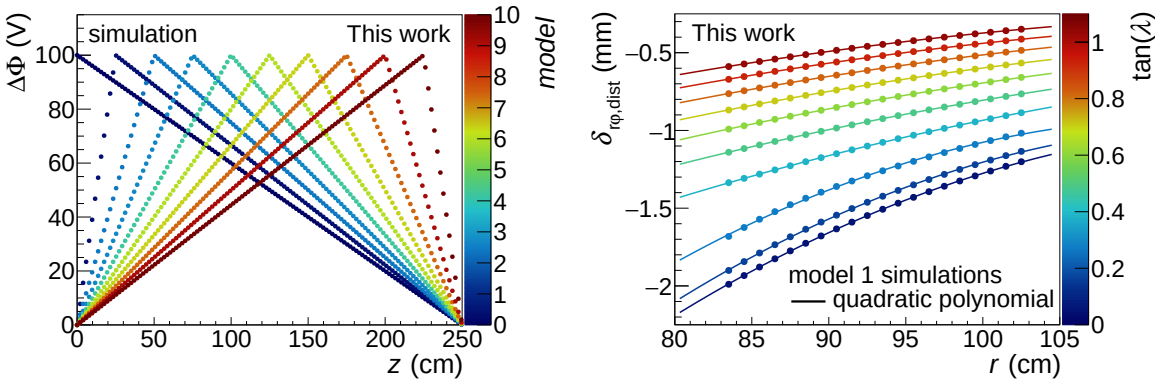

(a) (b)

Figure 4.33: (a) Boundary potentials relative to the nominal potential at the inner field cage of the A-side to model the M-shape distortions. (b) Resulting space-point distortions in the $r\varphi$-direction as a function of the radius for the first boundary potential model for ten high p_{T} tracks.

nominal potential of the inner field cage as a function of the z-position. These analytical models of boundary potentials are used to describe the DCAs in data. The models are φ-symmetric and chosen such that a linear combination of these models as a function of time can approximate the change in the potential at the field cage strip closest to the readout chambers and the bubble drifting through the resistor rod cooling system according to:

$$\Delta\Phi(t,z) = S \cdot \left[c_0(t) \cdot \Delta\Phi_0(z) + \cdots + c_9(t) \cdot \Delta\Phi_9(z)\right], \tag{4.29}$$

where c_j are time-dependent linear scaling parameters for the analytical models $\Delta\Phi_j$. The global scaling parameter S accounts for simplifications in the extraction procedure of the parameters c_j. To obtain these time-dependent scaling parameters, the DCAs for each analytical model are calculated as a function of $\tan(\lambda)$ and fitted to the measured DCAs. The procedure is described in the following: As an example for the first analytical model, Figure 4.33b shows the space-point distortions in the $r\varphi$-direction for ten simulated high p_{T} tracks with different $\tan(\lambda)$ angles as a function of the radius. The $\tan(\lambda)$ angle of the track is indicated on the color axis. These $r\varphi$-distortions are used as an estimate of the distorted space points of the track trajectories. The lines show parameterizations with a second-order polynomial as approximations of the trajectories of the distorted tracks. To approximate the DCA for each track, the parameterizations are evaluated at the ideal collision vertex, i.e. at $r = 0\,\mathrm{cm}$. The assumption of high p_{T} tracks leads to a bias in the approximated DCAs compared to the DCAs in data, as these DCAs

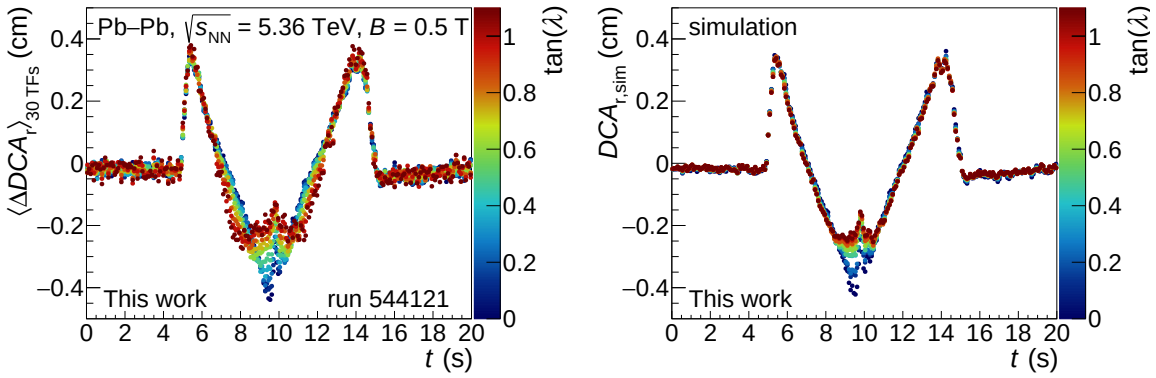

(a) (b)

Figure 4.34: (a) Averaged DCAs over 30 TFs as a function of time and tan(λ) for a selected time window. The baseline DCA for each tan(λ) angle is subtracted. (b) DCAs of the combined analytical models after tuning the models to the DCAs from data as a function of time and tan(λ).

are extracted by particle tracks over a wide p_T range, leading to the requirement of the scaling factor S in Equation 4.29. It is found that this scaling factor is roughly independent of collision type and interaction rate.

Figure 4.34a shows $\langle \Delta DCA_r \rangle_{30\,TFs}$ as a function of time and tan(λ) on the color axis, where $\langle \Delta DCA_r \rangle_{30\,TFs}$ is defined as:

$$\langle \Delta DCA_r \rangle_{30\,TFs}(t_i, \tan(\lambda)) = \langle DCA_r \rangle_{30\,TFs}(t_i, \tan(\lambda)) - \langle DCA_r \rangle_{40\,s}(t_i, \tan(\lambda)) \,. \quad (4.30)$$

To tune the DCAs of the analytical models DCA_j to the observed DCAs in data as a function of time and tan(λ), the parameters c_j are extracted every 30 TFs for each sampled time interval t_i of the data by a ten-dimensional linear parameterization according to the relation:

$$\langle \Delta DCA_r \rangle_{30\,TFs}(t_i, \tan(\lambda)) = c_0(t_i) \cdot DCA_0(\tan(\lambda)) + \cdots + c_9(t_i) \cdot DCA_9(\tan(\lambda)) \,. \quad (4.31)$$

Figure 4.34b shows the combined DCAs from the scaled analytical models $DCA_{r,sim}$ according to Equation 4.31 yielding qualitatively similar results as the DCAs in data. Figure 4.35a shows the combined boundary potentials as a function of the time and the z-position on the color axis, obtained by scaling the input boundary potentials shown in Figure 4.33a with the parameters c_j from the linear parameterizations. The global scaling parameter S for the combined boundary potentials is found to be 2.5 to accurately

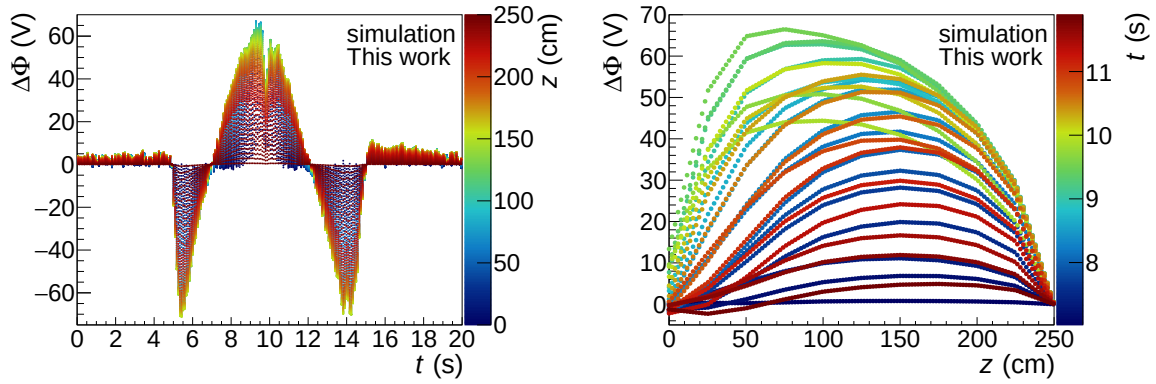

(a) (b)

Figure 4.35: Analytical boundary potentials used to model the M-shape distortions in data (a) for a selected time window as a function of time and the z-position and (b) for 7 s $< t <$ 12 s as a function of the z-position and time.

describe the M-shape distortions in data. Figure 4.35b shows, similar to Figure 4.35a, the boundary potentials as a function of the z-position and the time on the color axis for the time interval 7 s $< t <$ 12 s. The maximum of the boundary potential moves in the z-direction toward the central electrode with increasing time until about 9.5 s, and then the maximum moves back toward the readout. This behavior is presumably driven by the position of the bubble in the cooling system.

The correction objects for the M-shape distortions are stored in the CCDB and contain only the combined boundary potentials according to Equation 4.29. These correction objects are created for the full 2023 data by performing the extraction method described above in an offline procedure. During the reconstruction of the tracks in O^2, the boundary potentials are loaded from the CCDB and used to create on-the-fly the corresponding space-point correction map M_{MShape} for each processed TF using the software framework described in Section 4.1. The final correction map is composed by extending the space-point distortion correction procedure specified in Equation 4.23 to:

$$M(t) = M_{\mathrm{avg}} + M_{\Delta} \cdot \left(\frac{\sum_{t_{\mathrm{sc}}=t_{\mathrm{c}}}^{t} w(t_{\mathrm{sc}} - t, z) \cdot I_{\mathrm{S}}(t_{\mathrm{sc}})}{\sum_{t_{\mathrm{sc}}=t_{\mathrm{c}}}^{t} w(t_{\mathrm{sc}} - t, z)} - \langle I_{\mathrm{S,avg}} \rangle \right) + M_{\mathrm{MShape}}(t) \,. \quad (4.32)$$

Figure 4.36a shows the DCAs from a local reconstruction of the data for one run, overlaid for 43 time windows in which an M-shape distortion occurs, as a function of the relative time t_{M} of each M-shape distortion. To subtract the baseline, the DCAs are averaged over 100 TFs due to the limited amount of data in the local reconstruction compared to the previously shown DCAs. Figure 4.36b shows for the same time

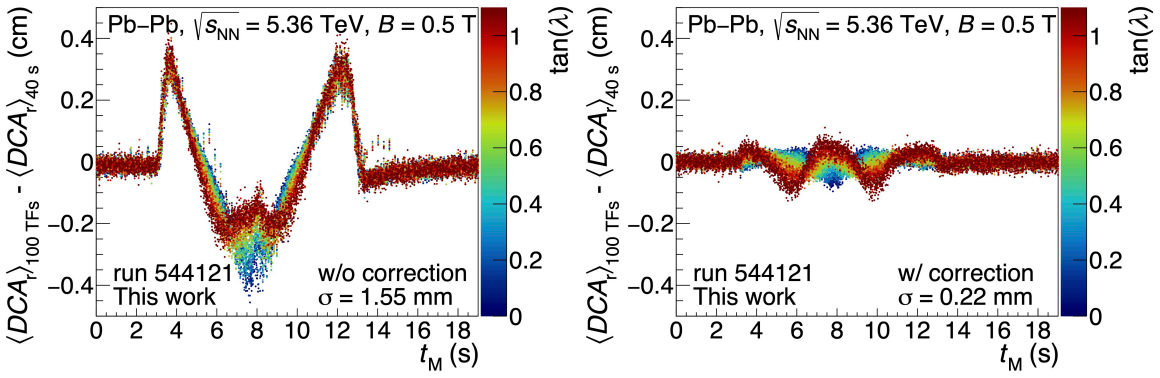

(a) (b)

Figure 4.36: DCAs (a) without and (b) with the correction of several M-shape distortions as a function of the relative time at which the M-shape distortion occurs. The width σ of the DCA distribution is indicated in the figures.

intervals as in Figure 4.36a the DCAs after the M-shape distortions are corrected for in the track reconstruction. While most of the DCA biases due to the M-shape distortions are corrected, a residual bias of approximately ±0.5 mm remains compared to the time intervals without M-shape distortions. The widths of the DCAs, as indicated in the figures, are significantly reduced from 1.55 mm to 0.22 mm with the correction for the M-shape distortions.

The developed correction for the M-shape distortions is automatically applied in the reconstruction of the data by the ALICE collaboration to improve the tracking performance for the time intervals in which the M-shape distortions occur. To avoid the occurrence of the M-shape distortions during data taking from 2024 onwards, the cooling water was removed from the cooling system. The expected temperature increase near the inner field cage, which leads to variations in the electron and ion drift velocities, is considered non-critical.

5 Specific energy loss calibration

Excellent particle identification with the TPC is achieved by combining the reconstructed specific energy loss with the momentum of the particles as described in Section 3.7.5. For optimal particle identification capabilities, the calibration of the measured cluster charges Q_{tot} and Q_{max} is crucial for calculating the specific energy loss. In the following sections, two important corrections for the measured cluster charges and a method to create time-dependent bad channel maps are described.

5.1 Correction of cluster charge dependencies

The measured cluster charges Q_{tot} and Q_{max} depend on several properties, such as the size of the readout pads, the local track inclination angle $\sin(\varphi)$, the dip angle $\tan(\theta)$, the zero-suppression, the time response function of the readout electronics and the gas composition which determines diffusion and electron attachment.

Pad length and local track angles

Figures 5.1a and 5.1b show the track dip angle θ and the local track inclination angle φ for a particle track. The length of the particle trajectory L over a pad and thus the number of projected electrons on a pad depends directly on the local track angles and the pad length l_{pad} according to:

$$L(l_{\mathrm{pad}}, \theta, \varphi) = l_{\mathrm{pad}} \sqrt{\tan(\theta)^2 + \tan(\varphi)^2 + 1}\,. \tag{5.1}$$

However, Equation 5.1 holds only true as long as all electrons are projected on the same pad, which is for example not the case if the track crosses another pad as illustrated in Figure 5.1b for the particle track shown as a dashed line.

Relative pad and time position and time response function

Figures 5.1c and 5.1d show the relative pad position $y_{\mathrm{rel.pad}}$ and the relative time position $t_{\mathrm{rel.time}}$ of a particle track, which are determined in data by the cluster position as described in Section 3.7.1. The electron cloud is indicated in Figure 5.1c as a blue Gaussian curve. Due to diffusion, a part of the electron cloud is measured on neighboring pads, reducing the maximum cluster charge. The time response function of the readout electronics sampled at a frequency of 5 MHz is shown as a blue line in Figure 5.1d. Due to the shaping and sampling of the signal, the maximum cluster charge depends on the

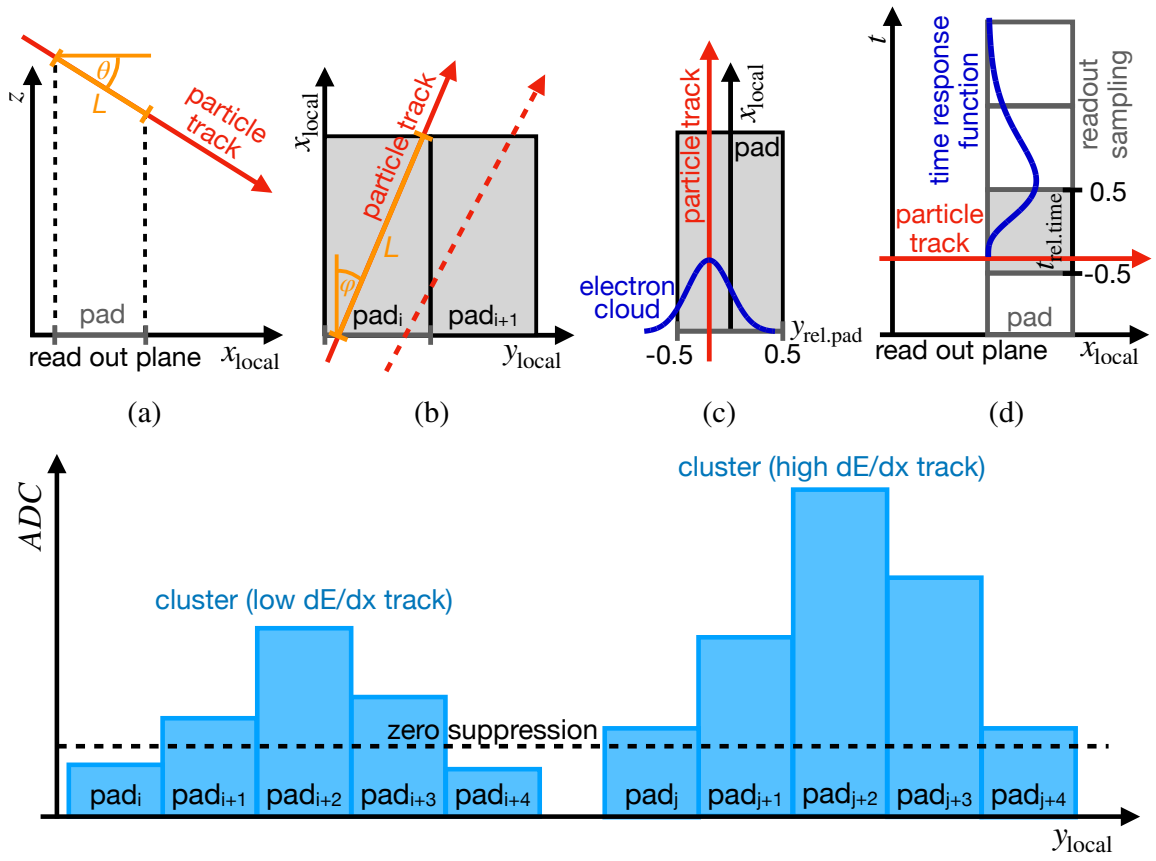

Figure 5.1: Local track angles (a) θ and (b) φ of a track. Relative (c) pad position and (d) time position of a track. (e) Digits for two clusters from a track with low energy loss (left) and high energy loss (right).

relative time of the track to the signal sampling. The total cluster charge is less affected than the maximum cluster charge since neighboring pads and time bins contribute to the total cluster charge.

Zero suppression

In Figure 5.1e, the impact of the zero suppression on the total cluster charge is shown: The cluster on the left-hand side corresponds to a particle track with rather low energy loss, for which the digits on the pads i and $i+4$ fall below the zero suppression threshold and thus do not contribute to the total cluster charge. The cluster on the right-hand side corresponds to a particle track with rather high energy loss. As a result, all digits are above the zero suppression threshold and thus contribute to the total cluster charge. The maximum cluster charge remains unaffected by the zero suppression since the highest digit of a cluster lies by definition above the zero suppression threshold.

5.1.1 Extraction procedure

In Run 2, an analytical approach was used to correct the cluster charges for some of the previously described effects [59]. For a more accurate estimate of the cluster charge dependencies in Run 3, a machine-learning approach is used. The machine learning approach for extracting a correction for the cluster charge dependencies consists of three steps: data generation, training of a neural network and conversion of the trained neural network into fast n-dimensional piecewise polynomials used during the reconstruction. The data generation is performed in the following three steps:

1. Simulation of particle tracks: The electrons from ionization processes of single high p_{T} tracks with random inclination and dip angle and random energy loss are generated to cover the whole phase space. Figure 5.2 shows as an example a few generated tracks as red lines in one sector. Overlapping tracks are avoided in the simulation by separating the tracks in the z-direction.

2. Digitization: The electrons are propagated through the drift volume of the TPC with the procedure described in Section 4.1.1. The generated digits for the tracks in Figure 5.2 are shown on the pad plane. For all digits from each track, a random zero suppression in the range of two to five is applied.

3. Clusterization: The clusterization of the digits is performed with the implementation provided in O^2, yielding the cluster charges Q_{tot} and Q_{max}.

A deep neural network [79] is chosen to parameterize the simulated cluster charges Q_{tot} and Q_{max}, using the Keras package [80]. For the parameterization of Q_{tot} and Q_{max}, the z-position of the drift electron, the local track angles $\sin(\varphi)$ and $\tan(\theta)$ and the pad region R, to account for the different pad sizes, are chosen as parameters. Since Q_{tot} also depends on the zero suppression, the energy loss $\mathrm{d}E/\mathrm{d}x_{\mathrm{in}}$ used to generate the track and the value of the zero suppression Z are used as additional parameters:

$$\frac{Q_{\mathrm{tot}}}{\mathrm{d}E/\mathrm{d}x_{\mathrm{in}}}\left(z, \tan(\theta), \sin(\varphi), Z, \mathrm{d}E/\mathrm{d}x_{\mathrm{in}}, R\right). \tag{5.2}$$

For Q_{max}, the relative pad and the relative time position of the tracks are used as additional parameters:

$$\frac{Q_{\mathrm{max}}}{\mathrm{d}E/\mathrm{d}x_{\mathrm{in}}}\left(z, \tan(\theta), \sin(\varphi), y_{\mathrm{rel.pad}}, t_{\mathrm{rel.time}}, R\right). \tag{5.3}$$

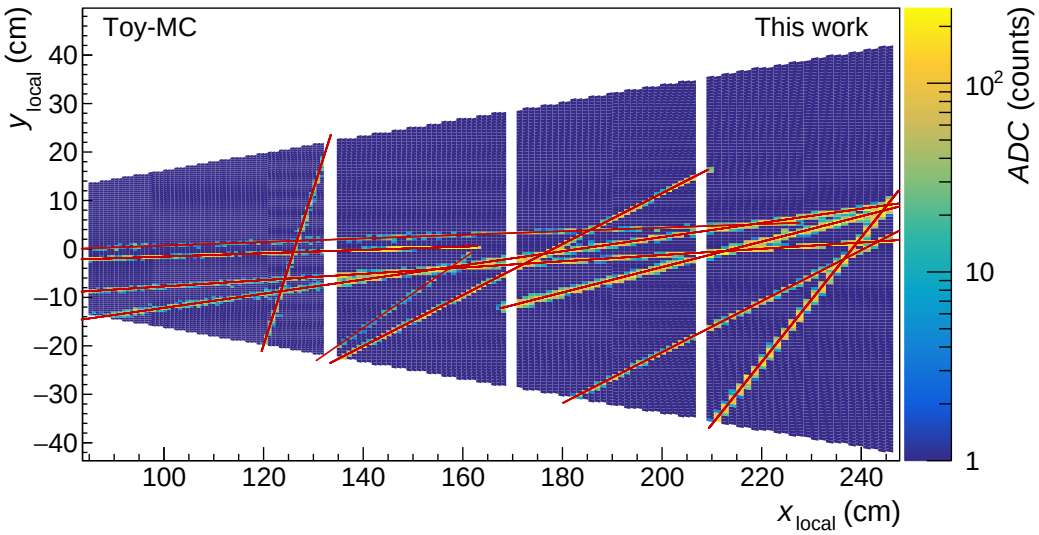

Figure 5.2: Simulated digits for high p_T tracks, shown as red lines. The tracks are separated in time to avoid overlapping digits between tracks.

In order to use the trained neural network during the synchronous reconstruction to correct the cluster charges, a fast method with GPU support for evaluating the trained network is required. To meet these requirements, piecewise five-dimensional polynomials [81] of third-degree are used to parameterize the trained network for each pad region as a fast method for querying the corrections.

An n-dimensional polynomial p of m-th degree with real-valued coefficients α_κ can be written in multi-index notation with the general expression [82]:

$$p_n^m = \sum_{|\kappa| \leq m} \alpha_\kappa \prod_{i=1}^{n} x_i^{\kappa_i} \ , \tag{5.4}$$

where κ is a non-negative integer: $\kappa \in \mathbb{N}, \kappa \leq n$ and $|\kappa| = \kappa_1 + \cdots + \kappa_n$.

This gives the expression for five-dimensional polynomials of third degree:

$$p_5^3 = \sum_{\kappa_1=0}^{3} \sum_{\kappa_2=0}^{3} \sum_{\kappa_3=0}^{3} \sum_{\kappa_4=0}^{3} \sum_{\kappa_5=0}^{3} \alpha_{\kappa_1\kappa_2\kappa_3\kappa_4\kappa_5} x_1^{\kappa_1} x_2^{\kappa_2} x_3^{\kappa_3} x_4^{\kappa_4} x_5^{\kappa_5} \text{ with: } |\kappa| \leq 3 \ . \tag{5.5}$$

For optimal performance during the track reconstruction when evaluating the polynomials, the full expression of Equation 5.5 is expanded at compile time of O^2. The trained neural networks are converted to twenty piecewise polynomials P_5^3 by evaluating the trained models on a grid and afterward parameterizing the predictions of the neural

network by the piecewise polynomials. For the total cluster charge, $\mathrm{d}E/\mathrm{d}x_{\mathrm{in}}$ is converted to the mean measured cluster charge $\langle Q_{\mathrm{tot}} \rangle$ in the given region by multiplying $\mathrm{d}E/\mathrm{d}x_{\mathrm{in}}$ with the prediction $\left\langle \frac{Q_{\mathrm{tot}}}{\mathrm{d}E/\mathrm{d}x_{\mathrm{in}}} \right\rangle$ of the trained network since $\mathrm{d}E/\mathrm{d}x_{\mathrm{in}}$ cannot be measured directly. This leads to corrections for the maximum and total cluster charge of the form:

$$C_{\mathrm{Q_{tot},R}}\left(z, \tan(\theta), \sin(\varphi), Z, \langle Q_{\mathrm{tot}} \rangle\right) = 1/P^3_{5,\mathrm{Q_{tot},R}} \ , \tag{5.6a}$$

$$C_{\mathrm{Q_{max},R}}\left(z, \tan(\theta), \sin(\varphi), y_{\mathrm{rel.pad}}, t_{\mathrm{rel.time}}\right) = 1/P^3_{5,\mathrm{Q_{max},R}} \ . \tag{5.6b}$$

The coefficients α_κ of the polynomials are stored in the CCDB and they are automatically loaded during the synchronous and asynchronous reconstruction for the correction of the cluster charges when calculating the specific energy loss according to:

$$\mathrm{d}E/\mathrm{d}x_{(\mathrm{tot,max})} = \frac{1}{0.6 \cdot n_{\mathrm{cl}} - 0.015 \cdot n_{\mathrm{cl}}} \sum_{i=0.015 \cdot n_{\mathrm{cl}}}^{0.6 \cdot n_{\mathrm{cl}}} C_{\mathrm{Q_{(tot,max)},R}} \cdot Q_{(\mathrm{tot,max}),i} \ . \tag{5.7}$$

Figure 5.3 shows as examples slices of the piecewise polynomials that are used to correct the cluster charges for the first pad region. Figure 5.3a shows the correction for the maximum cluster charge as a function of the relative pad and time position. As expected, the correction gets larger for clusters that are created by tracks closer to the edges of the pads or time bins. The asymmetry of the correction in the time direction is produced by the long tail of the time response function. Figure 5.3b shows the correction for the maximum cluster charge as a function of the z-position of the drift electron and the relative time position. Due to larger diffusion and higher electron attachment for longer drift distances, fewer electrons contribute to the maximum cluster charge, leading to larger correction values. Figure 5.3c shows the correction for the total cluster charge as a function of the total cluster charge and the zero suppression threshold. Toward low total cluster charges and high zero suppression, more digits of the clusters fall below the zero suppression threshold and therefore do not contribute to the total cluster charge, leading to larger correction values. Figure 5.3d shows the correction for the total cluster charge as a function of the z-position of the drift electron and the local track dip angle $\tan(\theta)$. Toward high track dip angles and small drift distances, more electrons contribute to the total cluster charge leading to smaller correction values. The increase in the corrections for very small drift distances and small dip angles is probably caused by edge effects.
The performance of the reconstructed specific energy loss with and without the correction for the cluster charges is shown for data in Figure 5.4 for rather long particle tracks with

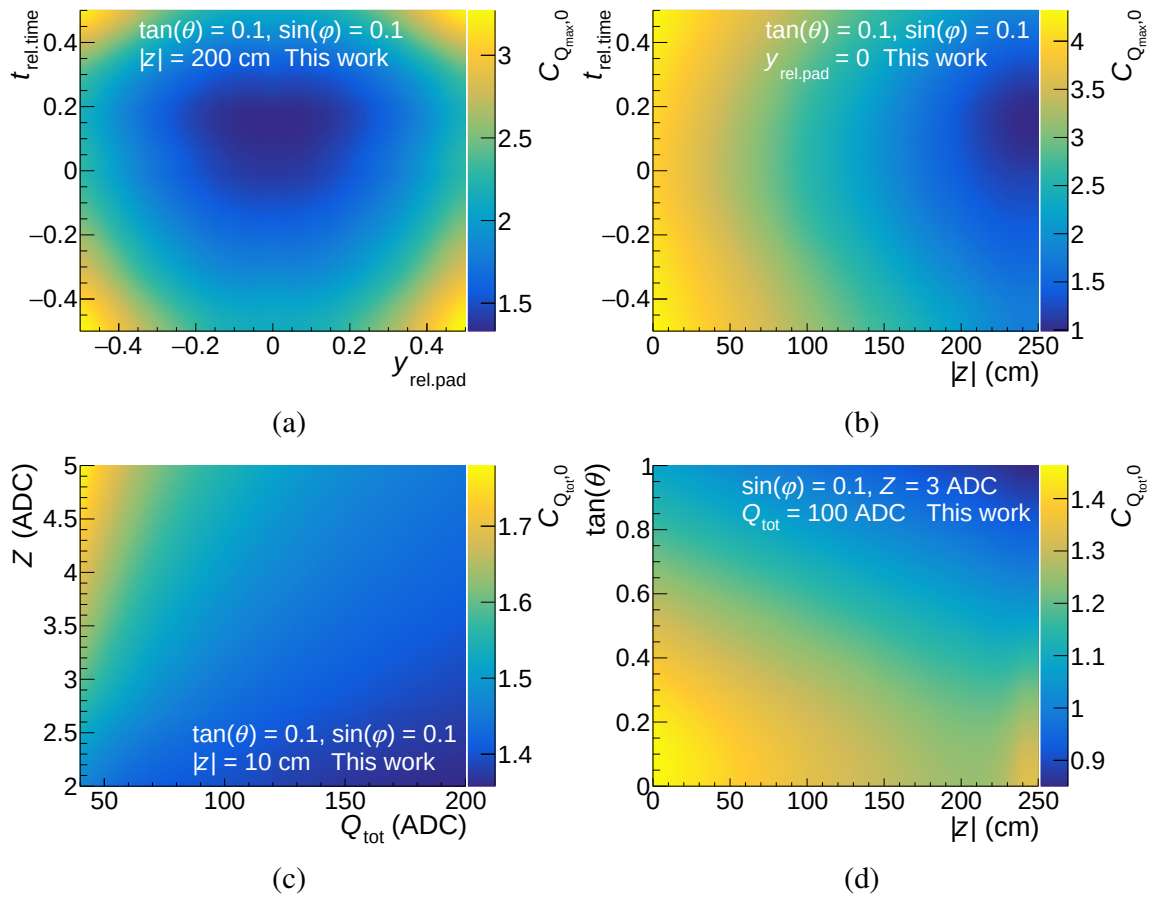

Figure 5.3: Slice of the correction for Q_{max} as a function of (a) the relative pad position $y_{\mathrm{rel.pad}}$ and relative time position $t_{\mathrm{rel.time}}$ and (b) the z-position of the drift electron and the relative time. Slice of the correction for Q_{tot} as a function of (c) the total cluster charge and the zero suppression threshold Z and (d) the z-position of the drift electron and the track dip angle $\tan(\theta)$.

more than 120 clusters which are matched to the ITS. The correction for time-dependent gain variations described in Section 3.7.6 is not applied. Figures 5.4a and 5.4b show the reconstructed specific energy loss for the maximum cluster charge and the total cluster charge, respectively, as a function of the particle's momentum without the correction for the cluster charges described above. Similarly, Figures 5.4c and 5.4d show the reconstructed specific energy loss after applying the correction for the maximum and total cluster charge, which leads to significant improvements in particle identification, as implied by the better separation of the particle bands. The red lines in Figure 5.4d show a parameterization by a Bethe-Bloch function, which is extracted by TPC experts in the post-processing of the reconstructed data. Since only the specific energy loss for the total cluster charge is stored in the final reconstruction data used for physics analysis,

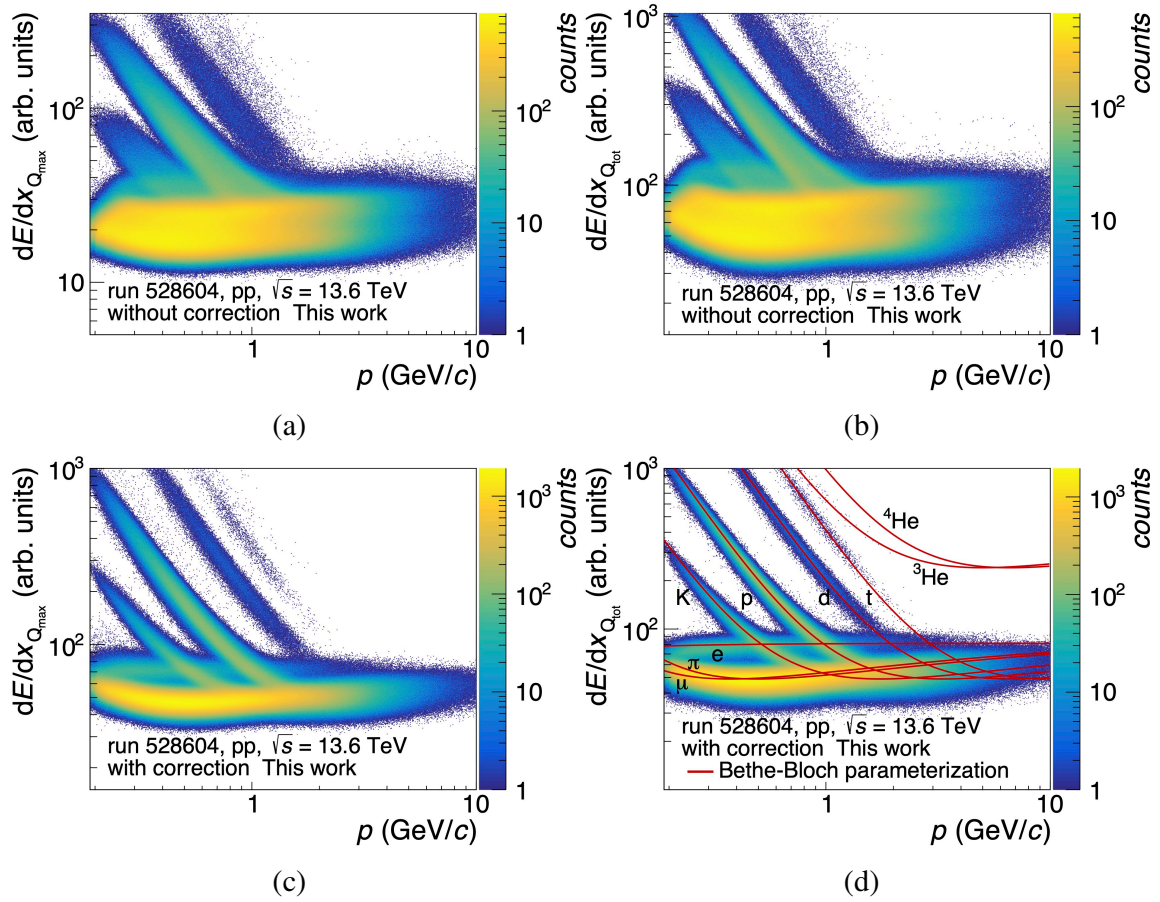

Figure 5.4: Reconstructed specific energy loss as a function of the particle's momentum without the correction for (a) the maximum cluster charge and (b) the total cluster charge and with the correction for (c) the maximum cluster charge and (d) the total cluster charge.

a similar parameterization for the maximum cluster charge is not extracted by the TPC experts and is therefore not shown. Figures 5.5a and 5.5b show the reconstructed specific energy loss normalized to the mean energy loss of pions for particles with momenta in the range of $0.4\,\mathrm{GeV}/c < p < 0.6\,\mathrm{GeV}/c$. The normalized reconstructed specific energy loss is shown in red without the correction and in blue with the correction. For the maximum cluster charge, the separation power between pions and electrons reaches 3.2 with the correction. The relative resolution reaches 8% for pions and 15% for electrons. For the total cluster charge, the separation power improves compared to the maximum cluster charge, reaching 4.4 with the correction. The relative resolution reaches 9% for pions and 13% for electrons. The separation between pions and electrons is only possible after applying the developed correction.

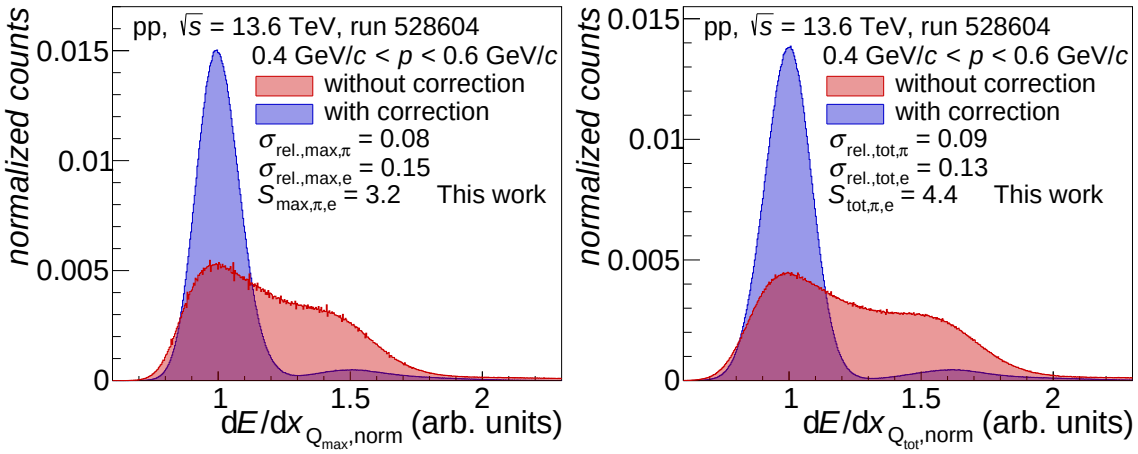

(a) (b)

Figure 5.5: Reconstructed specific energy loss normalized to the mean energy loss of pions with and without the correction for (a) the maximum cluster charge and (b) the total cluster charge.

5.2 Correction of residual gain variations

The extraction of the gain map with the procedure described in Section 3.7.6 requires the release of radioactive krypton into the TPC and is therefore typically performed only once at the end of the year during the winter maintenance break of the LHC. To allow for the extraction of a gain map during data acquisition, a dedicated procedure using particle tracks is developed and carried out during the synchronous reconstruction in the following four steps:

1. On the EPNs, the maximum cluster charges of all reconstructed tracks are corrected by the krypton pad-by-pad gain map and the correction described in Section 5.1. Afterward, the corrected cluster charges are normalized to the mean energy loss of the corresponding track. The normalized cluster charges are stored in pad-by-pad histograms and sent to a calibration node.

2. The pad-by-pad histograms with the normalized cluster charges $Q_{\mathrm{max,norm}}$ for all EPNs are collected and merged on a calibration node.

3. Once sufficient data has been collected for each pad, the truncated mean with an upper truncation range of 40% of the normalized cluster charges $Q_{\mathrm{max,norm}}$ is calculated for each pad as an estimate of the relative gain. As an example, Figure 5.6 shows for one pad the normalized cluster charges with the truncated mean as a black line.

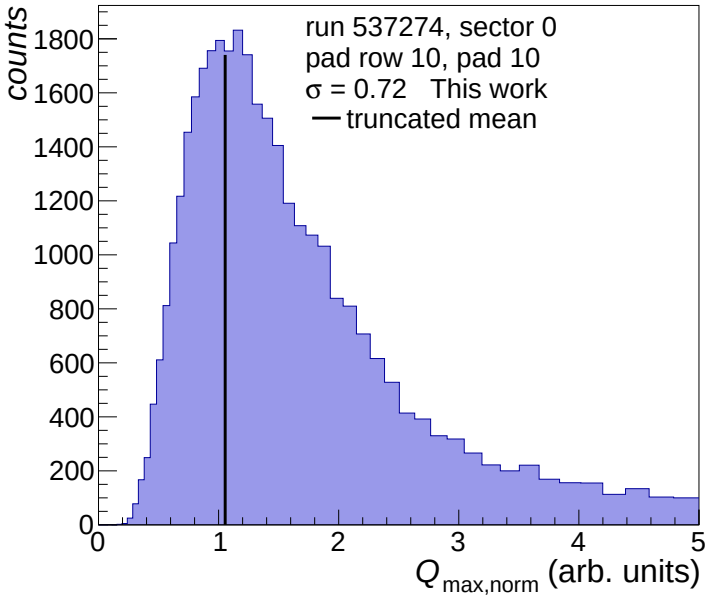

Figure 5.6: Maximum cluster charge normalized to the reconstructed energy loss of the track $Q_{\mathrm{max,norm}}$ for one readout pad.

4. The extracted relative gain per pad is normalized to the average relative gain per GEM stack, resulting in pad-by-pad gain maps which are stored in the CCDB. In addition, the standard deviations of each pad-by-pad histogram are calculated as a measure of the resolution for each pad, which is given in Figure 5.6 by $\sigma = 0.72$.

Figure 5.7 shows the results of this procedure: Figures 5.7a and 5.7b show the extracted relative pad-by-pad gain maps for the A-side and C-side, respectively. Large residual gain variations of about 20% occur in the region of the spacer crosses and in the first and last pad rows of a GEM stack, where the krypton method is not reliable [53]. In addition, rather large residual gain structures occur in some readout chambers, such as in sector four on the A-side. The horizontal lines of high gain in the IROCs are presumably noise induced by the temperature sensor cables. These pad-by-pad gain maps can be used during the calculation of the specific energy loss to correct for residual gain variations not corrected by the static krypton gain map by normalizing the cluster charges to the corresponding residual gain. Figures 5.7c and 5.7d show, as an estimate of the resolution of the measured gain, the pad-by-pad maps of the standard deviations normalized to the residual gain for the A-side and C-side, respectively. The resolution worsens with decreasing pad size due to the larger statistical fluctuations. In the regions of the spacer crosses, the resolution is significantly lower than for the surrounding pads, suggesting that these pads should be excluded when calculating the specific energy loss.

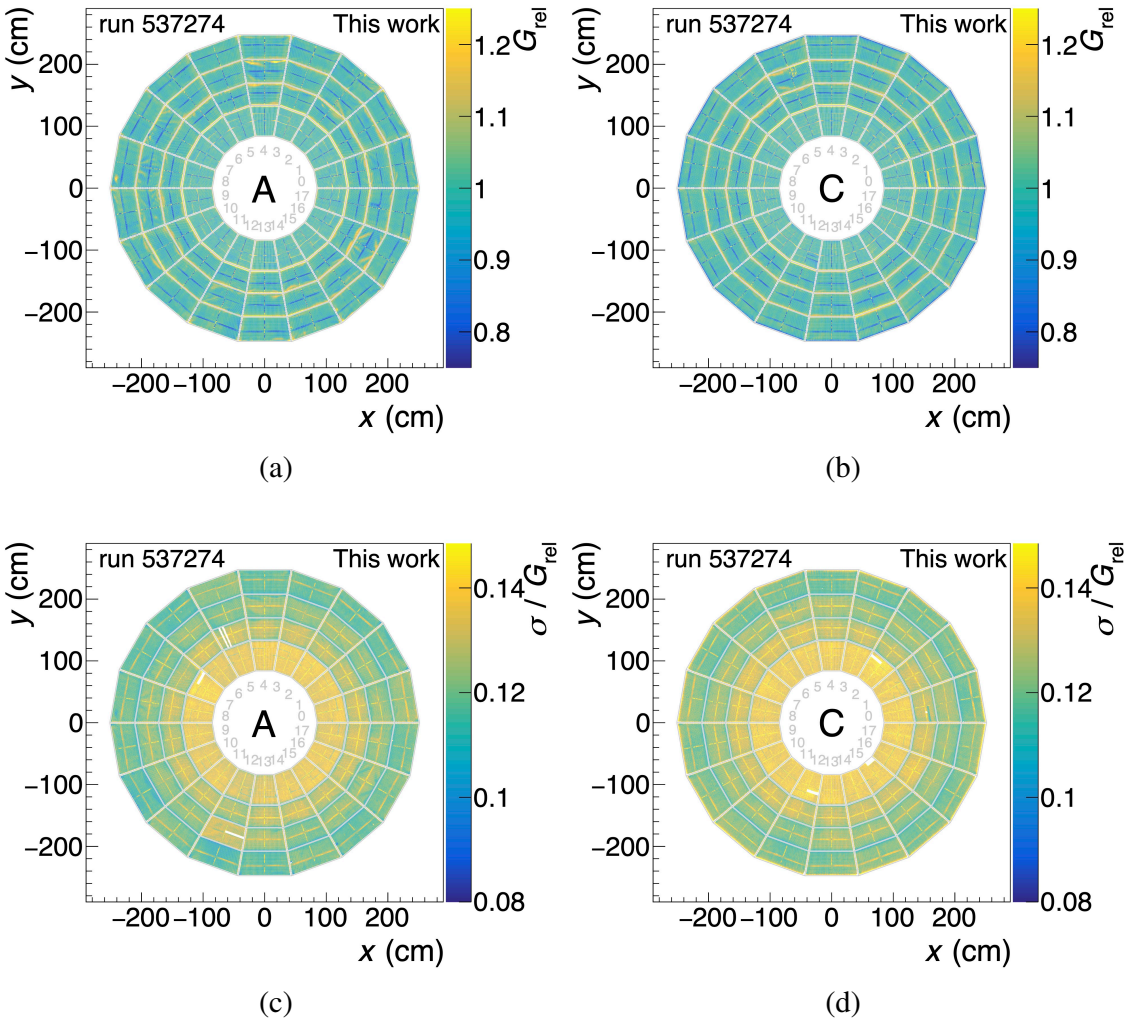

Figure 5.7: Residual pad-by-pad gain map for the (a) A-side and the (b) C-side. Pad-by-pad map of the resolution of the extracted relative gain for the (c) A-side and (d) C-side.

5.3 Time-dependent bad channel maps

Until mid-2023, the readout electronics of the TPC suffered from time- and rate-dependent acceptance losses, presumably caused by radiation-induced malfunctions in the FECs. Figure 5.8a shows for several pp runs with various interaction rates the acceptance losses for the C-side due to bad readout channels as a function of time since the start of each run t_{run}. The acceptance loss is defined by the ratio of bad channels $N_{\text{pads lost}}$ to the number of total readout channels $N_{\text{pads total}}$. The color axis shows the average IDC value of each run, which is used as a proxy of the interaction rate respectively the radiation exposed to the FECs. The jumps in bad channels for some time intervals correspond to trips of a GEM, where a full readout chamber is

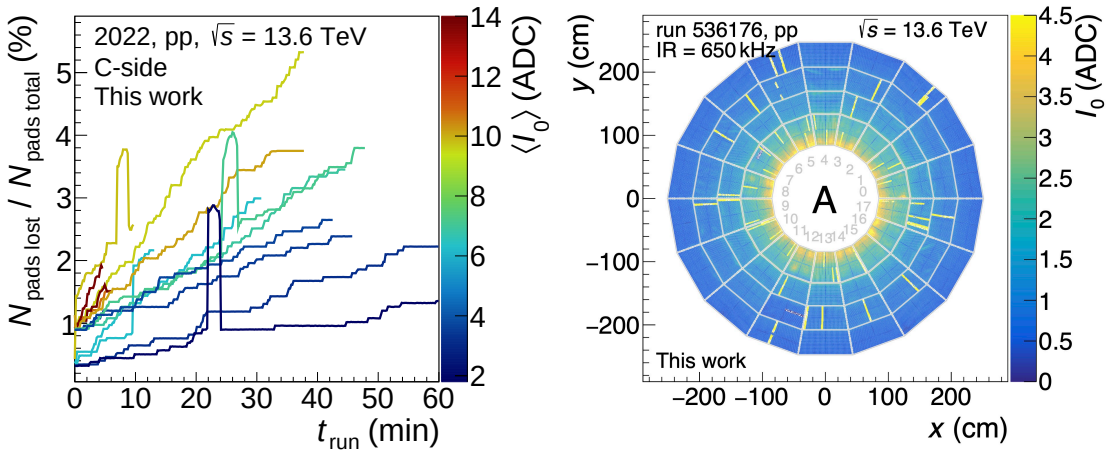

(a) (b)

Figure 5.8: (a) Acceptance loss, defined as the ratio of bad channels $N_{\text{pads lost}}$ to the number of total readout channels $N_{\text{pads total}}$, as a function of the time since the start of the run for the C-side for pp runs with interaction rates ranging from 650 kHz to 7 MHz. (b) I_0 for the A-side close to the end of a run.

automatically deactivated for some time until the GEM voltages are ramped up again. The number of bad readout channels increases constantly as a function of time due to the radiation-induced malfunctions in the FECs. Also, a clear increase of bad readout channels with the interaction rates occurs, due to the increase in radiation.

Figure 5.8b shows as an example I_0 for the A-side close to the end of a run where several FECs delivered faulty signals, leading to high values in the IDCs. During the reconstruction of the TPC tracks, the missing readout signals for these FECs can lead to the splitting or shortening of tracks when a particle traverses these problematic pad regions as the track following is aborted in case no clusters are found for a given amount of consecutive pad rows. This shortening leads to a lower number of clusters associated with the track, which reduces the resolution of the energy loss and worsens the momentum resolution. Figure 5.9a shows the pads that are flagged as bad by an automatic tagging procedure. In this procedure, the I_0 for each pad is normalized to the median I_0 of the corresponding GEM stack. If the normalized I_0 is outside the range of 15 standard deviations from the values of the same pad row, the channel is flagged as bad. These time-dependent bad channel maps are generated during the online processing of the IDCs in ten-second intervals after the I_0 maps are created. The bad channel maps are stored in the CCDB and they are used in the track reconstruction to avoid aborting the track following if the extrapolated track leads to a readout pad that has been identified as bad. Figure 5.9b shows the ratio of the number of clusters

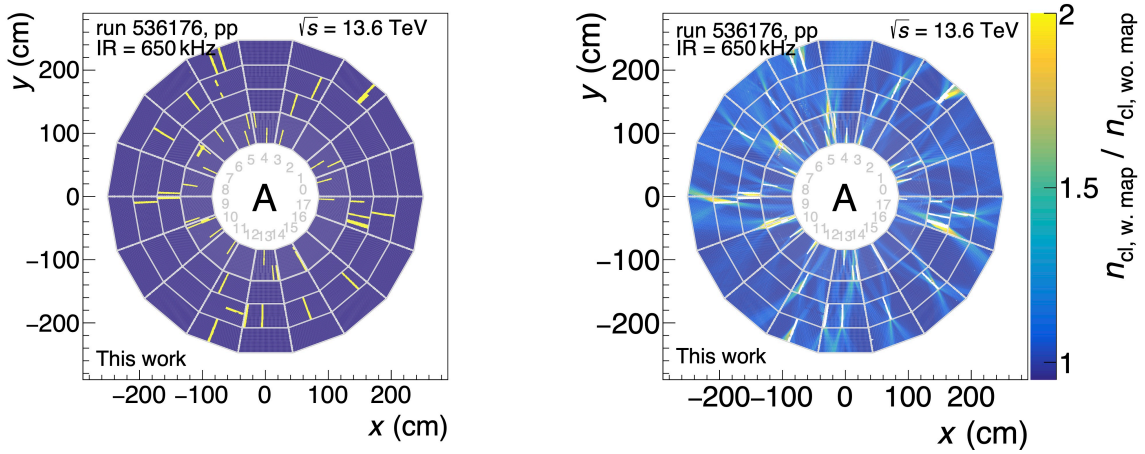

(a) (b)

Figure 5.9: (a) Readout pads which are flagged as bad. (b) Ratio of the number of clusters associated with tracks by using the bad channel maps in the reconstruction to the number of clusters associated with tracks without using the bad channel maps.

associated with TPC tracks by using the bad channel maps in the reconstruction to the number of clusters associated with tracks without using the bad channel maps. In the vicinity of the malfunctioning FECs, the number of clusters associated with tracks is significantly increased by up to two to three when using the bad channel maps.

In addition to the use of these bad channel maps during the reconstruction of real data, they are used in MC simulations to follow the acceptance losses by deactivating the flagged readout pads.

6 Summary

The major upgrade of the ALICE TPC and the newly written reconstruction and simulation framework O^2 enable continuous data acquisition for LHC Run 3. For the upgrade of the TPC, the Multi-Wire Proportional Chambers used in Run 1 and Run 2 for the electron amplification were replaced by stacks of four GEM foils. Due to the properties of the GEM foils, a residual amount of ions, produced during the amplification stage, enters the drift volume of the TPC. Ions from several consecutive collisions are considered as compressed space-charge disks drifting constantly to the central electrode. These space-charge disks cause, due to their positive charge, time- and position-dependent distortions of the drift field, which lead to distortions of the reconstructed space points, called space-charge distortions. In addition, the LHC beam behavior and short-term fluctuations of the order of milliseconds, for example due to event-by-event multiplicity variations, cause significant time-dependent changes in the space-charge distortions, which need to be corrected to preserve the intrinsic resolution of the TPC.
In the scope of this work, the software framework for analytically calculating space-point distortions is ported from the old software framework AliRoot to O^2. Improvements are achieved by significantly increasing the performance by using modern C++, multi-threading, and generally improving the usability by providing flexible and user-friendly interfaces for the calculation of the space-point distortions. This framework can be used to calculate the space-point distortions due to space charge and other sources such as the misalignment between the magnetic field and the electric field or charging of the GEM frames.
Within this thesis, the expected space-charge density for 50 kHz Pb–Pb collisions, simulated using the Pythia event generator, is shown. The resulting analytical models of the space-charge distortions reach up to ten centimeters in the radial direction. These models are used to analyze space-point distortions caused by the charging of the inner field cage vessel on the C-side. By fitting an analytical model to the observed space-point distortions in data for several runs with various interaction rates, the increase of these distortions with the interaction rate and the dependence on the magnetic field is shown.
In addition to simulations, correction procedures for the space-charge distortions and the space-charge distortion fluctuations are developed and implemented in O^2 in the scope of this work. For these correction procedures, the IDCs, i.e. the measured digits on the readout pads integrated over about one millisecond, are used as the main source to approximate the space-charge density in the TPC as a function of time. To be able

to use these IDCs in the correction procedures, their online processing and a dedicated compression procedure for storing the IDCs in the CCDB are developed and implemented in O^2: In the first step, the IDCs are averaged in time windows of about ten seconds to obtain an average two-dimensional IDC map. In the second step, the so-called one-dimensional IDCs are created for each millisecond by calculating the average of the IDCs normalized to their long-term average value. These one-dimensional IDCs are used as a proxy for the space-charge density fluctuations and to precisely analyze the LHC beam behavior. By performing the FFT of the one-dimensional IDCs it is found and confirmed by LHC experts that vibrations at frequencies of about six and eleven Hertz of the LHC's inner triplet magnets cause oscillations of the LHC beam for pp collisions, resulting in corresponding oscillations of the space-charge density.
The space-charge density fluctuations in data extracted by the one-dimensional IDCs are compared with MC simulations and the expectation from an analytical formula as a function of the number of ion pile-up events, i.e. the number of particle collisions contributing to the space-charge density from IBF for a given moment in time. The fluctuations from data agree well with the expected fluctuations from the MC simulations and the analytical formula, confirming that the IDCs are suitable as a proxy for the space-charge density fluctuations. The space-charge density fluctuations reach about 1.5% for 50 kHz Pb–Pb collisions, leading to space-charge distortion fluctuations of the order of millimeter in the Pb–Pb data taking. For a precise correction of these fluctuations, the contribution of the space-charge disks to the space-charge distortions with respect to the position of the space-charge disks in time is extracted from data by calculating in time intervals of about 2.8 ms the average distance of closest approach, the DCA, of the extrapolated distorted TPC tracks to the primary vertex. This DCA is used as a precise and robust measure of the space-point distortions as a function of time. By correlating these DCAs with the IDCs, the weights, which give an estimate of how much each space-charge density disk contributes to the space-charge distortions, are extracted with a multidimensional linear parameterization. The ion drift time of about 190 ms measured experimentally in other studies agrees with the results from the extracted weights. For the correction of the space-point distortions, a data-driven approach developed in Run 1 and Run 2 is used to create three-dimensional correction maps by matching the TPC tracks to the corresponding ITS tracks. These reference ITS tracks are extrapolated to the distorted TPC space points. By calculating the residuals between the positions of the extrapolated ITS track and the distorted TPC space points, and further processing, three-dimensional correction maps are created by TPC experts.

These correction maps describe, by construction, only the average space-point distortions for the data used to create the correction map. A second correction map is used to correct the space-charge distortion fluctuations on short timescales of the order of milliseconds and the space-charge distortion variations on long timescales of the order of minutes. This second correction map describes the derivative of the space-point distortions with respect to the IDCs. The derivative correction map is scaled by the IDCs and the weights according to the weighted average of the one-dimensional IDCs and it is linearly combined with the average correction map to produce on-the-fly the final correction map during the reconstruction of the data.
In the analysis of the DCAs, unexpected space-point distortions referred to as M-shape distortions are observed. It is found that these M-shape distortions are presumably caused by a leak in the underpressure cooling system for the resistor rod of the inner field cage on the A-side, leading to air bubbles being drawn into the cooling system. These bubbles could possibly be charged due to the surrounding radiation and thus induce currents in the inner field cage strips. In addition, spikes are observed in the currents of the power supply which is used to define the potential of the field cage strip closest to the readout chambers. These spikes and the charged bubbles might lead to the observed M-shape distortions. For the correction of the M-shape distortions, analytical models that describe the change in potential at the inner field cage strips are tuned to the DCAs in the data. The parameters of the models are stored in the CCDB and are used during the track reconstruction to calculate on-the-fly the required corrections.
In addition to the corrections for the space-point distortions, two procedures for the calibration of the specific energy loss are presented. In the first procedure, the cluster charges Q_{max} and Q_{tot} are corrected to account for their dependence on the track topology and detector geometry, such as pad size. This correction is obtained by simulating the relevant dependencies in a Toy-MC and parameterizing these dependencies with five-dimensional piecewise polynomials. The parameters of the piecewise polynomials are stored in the CCDB and they are automatically used for the correction of the cluster charges during the calculation of the specific energy loss. The second procedure provides an estimate of residual pad-by-pad gain variations that are not corrected by a krypton gain map. This method is based solely on particle tracks and is therefore performed during normal data acquisition.
The presented corrections for the space-point distortions and the specific energy loss, implemented in the scope of this work, are crucial components to ensure precise tracking and particle identification capabilities with the TPC in LHC Run 3.

References

[1] E. Rutherford, "The scattering of α and β particles by matter and the structure of the atom", *Philos. Mag.* 21 no. 125, 669–688, 1911.

[2] C. T. R. Wilson, "On an expansion apparatus for making visible the tracks of ionising particles in gases and some results obtained by its use", *Proc. R. Soc. A.* 87 no. 595, 277–292, 1912.

[3] D. A. Glaser, "Bubble Chamber Tracks of Penetrating Cosmic-Ray Particles", *Phys. Rev.* 91 762, 1953.

[4] A. Rousset, "The discovery of weak neutral currents", *Nucl. Phys. B Proc. Suppl.* 36 339–362, 1994.

[5] D. R. Nygren, "Origin and development of the TPC idea", *Nucl. Instrum. Meth. A* 907 22–30, 2018.

[6] ALICE, "The ALICE experiment - A journey through QCD", *CERN-EP-2022-227*, arXiv:2211.04384, 2022.

[7] ALICE, "The ALICE experiment at the CERN LHC", *J. Instrum.* 3 no. 08, S08002, 2008.

[8] ALICE TPC, "The upgrade of the ALICE TPC with GEMs and continuous readout", *JINST* 16 no. 03, P03022, arXiv:2012.09518 [physics.ins-det], 2021.

[9] ALICE, "Technical Design Report for the Upgrade of the Online-Offline Computing System", *CERN-LHCC-2015-006, ALICE-TDR-019*, 2015.

[10] L. Evans and P. Bryant, "LHC Machine", *JINST* 3 no. 08, S08001, 2008.

[11] R. Pasechnik and M. Šumbera, "Phenomenological Review on Quark-Gluon Plasma: Concepts vs. Observations", *Universe* 3 no. 1, 7, 2017.

[12] F. Noferini, "ALICE results from Run-1 and Run-2 and perspectives for Run-3 and Run-4", *J. Phys. Conf. Ser.* 1014 no. 1, 012010, 2018.

[13] ALICE, "Technical Design Report for the Upgrade of the ALICE Inner Tracking System", *J. Phys. G* 41 087002, 2014.

[14] ALICE, "Technical Design Report of the Time Projection Chamber", *CERN-OPEN-2000-183, CERN-LHCC-2000-001*, 2000.

[15] ALICE, "ALICE technical design report of the time-of-flight system (TOF)", *CERN-LHCC-2000-012*, 2000.

[16] ALICE, "The ALICE Transition Radiation Detector: construction, operation, and performance", *Nucl. Instrum. Meth. A* 881 88–127, arXiv:1709.02743 [physics.ins-det], 2018.

[17] M. Slupecki, "Fast Interaction Trigger for ALICE upgrade", *Nucl. Instrum. Meth. A* 1039 167021, 2022.

[18] A. Tauro, "ALICE Schematics", *Performance figure*, 2017. visited on 16.04.2024.

[19] J. Wenninger, "Operation and Configuration of the LHC in Run 1", *CERN-ACC-NOTE-2013-0041*, 2014.

[20] J. Wenninger, "Operation and Configuration of the LHC in Run 2", *CERN-ACC-NOTE-2019-0007*, 2019.

[21] W. Herr and B. Muratori, "Concept of luminosity", *CERN-2006-002.361*, 2006.

[22] LPC, "LHC Programme Coordination", https://lpc.web.cern.ch, 2023.

[23] CERN, "LHC supertable 2023", https://bpt.web.cern.ch/lhc/supertable/2023, 2024.

[24] S. Fartoukh *et al.*, "LHC Configuration and Operational Scenario for Run 3", *CERN-ACC-2021-0007*, 2021.

[25] ALICE, "AliceO2", https://github.com/AliceO2Group/AliceO2, 2018.

[26] T. Sjöstrand *et al.*, "An introduction to PYTHIA 8.2", *Comput. Phys. Commun.* 191 159–177, 2015.

[27] GEANT4, "Geant4—a simulation toolkit", *Nucl. Instrum. Meth. A* 506 250–303, 2003.

[28] D. Rohr, "Usage of GPUs in ALICE Online and Offline processing during LHC Run 3", *EPJ Web Conf.* 251 04026, arXiv:2106.03636 [physics.ins-det], 2021.

[29] ALICE, "Upgrade of the ALICE Time Projection Chamber", *CERN-LHCC-2013-020, ALICE-TDR-016*, 2014.

[30] L. Rolandi, W. Riegler and W. Blum, "Particle Detection with Drift Chambers", *Particle Acceleration and Detection*, 2008.

[31] Particle Data Group, "Review of Particle Physics", *PTEP* 083C01, 2022.

[32] N. Bohr, "On the theory of the decrease of velocity of moving electrified particles on passing through matter", *Philos. Mag.* 25 10–31, 1913.

[33] H. Bethe, "Zur Theorie des Durchgangs schneller Korpuskularstrahlen durch Materie", *Annalen der Physik* 397 325–400, 1930.

[34] F. Bloch, "Zur Bremsung rasch bewegter Teilchen beim Durchgang durch Materie", *Annalen der Physik* 408 285–320, 1933.

[35] E. Fermi, "The Ionization Loss of Energy in Gases and in Condensed Materials", *Phys. Rev.* 57 485–493, 1940.

[36] H. Kolanoski and N. Wermes, "Teilchendetektoren", 2016.

[37] J. Lindhard and A. H. Sorensen, "Relativistic theory of stopping for heavy ions", *Phys. Rev. A* 53 2443–2456, 1996.

[38] H. H. Andersen and J. F. Ziegler, "Hydrogen Stopping powers and ranges in all elements", 1977.

[39] J. Lindhard, M. Scharff and H. E. Schioett, "Range Concepts and Heavy Ion Ranges", *Kgl. Danske Videnskab. Selskab. Mat. Fys. Medd.* 33 no. 14, 1963.

[40] L. D. Landau, "On the energy loss of fast particles by ionization", *J. Phys.* 8 201–205, 1944.

[41] National Institute of Standards and Technology, "XCOM: Photon Cross Sections Database", `https://physics.nist.gov`, 2023.

[42] National Institute for Fusion Science, "Oscillator Strength Spectra and Related Quantities of 9 Atoms and 23 Molecules Over the Entire Energy Region", 2010.

[43] ALICE, "Direct photon production at low transverse momentum in proton-proton collisions at $\sqrt{s}$ = 2.76 and 8 TeV", *Phys. Rev. C* 99 no. 2, 024912, arXiv:1803.09857 [nucl-ex], 2019.

[44] M. Mager, S. Rossegger and J. Thomas, "The Langevin Equation expanded to 2nd order and comments on using the equation to correct for space point distortions in a TPC", *ALICE-INT-2010-016*, 2010.

[45] R. Veenhof, "Garfield - simulation of gaseous detectors", https://garfield.web.cern.ch, 2010.

[46] R. Veenhof, "Magboltz - transport of electrons in gas mixtures", https://magboltz.web.cern.ch, 2024.

[47] A. Deisting, "Measurements of ion mobility and GEM discharge studies for the upgrade of the ALICE time projection chamber", *CERN-THESIS-2018-014*, 2018.

[48] M. Jung, "Ageing tests with Gas Electron Multipliers for the ALICE TPC Upgrade", *master thesis*, 2021.

[49] M. Jung, personal communication, 2023.

[50] S. Duarte Pinto *et al.*, "Progress on large area GEMs", *JINST* 4 no. 12, P12009, arXiv:0909.5039 [physics.ins-det], 2009.

[51] F. Sauli, "The gas electron multiplier (GEM): Operating principles and applications", *Nucl. Instrum. Methods Phys. Res., Sect. A.* 805 2–24, 2016.

[52] S. Pommé, H. Stroh and R. Van Ammel, "The ^{55}Fe half-life measured with a pressurised proportional counter", *Appl. Radiat. Isot.* 148 no. 12, 27–34, 2019.

[53] P. Hauer, "Gain Calibration of the Upgraded ALICE TPC", *CERN-THESIS-2022-253*, 2022.

[54] ALICE, "The ALICE TPC, a large 3-dimensional tracking device with fast readout for ultra-high multiplicity events", *Nucl. Instrum. Meth. A* 622 316–367, arXiv:1001.1950 [physics.ins-det], 2010.

[55] F. Weiglhofer, "Optimierung des Cluster Finders auf GPUs im TPC-Detektor bei ALICE", *master thesis*, 2022.

[56] D. Rohr, S. Gorbunov and V. Lindenstruth, "GPU-accelerated track reconstruction in the ALICE High Level Trigger", *J. Phys. Conf. Ser.* 898 no. 3, 032030, arXiv:1712.09430 [physics.ins-det], 2017.

[57] Y. Belikov, K. Safarík and B. Batyunya, "Kalman Filtering Application for Track Recognition and Reconstruction in ALICE Tracking System", *ALICE-INT-1997-24, CERN-ALICE-INT-1997-24*, 1997.

[58] M. O. Schmidt, "Space-point calibration of the ALICE TPC with track residuals", *EPJ Web Conf.* 245 01003, arXiv:2003.03174 [physics.ins-det], 2020.

[59] A. Kalweit, "Production of light flavor hadrons and anti-nuclei at the LHC", *CERN-THESIS-2012-424*, 2012.

[60] C. Sonnabend, "ALICE TPC dE/dx performance - Run3 pp 13.6 TeV - With fitted ALEPH Bethe-Bloch parameterization", *Performance figure*, 2023.

[61] ALICE TPC, "Correction of the baseline fluctuations in the GEM-based ALICE TPC", *JINST* 18 no. 11, P11021, arXiv:2304.03881 [hep-ex], 2023.

[62] P. Chatzidaki, "Common-mode effect and ion-tail analysis of the GEM upgrade of the ALICE TPC at CERN", *master thesis*, 2020.

[63] M. Ivanov, personal communication, 2023.

[64] M. Mager, S. Rossegger and J. Thomas, "Composed correction framework for modeling the TPC field distortions in AliRoot", *ALICE-INT-2010-018*, 2011.

[65] ALICE, "AliRoot", https://github.com/alisw/AliRoot, 2016.

[66] ALICE, "Space-point distortion simulation framework", https://github.com/AliceO2Group/AliceO2/tree/dev/Detectors/TPC/spacecharge, 2024.

[67] S. Rossegger and J. Thomas, "Space-charge effects in the ALICE TPC: a comparison between expected ALICE performance and current results from the STAR TPC", *ALICE-INT-2010-017*, 2010.

[68] F. Lekien and J. Marsden, "Tricubic interpolation in three dimension", *Int. J. Numer. Methods Eng.* 63 455–471, 2005.

[69] E. Süli and D. F. Mayers, "An Introduction to Numerical Analysis", 2003.

[70] M. Arslandok *et al.*, "Track Reconstruction in a High-Density Environment with ALICE", *Particles* 5 no. 1, 84–95, arXiv:2203.10325 [physics.ins-det], 2022.

[71] A. M. Mathis, "First Measurement of the Proton$-\Sigma^0$ Interaction via the Femtoscopy Method", *CERN-THESIS-2020-094*, 2020.

[72] S. Gorbunov *et al.*, "Deep neural network techniques in the calibration of space-charge distortion fluctuations for the ALICE TPC", *EPJ Web Conf.* 251 03020, 2021.

[73] R. Shahoyan, "Summary of the L3 magnet field analysis", *ALICE-INT-2007-012*, 2007.

[74] M. Ivanov, personal communication, 2023.

[75] F. F. Van der Veken *et al.*, "LHC Beam Collimation During Extended β*-Levelling in Run 3", *ACoW IPAC* IPAC2022 2138–2141, 2022.

[76] E. O. Brigham and R. E. Morrow, "The fast Fourier transform", *IEEE Spectr.* 4 no. 12, 63–70, 1967.

[77] J. Wenninger, personal communication, 2023.

[78] C. G. Cuadrado, personal communication, 2024.

[79] T. Hastie, R. Tibshirani and J. Friedman, "The Elements of Statistical Learning", *Springer Series in Statistics*, 2009.

[80] F. Chollet *et al.*, "Keras", https://keras.io, 2015.

[81] C. de Boor, "Handbook of computer aided geometric design", *Spline Basics* 141–163, 2002.

[82] C. Olmsted, "Two Formulas for the General Multivariate Polynomial Which Interpolates a Regular Grid on a Simplex", *Math. Comp.* 47 no. 175, 275–284, 1986.

Acknowledgements

First of all, I would like to express my sincere gratitude to my supervisor, Henner Büsching. Since the start of my bachelor project, you have given me the opportunity to actively participate in the ALICE TPC group and to become part of this fascinating project. I would also like to thank you for the events we have organized together, such as the Night of Science. These moments were not only educational but also extremely entertaining.

A very big thank you goes to Harald Appelshäuser, for sharing your expertise on TPCs and for continuously supporting me in the TPC working group. Also, thank you for making yourself available as a second reviewer.

Special thanks go to Jens, without your help I would not have mastered programming in C++ and O^2. You have been a great mentor for my questions about TPCs and programming, as well as presentations and writing. Many thanks also for proofreading my thesis. Another big thank you goes to Ernst for our exciting work together on the correction of the space-charge distortions, your proofreading of my thesis, and your many wise suggestions. Special thanks also go to Marian for your creative ideas, innovative solutions and interesting discussions on the weekends. Without your input, this work would not have reached its current form. Thank you, Hannah Elfner, for the constructive exchange during the HGS-Hire PhD committee meetings. Your input has pushed me forward and motivated me to continue my work in a focused way.

I would also like to thank the TPC team at CERN, especially Robert, for your continued support in commissioning the IDCs at Point 2. Chiara, Ruben and David deserve a lot of thanks for their support in the ALICE collaboration, their expertise in O^2 and for helping to solve all kinds of technical problems that arose.

A heartfelt thank you goes to my long-time office colleague Joshua, who has accompanied me on my journey since my school days. Mario and Sebastian, many thanks for our joint phases of endurance while writing the thesis, for motivating me and especially Mario for your constant sense of humor. I extend my gratitude to all members of the IKF working group for the nice working atmosphere and the conversations outside of work, especially Marvin, Tuba, Janis, Nicolas, Michael, Steffi and Maria.